# Descriptor-Based Explorations on Flotation of Metal Sulfides Using Density Functional Theory Calculations

by

Hongbiao Tao

A thesis submitted in partial fulfillment of the requirements for the degree of

Doctor of Philosophy

in

Chemical Engineering

Department of Chemical and Materials Engineering

University of Alberta

# Abstract

Descriptor-based computational studies hold great promise for a more efficient optimization strategy for froth flotation of metal sulfides. To achieve this, fundamental insights into the ligand–metal sulfide interaction mechanism and identification of an effective descriptor possessing a predictive power toward the ultimate flotation index are highly desired. In this thesis, we have focused on understanding the trends in catalytic activity of metal sulfides for the oxygen reduction reaction (ORR) and the relative hydrophobic functionality of ligands toward metal sulfide using density functional theory (DFT) calculations. Thermodynamic calculations along the ORR elementary steps reveals that the catalytic activity trend of metal sulfides for ORR relates to its binding affinities toward ORR intermediates. This eventually led to the establishment of the S-3p band center as the descriptor linking the intrinsic attribute of metal sulfides with the corresponding catalytic ability. This descriptor also permits accurate prediction of the type of the anodic reaction product ($X_2$ or $MX_2$) between metal sulfide and xanthate. Regarding the surface hydrophobization of metal sulfides (galena and sphalerite), it is demonstrated that the chemical bond between the commonly used S/O-terminated ligands and metal sulfide is essentially ionic with limited covalency. This is in stark contrast to the conventional perception of these bonds. Moreover, instead of the generally used binding energy concept, we proposed that the electronegativity of ligand captures the relative ligand–metal sulfide bond ionicity, and it can potentially serve as the descriptor with respect to the hydrophobic functionality of the ligands toward metal sulfides. This study, therefore, further advanced our understandings on the catalytic activity of metal sulfides for ORR, shed light on the intrinsic ligand–metal sulfide binding mechanism and provided the thought-provoking descriptors.

# Preface

Chapter 3 has been published as "Hongbiao Tao, Subiao Liu, Jing-Li Luo, Phillip Choi, Qi Liu*, Zhenghe Xu*, Descriptor of Catalytic Activity of Metal Sulfides for Oxygen Reduction Reaction: A Potential Indicator for Mineral Flotation, Journal of Materials Chemistry A, 2018, 6(20), 9650-9656." I was responsible for designing and performing DFT calculations, data analysis and drafting/revising the paper. Drs. Xu, Liu and Choi were actively involved in the concept formation and the manuscript composition. Drs. Subiao Liu and Jing-Li Luo provided valuable comments and feedbacks for the manuscript writing and revision.

Chapter 4 has been/will be submitted as "Hongbiao Tao, Subiao Liu, Mingxia Liu, Phillip Choi, Qi Liu*, Zhenghe Xu*, Revelation of the Nature of Ligand−PbS Bond and Its Implication on Chemical Functionalization of PbS." I was responsible for designing and performing DFT calculations, data analysis and drafting/revising the paper. Drs. Xu, Liu and Choi were actively involved in the concept formation and the manuscript composition. Drs. Subiao Liu and Mingxia Liu provided valuable comments and feedbacks for the manuscript writing and revision.

Chapter 5 has been published as "Hongbiao Tao, Phillip Choi, Qi Liu*, Zhenghe Xu*, Chemical Functionalization of ZnS: A Perspective from Ligand−ZnS Bond Character, Journal of Physical Chemistry C, 2019, 123(10), 6054-6061." I was responsible for designing and performing DFT calculations, data analysis and drafting/revising the paper. Drs. Xu, Liu and Choi were actively involved in the concept formation and the manuscript writing and revision.

# Acknowledgement

PhD is a journey of self-exploration, tough but fun.

Thank Drs. Zhenghe Xu, Qi Liu and Phillip Choi for leading and cultivating me during the journey.

Thank Drs. Ye Chen and Hao Zhang for amazing me with the beauty of simulations, Drs. Jing-Li Luo, Subiao Liu, Zifu Li and Lei Xie for their continuous encouragements, Lisa Carreiro, Jim Skwarok, Lily Laser and Dr. Kaipeng Wang for their solid supports, and my friends, group members and roommates for sharing wonderful memories.

Thank the $C^5$MPT and NSERC for the financial support for the research.

Deep thanks for my great parents and girlfriend for their invaluable love and care.

# Table of Contents

# List of Figures

# List of Schemes

# List of Tables

# List of Nomenclatures

| | |
|---|---|
| $E$ | Energy of the system (eV) |
| $E_{kin}^{non}$ | Kinetic energy of the reference system (eV) |
| $E_{ext}$ | External energy (eV) |
| $E_H$ | Hartree energy (eV) |
| $E_{xc}$ | Exchange-correlation energy (eV) |
| $\widehat{H}_{KS}$ | KS one-electron Hamiltonian operator |
| $\varepsilon$ | KS orbital energy (eV) |
| $n$ | the number of electrons |
| $k$ | the number of nuclei |
| $\rho$ | Electron density (Å$^{-3}$) |
| $\Delta\rho$ | Electron density difference (Å$^{-3}$) |
| $\boldsymbol{r}$ | Electronic coordination |
| $\phi$ | Kohn-Sham orbital |
| $D(\varepsilon)$ | the number of electronic states at $\varepsilon$ |
| $E_F$ | Fermi energy (eV) |
| $\mathrm{R}^2$ | Coefficient of determination |
| $\Delta E$ | Binding energy (eV) |
| $EA$ | Electron affinity (eV) |
| $IE$ | Ionization energy (eV) |
| $\lambda$ | Empirical electronegativity |
| $\chi$ | Computational electronegativity |
| $p\mathrm{K}_{\mathrm{sp}}$ | Solubility product constant |

# List of Abbreviations

| | |
|---|---|
| AA | Acetic acid |
| AFM | Atomic force microscopy |
| AMT | 4-amino-5-mercapto-1,2,4-triazole |
| BZ | Brillouin Zone |
| CDDM | Charge density difference map |
| CHE | Computational hydrogen electrode |
| $CO_2RR$ | Carbon dioxide reduction reaction |
| DFT | Density functional theory |
| DOS | Density of states |
| DTC | Dimethyl dithiocarbamate |
| DTP | Dimethyl dithiophosphate |
| ELF | Electron localization function |
| EX | Ethyl xanthate |
| FTIR | Fourier transform infrared spectroscopy |
| GPAW | Grid-based projector-augmented wave method |
| HER | Hydrogen evolution reaction |
| HK | Hohenberg-Kohn |
| HSE | Heyd-Scuseria-Ernzerhof |
| IBZ | Irreducible Brillouin Zone |
| KS | Kohn-Sham |
| LDOS | Local density of states |
| MX | Metal-xanthate |
| ORR | Oxygen reduction reaction |

| | |
|---|---|
| PAW | Projector-augmented wave |
| PBE | Perdew-Burke-Ernzerhof |
| PDOS | Projected density of states |
| PEMFCs | Polymer electrolyte membrane fuel cells |
| PP | Pseudopotential |
| PW | Plane wave |
| PW91 | Perdew-Wang 91 |
| RPBE | Revised Perdew-Burke-Ernzerhof |
| SHE | Standard hydrogen electrode |
| VASP | Vienna *Ab initio* Simulation Package |
| VB | Valence band |
| XC | Exchange correlation |
| XPS | X-ray photoelectron spectroscopy |

# Chapter 1 Introduction

## 1.1 Froth flotation of metal sulfides

Metal sulfide minerals constitute the major raw resources for a wide range of elemental metals. Prior to the metallurgical extraction of valuable metallic elements, sulfide minerals need to be separated and enriched from the host rock matrix. This largely contributes to lowering the prohibitive cost of the subsequent transportation and smelting operations, removing harmful elements/compounds, as well as reducing the losses of valuable metals by producing less metal-bearing slags.[1]

Enrichment of mineral incorporates primarily the liberation and concentration units. Firstly, the value minerals are liberated from the associated gangue minerals following a typical sequence of crushing, screening, grinding and classification. The adequately liberated minerals are then subject to concentration by virtue of various physical (e.g., sorting, electrostatic separation, magnetic separation, gravity concentration and froth flotation) and/or chemical (e.g., pyrometallurgy, hydrometallurgy and biometallurgy) techniques depending on the unique properties of the ore.

Among the numerous approaches, froth flotation, is the most widely used technique to separate value metal sulfides from the unwanted gangue minerals. The floatability of certain mineral particle relies heavily on its surface physicochemical properties, especially the surface hydrophobicity.[2,3] However, the majority of the sulfide minerals are not sufficiently hydrophobic in the natural state. Thus, an economically acceptable quality of value minerals can only be acquired with the aid of functional chemical reagents.

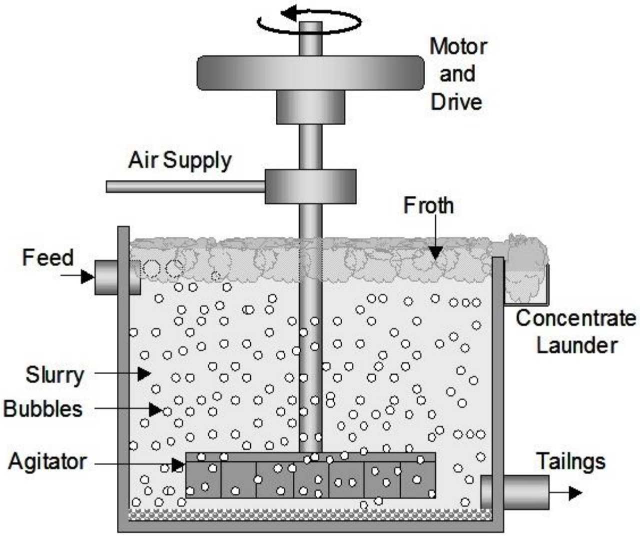

**Figure 1.1** Froth flotation operation.[4]

The surfactants, known as collectors, are probably the most important reagents for a desired flotation recovery index. The collector for metal sulfides normally comprises a chemically reactive head group and a short (2-5 carbons) hydrocarbon tail, such as the commonly used ethyl xanthate ($C_2H_5OCS_2$), dimethyl dithiocarbamate (DTC, $C_2H_6NCS_2$) and dimethyl dithiophosphate (DTP, $C_2H_6O_2PS_2$). When added to the flotation pulp, the collector selectively adsorbs on the surface of target metal sulfide, thereby rendering the surface with desired hydrophobicity. On the other hand, the collector is rather inert toward the gangue or clay minerals. Such selective hydrophobization process further enlarges the hydrophobicity difference between metal sulfide and gangue minerals. As a consequence, the attachment of value mineral particles to air bubbles for buoyancy and recovery is facilitated, whereas the gangue minerals remain in the pulp and eventually report to tailings, as shown in Figure 1.1. The entire process as depicted constitutes a typical case of direct flotation circuit.

## 1.2 The electrochemical model of metal sulfide/collector interaction

Xanthate is a thiol-collector that has ever brought the radical evolution of froth flotation technology. Since its introduction in flotation in 1925, xanthate remains a working-horse collector for flotation separation of metal sulfides as well as the model ligand for screening and designing of ligands with customized functionalities. Although many other auxiliary flotation chemicals (e.g., pH regulator, activator, depressant and frother) are also used to further regulate the flotation conditions, the collector is considered as the essence of froth flotation. Collectors possessing efficient hydrophobic functionality not only contribute to the satisfactory recovery of value minerals, but they also can substantially reduce the dosage of auxiliary chemicals and thus alleviate the negative impacts of a complex flotation pulp.

Given the critical role of thiol-collectors in flotation of metal sulfides, various experimental tools have been employed to reveal the ligand–metal sulfide interaction mechanism. These include the electrochemical method (e.g., open circuit potential[5] and cyclic voltammetry[6]), the spectroscopic analysis (e.g., Raman spectroscopy,[7] Fourier transform infrared spectroscopy[8,9] and X-ray photoelectron spectroscopy[3,10]), the advanced surface force characterization (e.g., atomic force microscopy[11]), and so on. Generally, the interaction between metal sulfides and xanthate and other thiol-collectors have been recognized as an electrochemical process. The underlying mechanism is well summarized by the so-called mixed potential model involving metal sulfide, oxygen and collector (X), as presented in Figure 1.2.

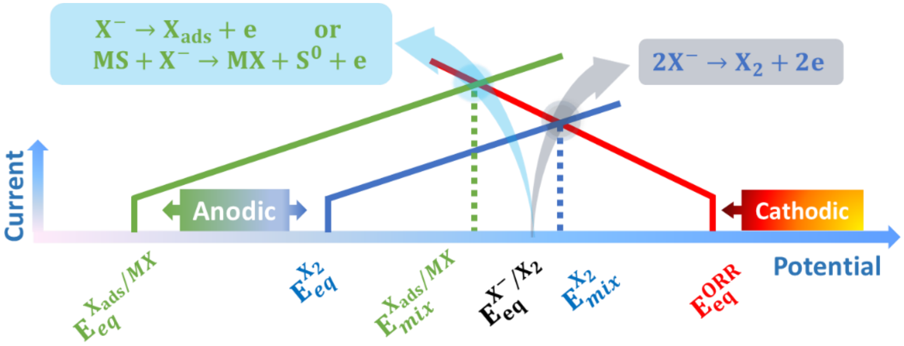

**Figure 1.2** The electrochemical model of metal sulfide–xanthate interaction.

According to this model, xanthate undergoes anodic reactions on the surface of the metal sulfide, and the oxygen reduction reaction (ORR) accounts for the cathodic reaction in the aerated flotation pulp.[11,12] The catalyzing ability of metal sulfide for ORR is measured by the potential at which there is no net current flow across the solid/solution interface. This potential is also named as mixed potential or rest potential that plays a crucial role in determining the type of the surface anodic reaction product.[5] Depending on the relative magnitude of the rest potential and the equilibrium potential of $X^-/X_2$, the reaction product on the surface of metal sulfide is predominantly either dixanthogen ($X_2$) or metal-xanthate salt (MX), regardless of the pulp pH and chain length of the xanthate homologue. As such, metal sulfides can be classified into two groups in line with the electrochemical mechanism, those on which metal xanthate is formed, and those on which dixanthogen is formed. For example, pyrite ($FeS_2$) and galena (PbS) have been widely referenced as the representative metal sulfides forming dixanthogen and metal-xanthate salt, respectively. In spite of the different types of the anodic products, chemisorption of ligand on metal sulfide has been suggested as the initial step upon metal sulfide–ligand interaction. This forms the basis for the widely adopted chemisorption models in many first-principles calculations.

## 1.3 Density functional theory

Density functional theory (DFT) is a revolutionary framework developed by Kohn et al., aiming to practically solve the many-body Schrödinger wave equation. This theory is built on the Hohenberg-Kohn (HK) theorems and the Kohn-Sham (KS) scheme.[13–15] The HK theorems state that the ground-state electron density uniquely determines the external potential and vice versa, and the ground state electron density can be obtained using the variational principle.[16] The electron density, $\rho(\boldsymbol{r})$, denotes the number of electrons per unit volume at a given point **r**, and integration of the electron density over all space gives the total number of electrons in the system. The coordinate notation **r** is defined to include both three spatial coordinates (x, y, z) and spin (↑, ↓) coordinates, and the atomic unit is adopted throughout this section.

The HK theorems established the electron density distribution as the chief parameter in the wave equation and linked it with the Hamiltonian and the wave function. Following these, Kohn and Sham constructed a fictitious system with noninteracting electrons, but this system has the electron density identical to that of the real one.[17] Based on the noninteracting reference system, the electron density is written as the sum over a set of squares of noninteracting KS orbitals $[\phi_i(\boldsymbol{r})]$,

$$\rho(\boldsymbol{r}) = \sum_i |\phi_i(\boldsymbol{r})|^2 \qquad \text{1-1}$$

The energy functional of a nondegenerate system at the ground state is then divided and expressed as,

$$E[\rho(\boldsymbol{r})] = E_{kin}^{non}[\phi(\boldsymbol{r})] + E_{ext}[\rho(\boldsymbol{r})] + E_H[\rho(\boldsymbol{r})] + E_{xc}[\rho(\boldsymbol{r})] \qquad \text{1-2}$$

$$E_{kin}^{non}[\phi(\boldsymbol{r})] = -\frac{1}{2}\sum_{i=1}^{n} \phi_i^*(\boldsymbol{r})\nabla^2\phi_i(\boldsymbol{r}) \qquad \text{1-3}$$

$$E_{ext}[\rho(\boldsymbol{r})] = -\sum_{k}^{nuclei} \int \frac{Z_k}{|\boldsymbol{r}-\boldsymbol{r}_k|} \rho(\boldsymbol{r}) d\boldsymbol{r} \quad \text{1-4}$$

$$E_H[\rho(\boldsymbol{r})] = \frac{1}{2} \iint \frac{\rho(\boldsymbol{r})\rho(\boldsymbol{r}')}{|\boldsymbol{r}-\boldsymbol{r}'|} d\boldsymbol{r} d\boldsymbol{r}' \quad \text{1-5}$$

$$E_{xc}[\rho(\boldsymbol{r})] = \int \frac{\delta E_{xc}[\rho(\boldsymbol{r})]}{\delta \rho(\boldsymbol{r})} \rho(\boldsymbol{r}) d\boldsymbol{r} \quad \text{1-6}$$

where $E_{kin}^{non}$, $E_{ext}$, $E_H$ and $E_{xc}$ represent the kinetic energy of the reference system, the external energy associated with the nuclei, the Hartree energy accounting for the classical electron repulsions, and the exchange-correlation energy, respectively; $n$ is the number of electrons and $k$ is the number of nuclei. The repulsive interaction energy between the nuclei can be added as a constant within the Born-Oppenheimer approximation. By further applying the variational principle with respect to the electron density or wave functions using the Lagrange multiplier which ensures the orthonormal constraint of the wave functions, a set of coupled KS equations can be obtained,

$$\widehat{H}_{KS} \phi_i(\boldsymbol{r}) = \varepsilon_i \phi_i(\boldsymbol{r}) \quad \text{1-7}$$

$$\widehat{H}_{KS} = -\frac{1}{2}\nabla^2 - \sum_{k}^{nuclei} \frac{Z_k}{|\boldsymbol{r}-\boldsymbol{r}_k|} + \int \frac{\rho(\boldsymbol{r}')}{|\boldsymbol{r}-\boldsymbol{r}'|} d\boldsymbol{r}' + \frac{\delta E_{xc}[\rho(\boldsymbol{r})]}{\delta \rho(\boldsymbol{r})} \quad \text{1-8}$$

where $\widehat{H}_{KS}$ is the KS one-electron Hamiltonian operator and $\varepsilon_i$ is the corresponding eigenvalue. The exchange-correlation term, $E_{xc}$, is essentially what the density functional theory is all about. It contains the effects of the quantum mechanical exchange and correlation, the correction for self-interaction energy due to the mean-field approximation, and the difference in kinetic energy between the reference and the real systems. However, the explicit form of this term remains unknown and is thus subject to approximations. There have been many available exchange-correlation functionals, such as the earlier local density approximation,[17] a series of the popular generalized gradient approximation-based functionals including Perdew-Wang 91 (PW91),[18] Perdew-Burke-Ernzerhof (PBE)[19] and revised Perdew-Burke-Ernzerhof (RPBE),[20] and the advanced hybrid functionals (PBE0[21] and HSE[22]). The exchange-correlation functional with higher accuracy is continuously being developed.

Regarding the treatment of solids, some commonly used approaches in first-principles calculations in conjunction with the structural periodicity of the solid are utilized, since both the number of electrons and atoms are infinite for the real systems. For example, the strongly bound and chemically inert core electrons are grouped together with the nuclei and are treated as the ionic core based on the frozen-core approximation. With the pseudopotential (PP) or the projector-augmented wave[23] method, the valence electron wave function and the corresponding potential can be reasonably pseudized. Meanwhile, the number of atoms can also be substantially reduced by virtue of the structural periodicity. Specifically, the solid is represented by a supercell model that can accurately represent the solid system without losing any information under the periodical boundary condition. The supercell can be transformed into the reciprocal space within the first Brillouin zone (BZ) which in turn can be further confined to the irreducible Brillouin zone (IBZ) through effective symmetry operations. The IBZ is then mapped with discrete *k*-points, and all necessary quantities can be obtained by integration/summation/extrapolation on these points. Consequently, dealing with a solid becomes equivalent to treating a handful of uniformly distributed *k*-points within the IBZ. The dramatically reduced computational burden brings DFT to the level of practical use for molecules and solids. It is currently being used routinely in a broad class of disciplines owing to its great success in terms of both accuracy and efficiency.

## 1.4 DFT studies in flotation of metal sulfides

The past several decades have witnessed the radical advancement of the accuracy of theoretical description of surface chemical reactions.[24,25] The first-principles studies, particularly the density functional theory (DFT) calculation, are increasingly becoming an indispensable tool to obtain atomistic insights into the adsorption mechanism and to identify descriptors linking the intrinsic attribute of material with the activities of interest.[24,26] For instance, the remarkable d-band model has been successfully applied as computational guideline for the design of transition metal-based catalysts for a number of catalytic reactions.[27,28] Likewise, DFT calculations have also been exploited in the field of minerals flotation. Up to now, the research directions in flotation of metal sulfides using DFT are relatively broad, covering the natural hydrophobicity of metal sulfide surface,[29,30] the ligand (collector and depressant)–metal sulfide binding,[31,32] and the effect of impurity/defect on geometric/electronic structures of metal sulfide bulk/surface as well as the ligand–metal sulfide interaction.[33] Typical studies in each of the directions are briefly reviewed with an emphasis on the collector–metal sulfide binding interaction.

Chen et al. simulated the adsorption of multilayer water molecules on (100) surfaces of pyrite and galena and noticed a dependence of the water–mineral interaction on the type of minerals.[29] Water adsorbs on $FeS_2(100)$ via the interaction between O ions from water molecules and Fe ions on $FeS_2(100)$, whereas the interaction on PbS(100) proceeds through the formation of hydrogen bond between the S ions on PbS(100) and H ions from water molecules. By comparing the water–mineral binding energy, they concluded that the bare surface of pyrite is more hydrophilic than that of galena. Later, the same group investigated the adsorption of water molecules on (110) surfaces of pure and Cu-activated sphalerite mineral.[30] The water–sphalerite interaction associates with both the formation of hydrogen bonds between the S ions on

ZnS(110) and O ions from water molecules and the Zn–O binding interaction. Besides, compared with the pure surface, the existence of the doping copper ions on ZnS(110) promotes the bond covalency on the surface. The enhanced surface covalency leads to the decrease of the hydrogen bonding strength and yields a less hydrophilic sphalerite surface.

Sarvaramini et al. studied the adsorption of four thiophosphorus-based collectors on the (110) facet of chalcopyrite mineral.[31] In their work, the terminal S and O ions from the collectors were shown to preferably bind with the Fe and Cu ions on $CuFeS_2(110)$ in a bidentate bridging pattern. Waterson et al. probed the effect of different metal-terminated (111) facets of pentlandite on the xanthate–pentlandite binding process.[32] They concluded that the Fe-enriched surface of pentlandite exhibits higher binding affinity toward xanthate than the Ni-enriched surface.

It is well known that metallic impurities are commonly embedded within the naturally existed minerals and play important roles on the resulting surface reactivity. Chen et al. found that the presence of metallic impurities leads to distinct variances of both the crystal and electronic structures of sphalerite, depending on the type of the doped impurity. The impurity can change the lattice constants and band gap of sphalerite as well as the binding ability of sphalerite toward oxygen and xanthate.[33]

Regarding the ligand–metal sulfide interaction, the effect of water molecules on the adsorption of ligand on metal sulfide surface ranging from one and two water molecules to multi-water molecule layers have been studied. Long et al. calculated the adsorption strengths of ethyl xanthate (EX), dithiocarbamate (DTC) and dithiophosphate (DTP) on PbS(100) and ZnS(110) with and without the inclusion of water molecules.[34] The solvation model was constructed by including two water molecules on the surface emulating the aqueous environment. In vacuum, the binding strength trend (DTC < EX < DTP) remains unchanged, regardless of the different types of minerals. With the presence of water molecules, the ligand–metal sulfide binding strength was weakened for both galena and sphalerite. However, the same binding trend was reserved for galena. For ZnS(110), the DTP still exhibits the strongest binding affinity toward ZnS(110), whereas the binding strength of EX with ZnS(110) becomes comparable with that of DTC.

Using DFT calculations with explicit water molecules, Sarvaramini et al. found that 18 out of 24 water molecules were found to adsorb on ZnS(110) at a surface area of 252.8 $Å^2$, constituting a monolayer configuration. Among the adsorbed water molecules, 10 water molecules bind with zinc ions, eight water molecules bind with sulfur ions and the rest six water molecules sit above the water monolayer by forming hydrogen bonds with the underlying water molecules. Besides, they found that the terminal sulfur ions of DTP bind with the adjacent zinc ions in the same row on ZnS(110) and form two chemical bonds. The adsorption of lead ion on ZnS(110) gives rise to a stronger binding strength of DTP on the lead-activated sphalerite, forming two chemical bonds with the terminal sulfur ions from DTP. In terms of the solvation model, one collector and ninety water molecules were optimized through molecular dynamic simulations method prior to DFT calculations. The presence of water molecules was found to lower the DTP–ZnS(110) binding strength for both the bare and the lead-activated surface.[35]

Similarly, the depressing mechanism of 4-amino-5-mercapto-1,2,4-triazole (AMT) toward chalcopyrite for the flotation separation of the Cu- and Mo-bearing metal sulfides was studied by Sun et al.[36] In their study, AMT formed a five-membered chelate ring with the adjacent Cu and Fe ions on $CuFeS_2(100)$. Based on the relative adsorption energies, they concluded that AMT prefers to bind with Cu ions over the Fe ions due to a more negative Cu-AMT binding energy than that of the Fe-AMT.

## 1.5 Objectives

Existing DFT studies in the context of minerals flotation have been primarily focused on the ligand–metal sulfide binding process, and the computational binding energy has been generally used to evaluate/compare the relevant functionality of ligands toward metal sulfides. However, the trend of binding energies, in certain cases, is completely opposite to the trend of the corresponding experimental metric. Moreover, the underlying reasons credited for the catalytic activity trend of metal sulfides for ORR and hence the different type of the anodic reaction product remain unclear.

To address these issues and also to obtain first-principles guidelines for the flotation process optimization and the design of new collectors, the main objectives are to understand two fundamental questions in connection with the recognized mixed-potential model: why different metal sulfides exhibit discriminated catalytic activities for ORR? Why the same metal sulfide acquires different surface hydrophobicity when interacting with ligands with a similar hydrocarbon tail but different head groups? The detailed objectives include,

1) Investigate and compare the catalytic activities of metal sulfides for ORR using DFT calculations. The results are expected to shed light on the distinct catalytic activities of metal sulfides for ORR and provide atomic-scale insights into the trends in catalytic activity. The goal is to identify an effective descriptor that permits the prediction of the predominant type of the resulting surface anodic product in the presence of xanthate.

2) Probe the binding mechanism between the commonly used S/O-terminated ligands and PbS(100) using DFT calculations. Particular emphasis will be centered on the resulting ligand–PbS(100) bond character. The goal is to identify a descriptor rather than the binding energy that allows more accurate prediction of the hydrophobic functionality of the ligand toward galena mineral.

3) Probe the binding mechanism between the commonly used ligands and ZnS(110) using DFT calculations as well as the resulting ligand–ZnS(110) bond character. The goal is to identify a descriptor rather than the binding energy that allows more accurate prediction of the hydrophobic functionality of the ligand toward sphalerite mineral.

## 1.6 Structure of the thesis

Chapter 1 introduces the importance of metal sulfide resources, basic principles of froth flotation of metal sulfides, and fundamental concepts and formulations of density functional theory (DFT). The recent and representative DFT studies on flotation of metal sulfides are briefly reviewed, the current state of DFT calculations in the context of minerals flotation is discussed, from which the objectives of this thesis are defined.

Chapter 2 presents the basic workflow of DFT calculations in VASP and the relevant techniques adopted in this study.

Chapter 3 explored the catalytic activity of metal sulfides for oxygen reduction reaction (ORR) using DFT calculations, and identified the computational descriptor linking the intrinsic attribute of metal sulfide with its catalytic activity for ORR.

Chapter 4 investigated the ligand–PbS(100) binding mechanism, probed the ligand–PbS(100) bond character, clarified the inconsistency between the binding energy trend and the hydrophobic functionality of the ligands toward galena mineral, and proposed to use the ligand electronegativity as the corresponding descriptor.

Chapter 5 investigated the ligand–ZnS(110) binding mechanism, uncovered the ligand–ZnS(110) bond character, resolved the inconsistency between the relative binding energy and the hydrophobic functionality of the ligands toward sphalerite mineral, and proposed to use the ligand electronegativity as the corresponding descriptor.

Chapter 6 summarizes the major conclusions and the original contributions of this thesis. The suggestions for future work in this field are also provided.

## 1.7 References

(1) Wills, B. A.; Finch, J. A. *Wills' Mineral Processing Technology: An Introduction to the Practical Aspects of Ore Treatment and Mineral Recovery*; Butterworth-Heinemann, 2016.

(2) Vaughan, D. J. Sulfide Mineralogy and Geochemistry: Introduction and Overview. *Rev. Mineral. Geochemistry* **2006**, *61* (1), 1–5.

(3) Xie, L.; Wang, J.; Shi, C.; Cui, X.; Huang, J.; Zhang, H.; Liu, Q.; Liu, Q.; Zeng, H. Mapping the Nanoscale Heterogeneity of Surface Hydrophobicity on the Sphalerite Mineral. *J. Phys. Chem. C* **2017**, *121* (10), 5620–5628.

(4) Strand, A.; Zasadowski, D.; Norgren, M.; Hedenstrom, E.; Willfor, S.; Sundberg, A. Selective Froth Flotation of Pitch Components from Spruce TMP Process Water. *Appita J.* **2012**, *65* (4), 337–346.

(5) Allison, S.; Goold, L.; Granville, A. A Determination of the Products of Reaction Between Various Sulfide Minerals and Aqueous Xanthate Solution, and a Correlation of the Products with Electrode Rest Potentials. *Metall. Trans.* **1972**, *3* (10), 2613–2618.

(6) Mu, Y.; Peng, Y.; Lauten, R. A. Electrochemistry Aspects of Pyrite in the Presence of Potassium Amyl Xanthate and a Lignosulfonate-Based Biopolymer Depressant. *Electrochim. Acta* **2015**, *174* (1), 133–142.

(7) Schlücker, S. Surface-Enhanced Raman Spectroscopy: Concepts and Chemical Applications. *Angew. Chemie - Int. Ed.* **2014**, *53* (19), 4756–4795.

(8) Gilbert, B.; Huang, F.; Lin, Z.; Goodell, C.; Zhang, H.; Banfield, J. F. Surface Chemistry

Controls Crystallinity of ZnS Nanoparticles. *Nano Lett.* **2006**, *6* (4), 605–610.

(9) Yang, H.; Li, F.; Shan, C.; Han, D.; Zhang, Q.; Niu, L.; Ivaska, A. Covalent Functionalization of Chemically Converted Graphene Sheets via Silane and Its Reinforcement. *J. Mater. Chem.* **2009**, *19* (26), 4632–4638.

(10) Voiry, D.; Goswami, A.; Kappera, R.; Silva, C. D. C. C. E.; Kaplan, D.; Fujita, T.; Chen, M.; Asefa, T.; Chhowalla, M. Covalent Functionalization of Monolayered Transition Metal Dichalcogenides by Phase Engineering. *Nat. Chem.* **2015**, *7* (1), 45–49.

(11) Xie, L.; Wang, J.; Shi, C.; Huang, J.; Zhang, H.; Liu, Q.; Liu, Q.; Zeng, H. Probing Surface Interactions of Electrochemically Active Galena Mineral Surface Using Atomic Force Microscopy. *J. Phys. Chem. C* **2016**, *120* (39), 22433–22442.

(12) Chandra, A. P.; Gerson, A. R. A Review of the Fundamental Studies of the Copper Activation Mechanisms for Selective Flotation of the Sulfide Minerals, Sphalerite and Pyrite. *Adv. Colloid Interface Sci.* **2009**, *145* (1–2), 97–110.

(13) Kohn, W.; Becke, A. D.; Parr, R. G. Density Functional Theory of Electronic Structure. *J. Phys. Chem.* **1996**, *100* (31), 12974–12980.

(14) Lee, J. G. *Computational Materials Science: An Introduction*; Crc Press, 2016.

(15) Cramer, C. J. *Essentials of Computational Chemistry Theories and Models*, Second Edi.; John Willey & Sons Ltd: Chichester, 2004.

(16) Pierre, H.; Kohn, W. Inhomogeneous Electron Gas. *Phys. Chem. Chem. Phys.* **1964**, *136* (3B), 864–871.

(17) Kohn, W. and Sham, L. J. Self-Consistent Equations Including Exchange and Correlation Effects. *Phys. Rev.* **1965**, *140* (4A), A1133.

(18) Perdew, J. P.; Wang, Y. Accurate and Simple Analytic Representation of the Electron Gas Correlation Energy. *Phys. Rev. B* **1992**, *45* (23), 13244–13249.

(19) Perdew, J. P.; Burke, K.; Ernzerhof, M. Generalized Gradient Approximation Made Simple. *Phys. Rev. Lett.* **1996**, *77* (18), 3865–3868.

(20) Hammer, B.; Hansen, L. B.; Nørskov, J. K. Improved Adsorption Energetics within Density-Functional Theory Using Revised Perdew-Burke-Ernzerhof Functionals. *Phys. Rev. B* **1999**, *59* (11), 7413–7421.

(21) Perdew, J. P.; Ernzerhof, M.; Burke, K. Rationale for Mixing Exact Exchange with Density Functional Approximations. *J. Chem. Phys.* **1996**, *105* (22), 9982–9985.

(22) Heyd, J.; Scuseria, G. E.; Ernzerhof, M. Hybrid Functionals Based on a Screened Coulomb Potential. *J. Chem. Phys.* **2003**, *118* (18), 8207–8215.

(23) Blöchl, P. E. Projector Augmented-Wave Method. *Phys. Rev. B* **1994**, *50* (24), 17953–17979.

(24) Nørskov, J. K.; Bligaard, T.; Rossmeisl, J.; Christensen, C. H. Towards the Computational Design of Solid Catalysts. *Nat. Chem.* **2009**, *1* (1), 37–46.

(25) Neese, F., Atanasov, M., Bistoni, G., Maganas, D. and Ye, S. Chemistry and Quantum Mechanics in 2019: Give Us Insight and Numbers. *J. Am. Chem. Soc.* **2019**, *141* (7), 2814–2824.

(26) Nørskov, J. K.; Abild-Pedersen, F.; Studt, F.; Bligaard, T. Density Functional Theory in Surface Chemistry and Catalysis. *Proc. Natl. Acad. Sci.* **2011**, *108* (3), 937–943.

(27) Kulkarni, A.; Siahrostami, S.; Patel, A.; Nørskov, J. K. Understanding Catalytic Activity Trends in the Oxygen Reduction Reaction. *Chem. Rev.* **2018**, *118* (5), 2302–2312.

(28) Hammer, B.; Nørskov, J. K. Electronic Factors Determining the Reactivity of Metal Surfaces. *Surf. Sci.* **1995**, *343* (3), 211–220.

(29) Chen, J.; Long, X.; Chen, Y. Comparison of Multilayer Water Adsorption on the Hydrophobic Galena (PbS) and Hydrophilic Pyrite ($FeS_2$) Surfaces: A DFT Study. *J. Phys. Chem. C* **2014**, *118* (22), 11657–11665.

(30) Li, Y., Chen, J., Chen, Y., Zhu, Y. and Liu, Y. DFT Simulation on Interaction of $H_2O$ Molecules with ZnS and Cu-Activated Surfaces. *J. Phys. Chem. C* **2019**, *123* (5), 3048–3057.

(31) Sarvaramini, A.; Larachi, F. Understanding the Interactions of Thiophosphorus Collectors with Chalcopyrite through DFT Simulation. *Comput. Mater. Sci.* **2017**, *132*, 137–145.

(32) Waterson, C. N.; Sindt, J. O.; Cheng, J.; Tasker, P. A.; Morrison, C. A. First-Principles Study on Ligand Binding and Positional Disorder in Pentlandite. *J. Phys. Chem. C* **2015**, *119* (45), 25457–25468.

(33) Chen, Y.; Chen, J.; Lan, L.; Yang, M. The Influence of the Impurities on the Flotation Behaviors of Synthetic ZnS. *Miner. Eng.* **2012**, *27–28*, 65–71.

(34) Long, X.; Chen, Y.; Chen, J.; Xu, Z.; Liu, Q.; Du, Z. The Effect of Water Molecules on the Thiol Collector Interaction on the Galena (PbS) and Sphalerite (ZnS) Surfaces: A DFT

Study. *Appl. Surf. Sci.* **2016**, *389*, 103–111.

(35) Sarvaramini, A.; Larachi, F.; Hart, B. Collector Attachment to Lead-Activated Sphalerite–Experiments and DFT Study on PH and Solvent Effects. *Appl. Surf. Sci.* **2016**, *367*, 459–472.

(36) Yin, Z.; Hu, Y.; Sun, W.; Zhang, C.; He, J.; Xu, Z.; Zou, J.; Guan, C.; Zhang, C.; Guan, Q.; et al. Adsorption Mechanism of 4-Amino-5-Mercapto-1,2,4-Triazole as Flotation Reagent on Chalcopyrite. *Langmuir* **2018**, *34* (13), 4071–4083.

# Chapter 2 Density functional theory calculations

## 2.1 DFT calculations with VASP

There are many available commercial and open source software packages for DFT calculations, such as Materials Studio, Vienna *Ab initio* Simulation Package (VASP), Grid-Based Projector Augmented Wave Method (GPAW) and Quantum ESPRESSO. Among these, Materials Studio and VASP are the most popular ones for solid systems of interest in the context of minerals flotation. In this study, VASP is used and is briefly introduced below.

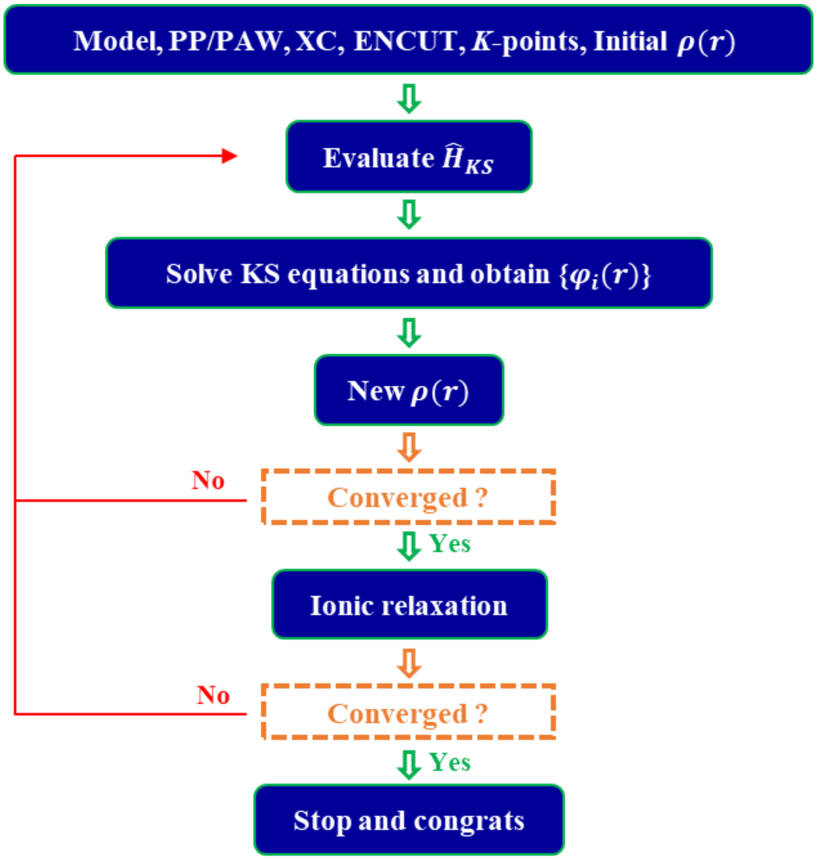

**Scheme 2.1** The basic workflow of DFT calculations in VASP.

VASP[1–4] is a sophisticated computer program for first-principles calculations using the pseudopotential (PP) or the projector-augmented wave method (PAW)[5,6] and a plane wave (PW) basis set. VASP is currently being widely used around the world owing to its demonstrated accuracy and efficiency. It has been proven suitable for many systems, such as atoms, molecules, bulk solids, surfaces and clusters.[7] The basic procedures of DFT calculation in VASP is presented in Scheme 2.1. Specifically,

1) Build the model under investigation, specify the PP/PAW scheme and the exchange-correlation (XC) functional approximation, and set the cutoff-energy (ENCUT) and $K$-points.
2) Construct the initial trial electron density, $\rho(r)$, of the model system by superimposing the electron densities of each atom as provided by the designated PP.
3) Expand the one-electron KS orbitals with the PW basis set.
4) Calculate each of the items in the Kohn-Sham operator, $\widehat{H}_{KS}$, and construct the $\widehat{H}_{KS}$.
5) Solve the coupled KS equations by an iterative diagonalization of the KS matrix in the real and reciprocal spaces.
6) Generate the new $\rho(r)$ with the newly calculated set of $\phi_i(r)$, mix it with the previous densities, and then resume for the next inner self-consistent loop at fixed ionic positions until the electronic minimization is achieved.
7) Calculate the forces on atoms and update the positions of the atoms accordingly, and then repeat the above electronic and ionic minimizations.
8) After successive modifications of $\widehat{H}_{KS}$, $\rho(r)$ and ionic positions, stop iteration when both the energy and force changes meet the preset convergence criteria.

## 2.2 The VASPsol

The implicit solvation model, VASPsol,[8,9] was used to evaluate the solvation effect on the solid system which has been successfully employed for many interfacial adsorption studies.[8–11] Within this model, the thermodynamically-averaged effect of water is replaced by the electrostatic response of a continuum dielectric cavity along with the corrections for cavity formation and dispersion energies, aimed at avoiding the computationally prohibitive sampling of explicit solvent configurations. More details on the VASPsol can be found in Appendix C.

## 2.3 Relevant techniques

### 2.3.1 Density of states

Density of states (DOS) denote the number of electronic states per unit energy range ($d\varepsilon$). The integral of DOS up to the Fermi level at 0 K gives the total number of electrons ($n$) of the system,

$$\int_0^{E_F} D(\varepsilon)d\,\varepsilon = n \qquad \text{2-1}$$

DOS diagram is the commonly used tool to characterize the electronic structure of solids. It is analogous to the molecular orbital diagrams and provides atomic-scale insights into the bonding interaction. Local/projected density of states (LDOS/PDOS) are the density of states for the selected atom and the specific angular momenta of the selected atoms, respectively.

### 2.3.2 Charge density distribution

Charge density of the system can be visualized to reveal the distribution of electrons graphically. Charge density difference, taking the adsorbed system as an example, indicates the difference

($\Delta\rho$) between the total charge density of the adsorbed system ($\rho_{AB}$) and those of the constituent units in their isolated states ($\rho_A$ and $\rho_B$) without further geometric optimizations,

$$\Delta\rho = \rho_{AB} - \rho_A - \rho_B \tag{2-2}$$

The 2/3-D charge density difference map offers valuable information on the preferred location of electrons and thus can be used to examine the adsorption induced charge redistributions.

### 2.3.3 Bader charge analysis

Bader charge analysis is a scheme proposed for quantitative analysis of charge distributions. Within this scheme, molecules are divided into atoms based purely on the electronic charge density by utilizing the so-called zero flux surfaces. Such surface is 2-D plane on which the charge density is a minimum perpendicular to the surface. Typically, charge density reaches a minimum between atoms, and this forms a natural place to separate atoms from each other. The charge enclosed within the Bader volume can be viewed as a good approximation to the total electronic charge associated with the atom. In VASP, the Bader charge analysis is realized by a fast and robust algorithm implemented by Henkelman et al. which is well suited for large solid-state systems.[12]

### 2.3.4 Electron localization function

Electron localization function (ELF) is essentially a manifestation of the Pauli exclusion principle.[13] The electron associates with a so-called Fermi hole which is a direct result of the Pauli exclusion principle and describes the probability of finding another electron with the same spin. If the electron is strongly localized, all other electrons with the same spin are excluded from this specific hole region, except for the electron with an opposite spin. Correspondingly, the existence of a localized electron pair implies that there may exist a high probability of finding two electrons of opposite spin in a given region.

The application of ELF in analyzing chemical bonds has been well documented.[14,15] The value of ELF scales from 0 to 1 and has three typical values: 1 indicates high probability to find localized electron pairs either as a lone pair or as covalently bonded electrons; 0.5 implies the electron gas-like electron behavior and corresponds to metallic bond; 0 points to extremely low electron density or an ionic bond character.

## 2.4 References

(1) Kresse, G.; Hafner, J. Ab Initio Molecular Dynamics for Liquid Metals. *Phys. Rev. B* **1993**, *47* (1), 558–561.

(2) Kresse, G.; Hafner, J. Ab Initio Molecular-Dynamics Simulation of the Liquid-Metal–amorphous-Semiconductor Transition in Germanium. *Phys. Rev. B* **1994**, *49* (20), 14251–14269.

(3) Kresse, G.; Furthmüller, J. Efficiency of Ab-Initio Total Energy Calculations for Metals and Semiconductors Using a Plane-Wave Basis Set. *Comput. Mater. Sci.* **1996**, *6* (1), 15–50.

(4) Kresse, G.; Furthmüller, J. Efficient Iterative Schemes for Ab Initio Total-Energy Calculations Using a Plane-Wave Basis Set. *Phys. Rev. B* **1996**, *54* (16), 11169–11186.

(5) Blöchl, P. E. Projector Augmented-Wave Method. *Phys. Rev. B* **1994**, *50* (24), 17953–17979.

(6) Kresse, G. From Ultrasoft Pseudopotentials to the Projector Augmented-Wave Method. *Phys. Rev. B* **1999**, *59* (3), 1758–1775.

(7) Hafner, J. Ab-Initio Simulations of Materials Using VASP: Density-Functional Theory and Beyond. *J. Comput. Chem.* **2018**, *29* (13), 2044–2078.

(8) Mathew, K.; Sundararaman, R.; Letchworth-weaver, K.; Arias, T. A.; Hennig, R. G. Implicit Solvation Model for Density-Functional Study of Nanocrystal Surfaces and Reaction Pathways. *J. Chem. Phys.* **2014**, *140* (8), 084106.

(9) Fishman, M.; Zhuang, H. L.; Mathew, K.; Dirschka, W.; Hennig, R. G. Accuracy of Exchange-Correlation Functionals and Effect of Solvation on the Surface Energy of Copper. *Phys. Rev. B* **2013**, *87* (24), 245402.

(10) Kitchaev, D. A.; Ceder, G. Evaluating Structure Selection in the Hydrothermal Growth of $FeS_2$ Pyrite and Marcasite. *Nat. Commun.* **2016**, *7*, 13799.

(11) Garza, A.; Bell, A. T.; Head-Gordon, M. Is Subsurface Oxygen Necessary for the Electrochemical Reduction of $CO_2$ on Copper? *J. Phys. Chem. Lett.* **2018**, *9* (3), 601–606.

(12) Yu, M.; Trinkle, D. R. Accurate and Efficient Algorithm for Bader Charge Integration. *J. Chem. Phys.* **2011**, *134* (6), 1–19.

(13) Fuentealba, P., Chamorro, E. and Santos, J. C. Understanding and Using the Electron Localization. *Theor. Asp. Chem. React.* **2007**, *19*, 57–85.

(14) Silvi, B.; Savin, A. Classification of Chemical Bonds Based on Topological Analysis of Electron Localization Functions. *Nature* **1994**, *371*, 683–686.

(15) Tsuji, Y.; Dasari, P. L. V. K.; Elatresh, S. F.; Hoffmann, R.; Ashcroft, N. W. Structural Diversity and Electron Confinement in $Li_4N$: Potential for 0-D, 2-D, and 3-D Electrides. *J. Am. Chem. Soc.* **2016**, *138* (42), 14108–14120.

# Chapter 3  Descriptor of Catalytic Activity of Metal Sulfides for Oxygen Reduction Reaction: A Potential Indicator for Mineral Flotation

**Abstract:** Froth flotation has been widely used to separate sulfide minerals from sulfide ores, where the oxygen reduction reaction (ORR) plays a significant role as the cathodic reaction. However, the intrinsic ORR mechanism over sulfide minerals and its effect on the flotation performance remain unclear. Herein, we explored the intrinsic ORR mechanism over metal sulfides through density functional theory (DFT) calculations along with the computational hydrogen electrode (CHE) model. Our results revealed that pyrite ($FeS_2$) and chalcopyrite ($CuFeS_2$) exhibited similar ORR behavior to that over platinum (Pt) but not galena (PbS) and sphalerite (ZnS). The relative computational overpotentials for the ORR were consistent with the experimental trend in the order $Pt < FeS_2 < CuFeS_2 < PbS < ZnS$ and linearly correlate with the oxygen binding energies. We thus conclude that the distinct ORR behaviors originate from the different oxygen binding strengths which are determined by the underlying electronic structure. More importantly, we demonstrated that the DFT calculated bulk centroids of the occupied S 3p band for metal sulfides strongly correlate with the experimental rest potential of the sulfide mineral electrodes in xanthate solution, and consequently we established the descriptor–activity relationship. Using this relationship, we propose that the mechanism underlying the mixed potential model regarding the xanthate–sulfide mineral interaction is governed by the relative dominating role of the compositional metallic cation to the anionic sulfur in terms of the electronic structure around the Fermi level, which favors the formation of dixanthogen and metal-xanthate, respectively.

## 3.1 Introduction

Sulfide minerals constitute the major source of nonferrous base metals, which are conventionally recovered from ores through a froth flotation technology. To increase the flotation efficiency, short hydrocarbon chain collectors composed of a chemically reactive head group and a hydrophobic tail are added to the flotation process so that the collectors chemisorb on the target mineral surface, thereby increasing its surface hydrophobicity.[1–3] Xanthate is the most commonly used collector for sulfide minerals. However, its interaction with the sulfide mineral surfaces is complicated. According to the mixed potential model, the interaction could be treated as electrochemical reactions in which xanthate undergoes the anodic reaction while oxygen in the aerated flotation pulp cathodic reaction.[4,5] Here, the sulfide minerals act as a catalyst for the reactions. The intrinsic activity for the oxygen reduction reaction (ORR) is correlated with the measured rest potential of sulfide mineral surface. Studies have also shown that the rest potentials of different sulfide minerals match well with the catalytic activity trend for the ORR with the sequence pyrite > chalcopyrite > galena > sphalerite.[6] More importantly, the xanthate–mineral reaction products on the sulfide mineral surfaces can be tailored to be rich of either dixanthogen or metal xanthate depending on the difference of the rest potential and the equilibrium potential of dixanthogen/xanthate ($X_2/X^-$) regardless of the pulp pH and chain length of the xanthate homologue.[7] It has been further confirmed by electrochemical studies (e.g., open circuit potential and cyclic voltammetry) and spectroscopy analysis (e.g., FTIR and XPS) that the dominant xanthate–mineral reaction products contributing to the floatability of pyrite and galena are different and they are dixanthogen and metal xanthate, respectively.[7] Therefore, the catalytic activity of sulfide minerals for the ORR and thereby the rest potential can be used as an indicator toward the type of the surface reaction product which in turn can be used to guide the optimization of the froth flotation performance. However, systematic and fundamental insights into the underlying ORR mechanism over sulfide minerals in the context of promoting the flotation performance are still lacking.

In recent years, first-principles calculations have been demonstrated capable of explicating the intrinsic activity of catalysts for hydrogen evolution, oxygen reduction and methanol oxidation reactions.[8–12] The first principle descriptors, such as the d band theory of transition metal and alloy for the ORR,[13] the $e_g$ filling of perovskite for the ORR at room temperature,[14] the O p band theory of double perovskite for the oxygen evolution reaction,[15] and the O p band theory of conducting electron rich perovskite for the ORR at elevated temperatures,[16] strongly correlate with the catalytic activity. Therefore, density functional density (DFT) calculations (e.g., Gibbs free energy diagram, theoretical overpotential and density of states) on the ORR mechanism over sulfide minerals, coupled with the establishment of descriptor–activity relationships, are expected to offer guidance for the development of the surface compounds during the mineral flotation process.

In this study, the energetics of the ORR elementary steps over representative metal sulfides (i.e., $FeS_2$, $CuFeS_2$, PbS, and ZnS, representing pyrite, galena, chalcopyrite and sphalerite, respectively) were calculated through DFT calculations. Moreover, thermodynamic analysis on the basis of Gibbs free energy diagram, together with the electronic structure calculations were performed to establish the descriptor–activity relationships. The mechanism underlying the mixed potential theory of xanthate–mineral surface interaction was then discussed with the established relationship.

## 3.2 Results and Discussion

The oxygen reduction reaction (ORR) can proceed with either the two elementary step dissociative mechanism or the four elementary electron-proton step associative mechanism.[9,13,17] The previous studies have shown that the dissociative ORR mechanism requires the dissociation of oxygen molecules which involves considerable activation energy barrier, especially for catalyst that binds oxygen weakly.[18,19] As such, the associative mechanism was widely employed as the ORR model in many previous studies,[13,20,21] which was also the approach adopted in this study. Therefore, the Gibbs free energy diagram for the ORR, comprising the following four elementary steps, was constructed with the associative ORR mechanism,[11]

$$O_2(g) + 4H^+ + 4e^- + * \rightarrow OOH^* + 3H^+ + 3e^- \tag{3-1}$$

$$OOH^* + 3H^+ + 3e^- \rightarrow O^* + H_2O(l) + 2H^+ + 2e^- \tag{3-2}$$

$$O^* + H_2O(l) + 2H^+ + 2e^- \rightarrow OH^* + H_2O(l) + H^+ + e^- \tag{3-3}$$

$$OH^* + H_2O(l) + H^+ + e^- \rightarrow 2H_2O(l) + * \tag{3-4}$$

To build the ORR models, the cleavage planes of (111), (100), (112), (100) and (110) were adopted for Pt, $FeS_2$, $CuFeS_2$, PbS and ZnS, respectively, because they have been considered as stable and easily exposed planes, which have been extensively used as the model surfaces.[13,22–26] We subsequently built the relevant ORR models with the compositional metallic cations (*) on the surface as the active center, attempting to understand the distinct activities of these materials for the ORR (see Supporting Information in Appendix A for more details).[11,27] The adsorption models of intermediates over PbS(100) (a-d) and $FeS_2$(100) (e-h) are presented in Scheme 3.1.

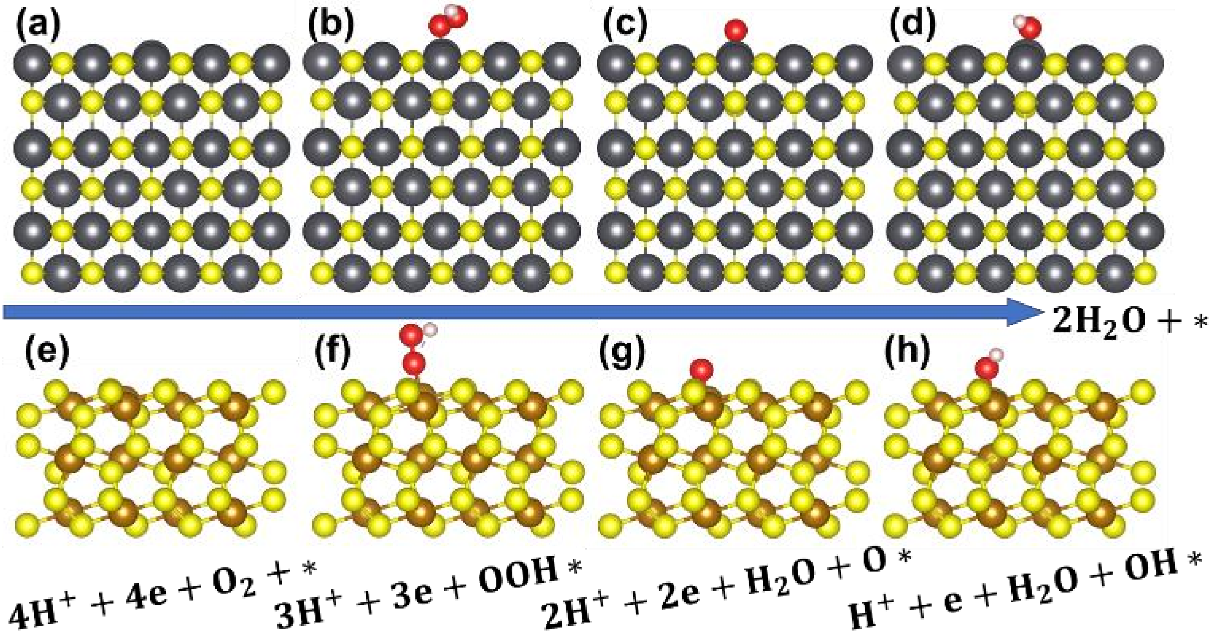

**Scheme 3.1** The optimized geometries of (a) bare PbS(100), (b) bare $FeS_2(100)$, (b)-(d) PbS(100) and (f)-(h) $FeS_2(100)$ with adsorbed ORR intermediates of OOH/*, O/* and OH/*, respectively (the coverage of intermediate is around 1/8 ML).

All potentials were calculated relative to the standard hydrogen electrode (SHE) throughout this study. Figure 3.1(a) shows the Gibbs free energy diagram for ORR over Pt(111), $FeS_2(100)$, $CuFeS_2(112)$_copper site, $CuFeS_2(112)$_iron site, PbS(100) and ZnS(110) at the equilibrium potential of 1.23 V at room temperature. The ORR performance over $CuFeS_2(112)$ was assumed to be equivalent to the average performance of that over the $CuFeS_2(112)$_copper site and $CuFeS_2(112)$_iron site and finally located between that of $FeS_2(100)$ and PbS(100). It should be noted that energy barriers are not included in the thermodynamic data in Figure 3.1(a). The energy barriers for the rate-limiting step is assumed to be equal to the highest free energy difference of the elementary reaction, which has been proven useful in rationalizing trends for electrochemical reactions.[28,29]

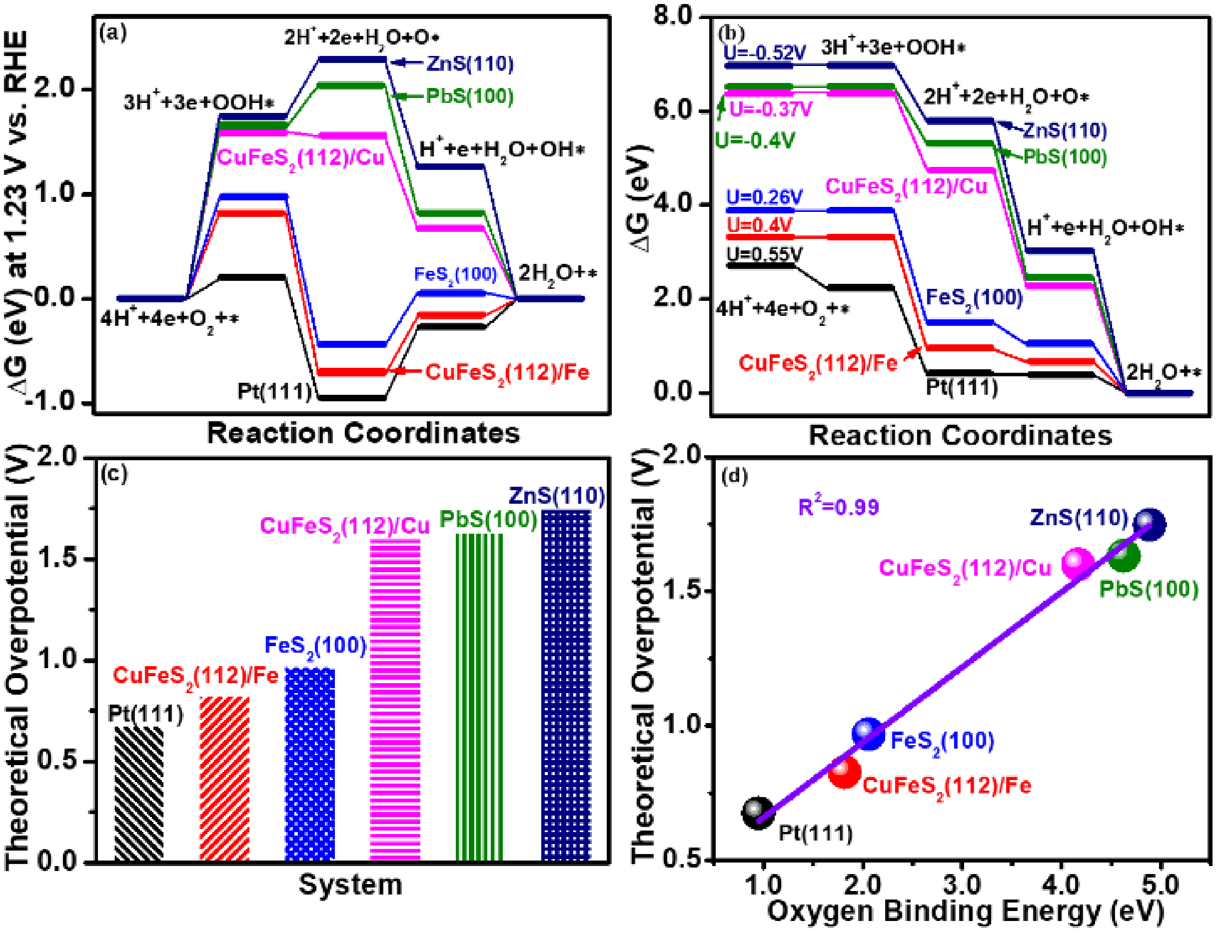

**Figure 3.1** Free energy diagrams for the ORR over Pt(111), CuFeS$_2$(112)_Fe, FeS$_2$(100), CuFeS$_2$(112)_Cu, PbS(100) and ZnS(110) (a) at 1.23 V and (b) at different potentials for different materials; (c) the theoretical overpotential for the ORR; (d) the theoretical overpotential plotted as a function of the oxygen binding energy.

For Pt(111) in Figure 3.1(a), the transition from O* to OH* [i.e., step (3)] requires the highest energy input among the four elementary reactions, indicating that reaction (3) is the rate-limiting step for the ORR over Pt(111), which agrees well with the previous computational studies.[13] In comparison, the transfer of a proton and an electron to the adsorbed O$_2$ [i.e., step (1)] is the rate-determining step for the ORR over metal sulfides, as verified by the electrochemical experiments.[30] The consistency between the computationally and experimentally identified rate-determining step for the ORR confirms the proposed hypothesis that thermodynamic analysis is capable of rationalizing the trends for electrochemical reactions involving oxygen on the basis of Gibbs free energy diagram.[13,31,32] Moreover, it is worth noting that the biggest difference along the reaction coordinates at the equilibrium potential is the second elementary step which involves the evolution of OOH* to O*. This reaction proceeds downhill over $FeS_2(100)$, $CuFeS_2(112)$ and Pt(111), suggesting the spontaneous occurrence of the ORR, whereas it reverses over PbS(100) and ZnS(110).

To quantitatively describe the distinct catalytic activity of Pt and metal sulfides for the ORR, the Gibbs free energy diagram was further constructed under the potentials (i.e., the onset potential) where all the ORR elementary steps proceed spontaneously. As shown in Figure 3.1(b), all materials require activation energy to initiate the ORR, since the calculated onset potentials are lower than the theoretical equilibrium potential of 1.23 V. Among others, Pt(111) requires the lowest activation energy to initiate ORR, exhibiting an onset potential of 0.55 V, versus 0.26 V for $FeS_2(100)$ and 0.03 V for $CuFeS_2(112)$. However, the onset potential over PbS(100) and ZnS(110) are −0.4 V and −0.52 V, respectively, suggesting considerable higher activation energies needed. In addition, theoretical overpotentials, i.e., the difference between the thermodynamic equilibrium potential and the theoretical onset potential, were calculated on the basis of the Gibbs free energy diagram. The use of theoretical overpotential to evaluate catalyst activity has been extensively employed, and good correlations have been verified by previous studies.[11,33–35] The relative magnitudes of the overpotentials [Figure 3.1(c)] illustrate that the catalytic activity of the materials for the ORR decreases in the order Pt > $FeS_2$ > $CuFeS_2$ > PbS > ZnS, in good agreement with the experimentally observed catalytic activity trend.[6]

The distinct ORR behaviors over the materials can be attributed to the material's ability to bind oxygen.[18,36] Figure 3.1(d) summarizes the calculated reaction energetics of atomic oxygen on the surface of the minerals of interest. Apparently, Pt(111) binds oxygen strongly and exhibits the highest oxygen chemisorption energy among the materials studied, in accordance with the identified rate-limiting step of Pt(111) for the ORR. In contrast, metal sulfides present lower oxygen chemisorption energies which drives reaction (1) to be the rate-limiting step. Moreover, the strong binding ability of Pt(111), $FeS_2$(100) and $CuFeS_2$(112) to atomic oxygen leads to the exothermic process of step (2). In comparison, step (2) is endothermic over PbS(100) and ZnS(110) due to the weak oxygen binding ability. It is, therefore, concluded that the distinct ORR performances [Figure 3.1(a)] over Pt and metal sulfides originate from the different oxygen binding capabilities. This is further supported by the Sabatier principle and the volcanic relation which relate the catalytic activity with the adsorbate binding strengths.[13,18] However, it is noted that the overall ORR behaviors over $FeS_2$(100) and $CuFeS_2$(112) are closer to that over Pt(111) than those over PbS(100) and ZnS(110) in spite of the rate-limiting step differences. The theoretical overpotentials were further plotted against the corresponding oxygen binding energies in Figure 3.1(d). The linear correlation indicates that both the theoretical overpotential and the oxygen binding energy can serve as good computational descriptors for predicting the catalytic activity of metal sulfides for the ORR. However, the two descriptors cannot be directly linked with the inherent attributes of the underlying materials because an effective descriptor requires the elucidation of the intrinsic factors responsible for the distinct catalytic activities for the ORR.

In this study, we have attributed the distinct catalytic activities for the ORR to the different oxygen binding energies. It is well known that the binding ability of the surface to the ORR intermediates is governed by the underlying electronic structure.[37–39] To achieve this, electronic structures, with an emphasis on the projected density of states (PDOS), were calculated for the bulk materials plus sulfur [Figures 3.2(a)-(f)].

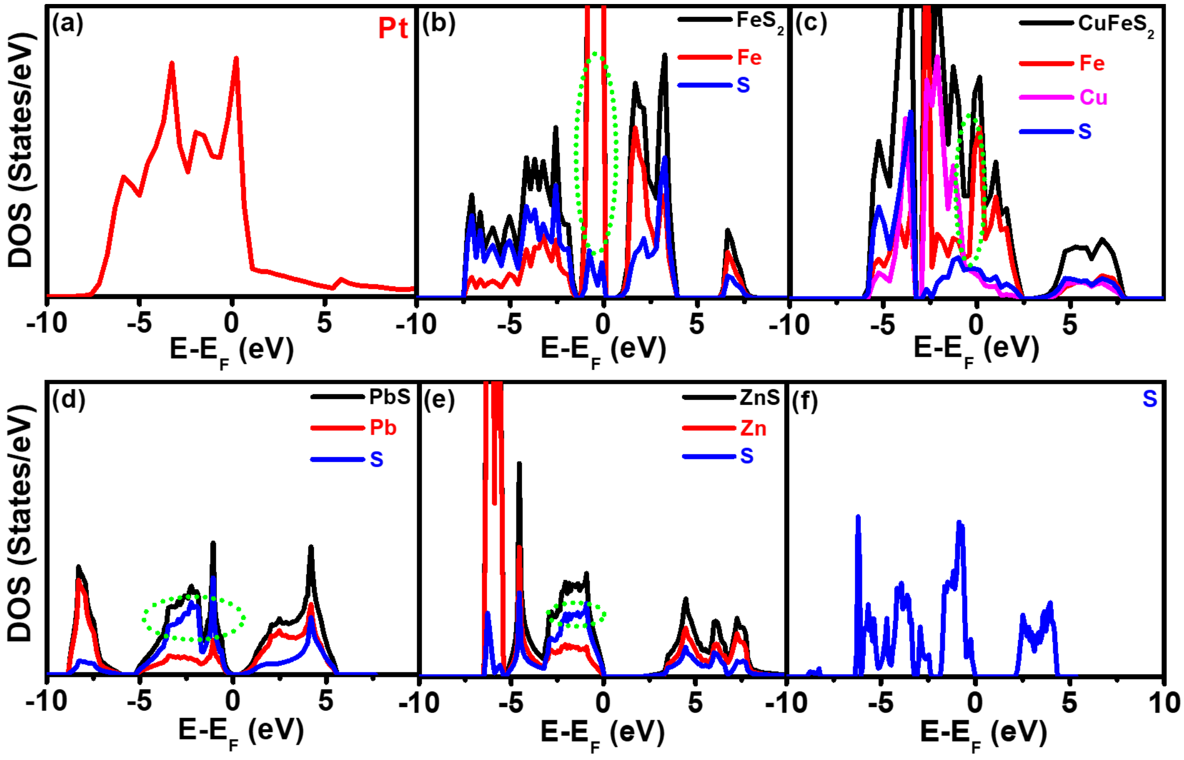

**Figure 3.2** Projected density of states (PDOS) calculated by DFT for bulk crystals (a) Pt, (b) $FeS_2$, (c) $CuFeS_2$, (d) PbS, (e) ZnS and (f) S.

Figures 3.2(b) and (c) reveal that the compositional metallic cations of $FeS_2$ and $CuFeS_2$ dominate the electronic states around the Fermi level, since the metallic cations contribute more to the total electronic states than that from the sulfur anion. This agrees well with the study on iron and copper sulfides, where the highest occupied state of pyrite was found to arise from the 3d non-bonding orbital of Fe, and the topmost part of the valence band of chalcopyrite comprises a mixture of Fe 3d, Cu 3d and S 3p orbitals. However, the S 3p state predominantly contributes to the topmost valence band for both PbS [Figure 3.2(d)] and ZnS [Figure 3.2(e)]. Clearly, the electronic structures of $FeS_2$ and $CuFeS_2$ resemble that of Pt [Figure 3.2(a)] while those of PbS and ZnS resemble that of S [Figure 3.2(f)]. The contrasting electronic features of the materials (i.e., Pt, $FeS_2$ and $CuFeS_2$ versus PbS and ZnS) around the Fermi energy are consistent with the distinct catalytic activity for the ORR which can be understood from the d band theory.

The d band model was initially developed to correlate the d band center (relative to the Fermi level) of the metallic cation with the catalytic activity trend of transition metals through predicting the surface–intermediate bond strength.[40,41] According to this theory, the energy of the metal d states relative to the Fermi level can be a qualitative indicator for the bond strength, the higher the d states are in energy relative to the Fermi level, the higher in energy the antibonding states and consequently the stronger the bonding strength. Therefore, we conjecture that the metallic cation dominated nature of $FeS_2$ and $CuFeS_2$ is the underlying reason for the similar ORR behaviors to that over Pt, as revealed by the Gibbs free energy diagram in Figure 3.1(a) and oxygen chemisorption energies in Figure 3.1(d). Accordingly, the sulfur dominated electronic feature around the Fermi level of PbS and ZnS also matches with the lower catalytic activities for the ORR. The correlation between the d band center of the metallic cation and the catalytic activity is further confirmed by the study that the stronger binding interactions toward intermediate over transition metal (i.e., Mo or W) dichalcogenides than that over Ag(111) was attributed to its closer d-band centers (relative to the Fermi level) of the metallic cations.[42] However, the d band model has its own limitations in terms of its generality. For example, even for the transition metal catalysts, the d band center alone fails to reflect the corresponding trends of catalytic activity for the metallic cations from different rows in the periodic table.[43] Another typical example is encountered by Y. Shao-Horn and D. Morgan in the establishment of the descriptor–activity relationship for the catalytic activity of the perovskite for the ORR.[16] They found that the correlation between the activity and the bulk O p-band center is much better than that with the bulk d-band center, exhibiting $R^2$ of 0.87 and 0.06, respectively. Therefore, to extend the observed regularity above from the representative metal sulfides to general sulfide minerals, a descriptor different from the d band center need to be established.

In Figure 3.2 (a)-(f), it is observed that the band center of the sulfur moves more closely to the Fermi level than that of the metallic cation as schematically illustrated in the inset of Figure 3.3(a), indicative of a potential relationship between the band feature of the sulfur anion and the catalytic activity for the ORR. Given that all metal sulfides contain sulfur and the metal sulfides normally possess non-ideal cleavage planes, we calculated the occupied bulk S-p band center by taking the centroid of the occupied projected density of states of S 3p states relative to the Fermi level (i.e., the bulk descriptor). To verify the effectiveness of the descriptor, the experimental rest potentials of the representative sulfide minerals together with another seven sulfide minerals are plotted against the bulk descriptors of the corresponding metal sulfides in Figure 3.3(a). The rest potential denotes the measured equilibrium potential of the metal sulfide electrode when the anodic reactions and cathodic reactions reach an equilibrium state. The experimental rest potential values were obtained from the classic paper published by S. A. Allison et al.[7] To our knowledge, the results from the group of S. A. Allison are the only available systematic and well established experimental rest potential values for such a wide range of sulfide minerals. Apparently, the experimental rest potentials correlate well with the bulk descriptors, which verifies the effectiveness of the underlying descriptor–activity relationship. The effectiveness of the descriptor is further confirmed by the linear correlation of the bulk descriptor and the oxygen reaction energies as shown in Figure 3.3(c). Moreover, the charges of the adsorbed oxygen calculated with the Bader charge scheme also correlate with the descriptor values, as shown in Figure 3.3(c). Therefore, we propose that the bulk descriptor can serve as effective descriptor for catalytic activity of sulfide minerals for the ORR. More importantly, the proposed bulk descriptor can be straightforwardly calculated with the first-principles methods regardless of the surface structure and chemistry.

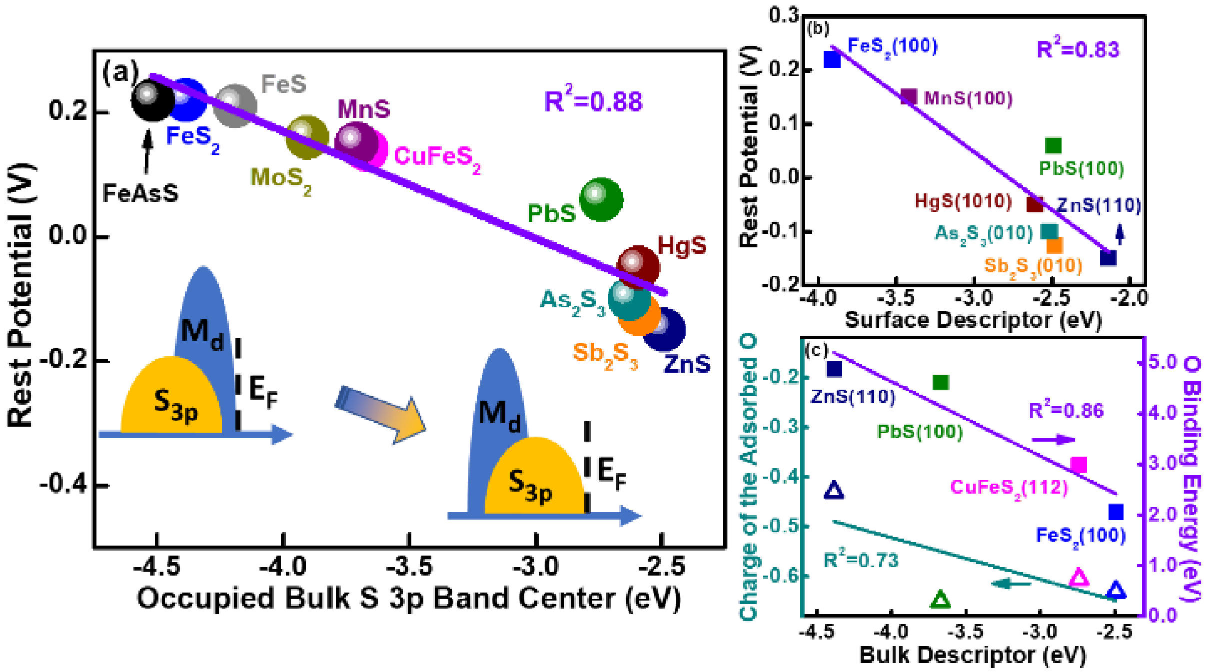

**Figure 3.3** (a) The experimental rest potentials plotted against the bulk S p-band center relative to the Fermi energy level; the inset illustrates the refined model reflecting the gradual geometrical change of PDOS following the activity trend for the ORR; (b) the experimental rest potentials plotted against the occupied surface S p-band center relative to the Fermi energy level; (c) the charges of the adsorbed oxygen (i.e., solid squares) and the oxygen binding energies (i.e., open and up triangles) as a function of the bulk descriptor (the occupied bulk S 3p band center relative to the Fermi energy level).

For comparison, the centroids of S 3p band of sulfur on the optimized surfaces of metal sulfides with ideal cleavage planes were calculated and plotted against the rest potentials. As illustrated in Figure 3.3(b), the surface descriptors also correlate with the corresponding rest potentials with a $R^2$ of 0.83, but fails to present any further improvements than the bulk descriptors. This is probably due to the fact that the sulfide minerals used for the rest potential measurement composed of different cleavage planes, while the calculations were conducted on the ideal surface cleavages. As a result, the catalytic activity for the ORR is better predicted by descriptors calculated from bulk crystals. Moreover, we also calculated the bulk occupied d-band center of the constituent metallic cation, as shown in Figure A2 in the Appendix A. As expected, the experimental rest potential exhibits a weaker correlation with the metal d-band center with a $R^2$ of 0.71 than that of the bulk S p-band center (0.88).

With the established descriptor– activity relationship, the mechanism underlying the mixed potential model regarding the xanthate–sulfide mineral interaction within the regime of flotation can be well understood. On the basis of the descriptor–activity relationship, we hypothesize that the bulk descriptor reflects the degree of the contribution of the constituent metallic cation to the catalytic activity of the whole mineral. Taking pyrite and galena as an example, the floatability of pyrite and galena depends on the formation of dixanthogen and metal xanthate, respectively. The lower descriptor value of pyrite indicates that the metallic cation dominates the electronic structure around the Fermi level and thereby facilitates its interaction with the ORR intermediates. In this case, oxygen obtains electrons at the cathode and gets reduced, while xanthate anions provide electrons at anode and are oxidized to dixanthogen. However, the higher descriptor value of galena highlights the dominating role of the sulfur anion over the electronic structure around the Fermi level, resulting in the competition between the adsorption of the ORR intermediates over the sulfur anion and the metallic cations. The competitive adsorption weakens the catalytic role of the metallic active center and leads to the considerably lower catalytic activity of galena for the ORR. As a result, oxygen tends to obtain electrons from the sulfur anion and consequently promotes the interaction between the metallic cation and the xanthate anion (i.e., metal-xanthate). The proposed mechanism is further supported by previous DFT studies that oxygen adsorbs more easily on metallic cation of pyrite, while sulfur anion of galena binds to oxygen more easily.[44] Therefore, the established descriptor–activity relationship provides insights into the mechanism underlying the mixed potential model which further highlights its potential in benefiting the mineral flotation engineering. In addition, due to the superior catalytic activity for the ORR, both S- based noble (e.g., Ru) and base metal (e.g., Fe, Co and Ni) chalcogenides have been extensively explored as potential alternatives to the Pt-based catalysts for the ORR in polymer electrolyte membrane fuel cells (PEMFCs).[45–50] Therefore, the established descriptor–activity relationship can also potentially serve as the guidance for first principle design of metal chalcogenide catalysts for the ORR.

### 3.3 Conclusions

In summary, we have carried out density functional theory (DFT) calculations combined with the computational hydrogen electrode (CHE) model to explore the intrinsic mechanism of oxygen reduction reaction (ORR) over sulfide minerals. The Gibbs free energy diagram reveals that the transfer of proton to the adsorbed O is the rate-limiting step of the ORR over Pt, while the transfer of proton and electron to the adsorbed $O_2$ molecule is the rate-limiting step of metal sulfides for the ORR. Despite the differences in the rate-limiting step, the ORR behaviors over $FeS_2$ and $CuFeS_2$ are similar to that over Pt, but different from those over PbS and ZnS, arising from the different oxygen binding energies. Meanwhile, the relative theoretical overpotentials are in good agreement with the experimental trend in the order of Pt < $FeS_2$ < $CuFeS_2$ < PbS < ZnS and linearly correlate with the oxygen binding energies. Moreover, the projected density of state (PDOS) illustrates that the electronic states around the Fermi level of Pt, $FeS_2$ and $CuFeS_2$

are predominately contributed by the compositional metallic cations, whereas the sulfur anion of PbS, ZnS and bulk S dominants the electronic states around the Fermi level. The distinct ORR behaviors are, therefore, concluded to originate from the different oxygen binding energies which are governed by the underlying electronic structure. More importantly, we establish the underlying descriptor–activity relationship, where the bulk centroids (relative to the Fermi level) of the occupied S 3p band of metal sulfides strongly correlate with the experimental rest potentials for such sulfide minerals in xanthate solutions. Based on the relationship, the mixed potential model regarding the mineral−xanthate interaction is proposed to associate with the ion that dominates the electronic states around the Fermi energy level. The dominating role of metallic cation contributes to a higher catalytic activity for the ORR and facilitates the formation of dixanthogen, while the dominating role of sulfur anion results in a lower catalytic activity for the ORR and favors the formation of metal xanthate. Therefore, this work provides fundamental insights into the intrinsic mechanism of the ORR over sulfide minerals, and the established descriptor–activity relationship holds the promise in prediction of the overall electrochemical behavior of sulfide minerals and hence can potentially benefits the mineral flotation.

## 3.4 References

(1) Zhang, H.; Kim, Y. K.; Hunter, T. N.; Brown, A. P.; Lee, J. W.; Harbottle, D. Organically Modified Clay with Potassium Copper Hexacyanoferrate for Enhanced $Cs^+$ Adsorption Capacity and Selective Recovery by Flotation. *J. Mater. Chem. A* **2017**, *5* (29), 15130–15143.

(2) Xing, Y.; Gui, X.; Cao, Y. The Hydrophobic Force for Bubble–particle Attachment in Flotation–a Brief Review. *Phys. Chem. Chem. Phys.* **2017**, *19* (36), 24421–24435.

(3) Anthore-Dalion, L.; Liu, Q.; Zard, S. Z. A Radical Bidirectional Fragment Coupling Route to Unsymmetrical Ketones. *J. Am. Chem. Soc.* **2016**, *138* (27), 8404–8407.

(4) Chandra, A. P.; Gerson, A. R. A Review of the Fundamental Studies of the Copper Activation Mechanisms for Selective Flotation of the Sulfide Minerals, Sphalerite and Pyrite. *Adv. Colloid Interface Sci.* **2009**, *145* (1–2), 97–110.

(5) Xie, L.; Wang, J.; Shi, C.; Huang, J.; Zhang, H.; Liu, Q.; Liu, Q.; Zeng, H. Probing Surface Interactions of Electrochemically Active Galena Mineral Surface Using Atomic Force Microscopy. *J. Phys. Chem. C* **2016**, *120* (39), 22433–22442.

(6) Rand, D. A. J. Oxygen Reduction on Sulphide Minerals: Part III. Comparison of Activities of Various Copper, Iron, Lead and Nickel Mineral Electrodes. *J. Electroanal. Chem. Interfacial Electrochem.* **1977**, *83* (1), 19–32.

(7) Allison, S.; Goold, L.; Granville, A. A Determination of the Products of Reaction Between Various Sulfide Minerals and Aqueous Xanthate Solution, and a Correlation of the Products with Electrode Rest Potentials. *Metall. Trans.* **1972**, *3* (10), 2613–2618.

(8) Friebel, D.; Louie, M. W.; Bajdich, M.; Sanwald, K. E.; Cai, Y.; Wise, A. M.; Cheng, M.

J.; Sokaras, D.; Weng, T. C.; Alonso-Mori, R.; et al. Identification of Highly Active Fe Sites in (Ni,Fe)OOH for Electrocatalytic Water Splitting. *J. Am. Chem. Soc.* **2015**, *137* (3), 1305–1313.

(9) Seh, Z. W.; Kibsgaard, J.; Dickens, C. F.; Chorkendorff, I.; Nørskov, J. K.; Jaramillo, T. F. Combining Theory and Experiment in Electrocatalysis: Insights into Materials Design. *Science* **2017**, *355* (6321), 1–12.

(10) Nørskov, J. K.; Bligaard, T.; Rossmeisl, J.; Christensen, C. H. Towards the Computational Design of Solid Catalysts. *Nat. Chem.* **2009**, *1* (1), 37–46.

(11) Tritsaris, G. A.; Nørskov, J. K.; Rossmeisl, J. Trends in Oxygen Reduction and Methanol Activation on Transition Metal Chalcogenides. *Electrochim. Acta* **2011**, *56* (27), 9783–9788.

(12) Hammer, B.; Nørskov, J. K. Theoretical Surface Science and Catalysis – Calculations and Concepts. *Adv. Catal.* **2000**, *45*, 71–129.

(13) Nørskov, J. K.; Rossmeisl, J.; Logadottir, A.; Lindqvist, L.; Kitchin, J. R.; Bligaard, T.; Jónsson, H. Origin of the Overpotential for Oxygen Reduction at a Fuel-Cell Cathode. *J. Phys. Chem. B* **2004**, *108* (46), 17886–17892.

(14) Suntivich, J.; Gasteiger, H. A.; Yabuuchi, N.; Nakanishi, H.; Goodenough, J. B.; Shao-horn, Y. On Perovskite Oxide Catalysts for Fuel Cells and Metal–Air Batteries. *Nat. Chem.* **2011**, *3* (7), 546–550.

(15) Grimaud, A.; May, K. J.; Carlton, C. E.; Lee, Y.-L.; Risch, M.; Hong, W. T.; Zhou, J.; Shao-Horn, Y. Double Perovskites as a Family of Highly Active Catalysts for Oxygen Evolution in Alkaline Solution. *Nat. Commun.* **2013**, *4*, 1–7.

(16) Lee, Y.-L.; Kleis, J.; Rossmeisl, J.; Shao-Horn, Y.; Morgan, D. Prediction of Solid Oxide Fuel Cell Cathode Activity with First-Principles Descriptors. *Energy Environ. Sci.* **2011**, *4* (10), 3966–3970.

(17) Blizanac, B. B.; Lucas, C. A.; Gallagher, M. E.; Arenz, M.; Ross, P. N.; Markovic, N. M. Anion Adsorption, CO Oxidation, and Oxygen Reduction Reaction on a Au(100) Surface: The PH Effect. *J. Phys. Chem. B* **2004**, *108* (2), 625–634.

(18) Hong, W. T.; Risch, M.; Stoerzinger, K. A.; Grimaud, A.; Suntivich, J.; Shao-Horn, Y. Toward the Rational Design of Non-Precious Transition Metal Oxides for Oxygen Electrocatalysis. *Energy Environ. Sci.* **2015**, *8* (5), 1404–1427.

(19) Nørskov, J. K.; Bligaard, T.; Logadottir, A.; Bahn, S.; Hansen, L. B.; Bollinger, M.; Bengaard, H.; Hammer, B.; Sljivancanin, Z.; Mavrikakis, M.; et al. Universality in Heterogeneous Catalysis. *J. Catal.* **2002**, *209* (2), 275–278.

(20) Stamenkovic, V.; Mun, B. S.; Mayrhofer, K. J. J.; Ross, P. N.; Markovic, N. M.; Rossmeisl, J.; Greeley, J.; Nørskov, J. K. Changing the Activity of Electrocatalysts for Oxygen Reduction by Tuning the Surface Electronic Structure. *Angew. Chemie Int. Ed.* **2006**, *45* (18), 2897–2901.

(21) Viswanathan, V.; Hansen, H. A.; Rossmeisl, J.; Nørskov, J. K. Universality in Oxygen Reduction Electrocatalysis on Metal Surfaces. *ACS Catal.* **2012**, *2* (8), 1654–1660.

(22) McCrum, I. T.; Hickner, M. A.; Janik, M. J. First-Principles Calculation of Pt Surface Energies in an Electrochemical Environment: Thermodynamic Driving Forces for Surface Faceting and Nanoparticle Reconstruction. *Langmuir* **2017**, *33* (28), 7043–7052.

(23) Andersson, K. J.; Ogasawara, H.; Nordlund, D.; Brown, G. E.; Nilsson, A. Preparation,

Structure, and Orientation of Pyrite $FeS_2$\{100\} Surfaces: Anisotropy, Sulfur Monomers, Dimer Vacancies, and a Possible Fes Surface Phase. *J. Phys. Chem. C* **2014**, *118* (38), 21896–21903.

(24) Chen, V. H. Y.; Mallia, G.; Martínez-Casado, R.; Harrison, N. M. Surface Morphology of $CuFeS_2$: The Stability of the Polar (112)/(112¯) Surface Pair. *Phys. Rev. B* **2015**, *92* (15), 1–9.

(25) Zherebetskyy, D.; Scheele, M.; Zhang, Y.; Bronstein, N.; Thompson, C.; Britt, D.; Salmeron, M.; Alivisatos, P.; Wang, L.-W. Hydroxylation of the Surface of PbS Nanocrystals Passivated with Oleic Acid. *Science* **2014**, *344* (6190), 1380–1384.

(26) Hamad, S.; Cristol, S.; Catlow, C. R. A. Surface Structures and Crystal Morphology of ZnS: Computational Study. *J. Phys. Chem. B* **2002**, *106* (42), 11002–11008.

(27) Alonso-Vante, N.; Malakho, I. V; Nikitenko, S. G.; Sa, E. R. The Structure Analysis of the Active Centers of Ru-Containing Electrocatalysts for the Oxygen Reduction. An in Situ EXAFS Study. *Electrochim. Acta* **2002**, *47* (22–23), 3807–3814.

(28) Karamad, M.; Hansen, H. A.; Rossmeisl, J.; Nørskov, J. K. Mechanistic Pathway in the Electrochemical Reduction of $CO_2$ on $RuO_2$. *ACS Catal.* **2015**, *5* (7), 4075–4081.

(29) Jacobsen, C. J. H.; Dahl, S.; Clausen, B. G. S.; Bahn, S.; Logadottir, A.; Nørskov, J. K. Catalyst Design by Interpolation in the Periodic Table: Bimetallic Ammonia Synthesis Catalysts. *J. Am. Chem. Soc.* **2001**, *123* (34), 8404–8405.

(30) Ahlberg, E.; Broo, A. E. Oxygen Reduction at Sulphide Minerals. 1. A Rotating Ring Disc Electrode (RRDE) Study at Galena and Pyrite. *Int. J. Miner. Process.* **1996**, *46* (1–2), 73–89.

(31) Siahrostami, S.; Li, G.-L.; Viswanathan, V.; Nørskov, J. K. One- or Two-Electron Water Oxidation, Hydroxyl Radical or $H_2O_2$ Evolution. *J. Phys. Chem. Lett.* **2017**, *8* (6), 1157–1160.

(32) Rosen, J.; Hutchings, G. S.; Lu, Q.; Rivera, S.; Zhou, Y.; Vlachos, D. G.; Jiao, F. Mechanistic Insights into the Electrochemical Reduction of $CO_2$ to CO on Nanostructured Ag Surfaces. *ACS Catal.* **2015**, *5* (7), 4293–4299.

(33) Man, I. C.; Su, H. Y.; Calle-Vallejo, F.; Hansen, H. A.; Martínez, J. I.; Inoglu, N. G.; Kitchin, J.; Jaramillo, T. F.; Nørskov, J. K.; Rossmeisl, J. Universality in Oxygen Evolution Electrocatalysis on Oxide Surfaces. *ChemCatChem* **2011**, *3* (7), 1159–1165.

(34) Kim, D.; Xie, C.; Becknell, N.; Yu, Y.; Karamad, M.; Chan, K.; Crumlin, E. J.; Nørskov, J. K.; Yang, P. Electrochemical Activation of $CO_2$ through Atomic Ordering Transformations of AuCu Nanoparticles. *J. Am. Chem. Soc.* **2017**, *139* (24), 8329–8336.

(35) Bajdich, M.; García-Mota, M.; Vojvodic, A.; Nørskov, J. K.; Bell, A. T. Theoretical Investigation of the Activity of Cobalt Oxides for the Electrochemical Oxidation of Water. *J. Am. Chem. Soc.* **2013**, *135* (36), 13521–13530.

(36) Stamenkovic, V.; Mun, B. S.; Mayrhofer, K. J. J.; Ross, P. N.; Markovic, N. M.; Rossmeisl, J.; Greeley, J.; Nørskov, J. K. Changing the Activity of Electrocatalysts for Oxygen Reduction by Tuning the Surface Electronic Structure. *Angew. Chemie Int. Ed.* **2006**, *45* (18), 2897–2901.

(37) Suntivich, J.; Gasteiger, H. A.; Yabuuchi, N.; Nakanishi, H.; Goodenough, J. B.; Shao-Horn, Y. Design Principles for Oxygen-Reduction Activity on Perovskite Oxide Catalysts for Fuel Cells and Metal-Air Batteries. *Nat. Chem.* **2011**, *3* (7), 546–550.

(38) Kim, C.; Jeon, H. S.; Eom, T.; Jee, M. S.; Kim, H.; Friend, C. M.; Min, B. K.; Hwang, Y. J. Achieving Selective and Efficient Electrocatalytic Activity for $CO_2$ Reduction Using Immobilized Silver Nanoparticles. *J. Am. Chem. Soc.* **2015**, *137* (43), 13844–13850.

(39) Zhang, J.; Vukmirovic, M. B.; Xu, Y.; Mavrikakis, M.; Adzic, R. R. Controlling the Catalytic Activity of Platinum-Monolayer Electrocatalysts for Oxygen Reduction with Different Substrates. *Angew. Chemie Int. Ed.* **2005**, *44* (14), 2132–2135.

(40) Nørskov, J. K. Electronic Factors in Catalysis. *Prog. Surf. Sci.* **1991**, *38* (2), 103–144.

(41) Hammer, B.; Nørskov, J. K. Why Gold Is the Noblest of All the Metals. *Nature* **1995**, *376* (6537), 238–240.

(42) Asadi, M.; Kim, K.; Liu, C.; Addepalli, A. V.; Abbasi, P.; Yasaei, P.; Phillips, P.; Behranginia, A.; Cerrato, J. M.; Haasch, R.; et al. Nanostructured Transition Metal Dichalcogenide Electrocatalysts for $CO_2$ Reduction in Ionic Liquid. *Science (80-. ).* **2016**, *353* (6298), 467–470.

(43) Bligaard, T.; Nørskov, J. K. *Chemical Bonding at Surfaces and Interfaces*; Elsevier B.V.: Oxford, 2008.

(44) Chen, J.; Li, Y.; Lan, L.; Guo, J. Interactions of Xanthate with Pyrite and Galena Surfaces in the Presence and Absence of Oxygen. *J. Ind. Eng. Chem.* **2014**, *20* (1), 268–273.

(45) Kulkarni, P.; Sanna Kotrappanavar, N.; Balakrishna, G. R.; Nagaraju, D. H.; Reddy, M. V. V. Nanostructured Binary and Ternary Metal Sulfides: Synthesis Methods and Its Application in Energy Conversion and Storage Devices. *J. Mater. Chem. A* **2017**, *5* (42), 22040–22094.

(46) Eftekhari, A. Tungsten Dichalcogenides ($WS_2$, $WSe_2$, and $WTe_2$): Materials Chemistry

and Applications. *J. Mater. Chem. A* **2017**, *5* (35), 18299–18325.

(47) Shao, M.; Chang, Q.; Dodelet, J.-P.; Chenitz, R. Recent Advances in Electrocatalysts for Oxygen Reduction Reaction. *Chem. Rev.* **2016**, *116* (6), 3594–3657.

(48) Wang, F.; Shifa, T. A.; Zhan, X.; Huang, Y.; Liu, K.; Cheng, Z.; Jiang, C.; He, J. Recent Advances in Transition-Metal Dichalcogenide Based Nanomaterials for Water Splitting. *Nanoscale* **2015**, *7* (47), 19764–19788.

(49) Chen, Z.; Higgins, D.; Yu, A.; Zhang, L.; Zhang, J. A Review on Non-Precious Metal Electrocatalysts for PEM Fuel Cells. *Energy Environ. Sci.* **2011**, *4* (9), 3167–3192.

(50) Feng, Y.; Gago, A.; Timperman, L.; Alonso-vante, N. Electrochimica Acta Chalcogenide Metal Centers for Oxygen Reduction Reaction: Activity and Tolerance. *Electrochim. Acta* **2011**, *56* (3), 1009–1022.

# Chapter 4 Revelation of the Nature of the Ligand−PbS Bond and Its Implication on Chemical Functionalization of PbS

**Abstract:** Chemical functionalization of metal sulfides by adsorption of specially designed ligands is of primary importance in efficiently manipulating the physicochemical properties of the target surface. Despite the widely studied ligand−metal molecular systems and the generally used binding energy concept, reports on the bond character of ligand−metal sulfide and its implication on the design of ligands with enhanced functionalities are rather scarce. Herein, using density functional theory (DFT) calculations, we studied the intrinsic binding mechanism of the typical S/O-terminated ligands and (100) surface of lead sulfide (PbS), with a particular emphasis on the ligand−PbS(100) bond character. Strikingly, the ligand−PbS(100) bond is found to be predominantly ionic with minor covalency, different from the conventional perception of covalent interaction. Further insights into the specific hydrophobization of PbS led us to demonstrate that the ligand electronegativity, rather than the commonly used binding energy, allows more accurate prediction of the relative hydrophobic functionality of the ligand toward PbS. Therefore, this study advances our fundamental understanding on the ligand−PbS(100) interaction and provides new perspectives on the first-principles design of ligands.

## 4.1 Introduction

Metal sulfides are versatile and cost-effective materials with broad engineering applications.[1–3] For example, the nanostructured lead sulfide (PbS) has been found valuable for electronic, optical and photovoltaic applications.[4,5] The synthesis of PbS nanomaterial with certain size and shape necessitates precise process control of the nucleation, growth and ultimately the external surface stability.[6,7] It is also well known that the natural lead sulfide (galena, PbS) is the primary source for elemental lead but it needs to be separated and purified from the host rock matrix through froth flotation, followed by the metal reduction. The flotation enrichment of galena relies on selectively rendering the galena surface hydrophobic.[8,9] Thus, efficient manipulation of the surface properties plays a critical role toward further extending the versatilities of metal sulfides and better utilizing the metal sulfide resources.

Chemical functionalization of materials with the assistance of ligands has been established as a feasible way to tune the resulting surface physicochemical properties.[10–12] Various experimental tools including atomic force microscope,[13] cyclic voltammetry,[14] X-ray photoelectron spectroscopy,[15] Fourier transform infrared spectroscopy,[16] and nuclear magnetic resonance[17] have been used to elucidate the ligand–metal sulfide interaction mechanisms, attempting to achieve the rational design of ligands with tailored functionalities. Among the commonly used ligands, the typical S- and O-tailed surfactants, such as oleic acid and xanthate, were extensively studied and have been widely reported to bind with metal ions on the surfaces of metal sulfides (e.g., CdS,[18] ZnS,[19] PbS[7] and so on).

In parallel with the rapidly developing experimental approaches, the accuracy of using the theoretical description of the surface chemical reactions has been largely improved.[20,21] The first-principles study, particularly the density functional theory (DFT) calculation, is increasingly becoming an indispensable tool to provide atomistic insights into the adsorption mechanism as well as the identification of key descriptors linking the intrinsic attribute of material with the activity of interest.[22–25] For instance, the remarkable d-band model has been successfully applied as computational guideline for the design of transition metal-based catalysts for a number of catalytic reactions.[26,27] Regarding the chemical functionalization of metal sulfides in the context of froth flotation, the computed binding energy is generally used to assess the relative ligand functionalitiy.[28–30] However, the trend of the binding energy, in certain case, fails to match with the trend of the corresponding experimental metric.[31] To date, this issue still represents a major challenge, leaving the fundamental understanding of ligand–metal sulfide binding ambiguous and the predictive descriptors for the rational design of ligand lacking.

To this end, we studied the interaction mechanism of the prototype metal sulfide PbS and a set of commonly used ligands using DFT calculations. The representative PbS(100) was constructed as the model surface. The typical surfactants used in metal sulfide froth flotation, dimethyl dithiocarbamate (DTC, $C_2H_6NCS_2$), ethyl xanthate (EX, $C_2H_5OCS_2$), dimethyl dithiophosphate (DTP, $C_2H_6O_2PS_2$) and acetic acid (AA, $C_2H_5CO_2$) were selected as the S- and the O-terminated ligands, respectively. Special attentions have been drawn on the resulting ligand−PbS(100) bond character by a systematic combination of density of states, charge density, Bader charge and electron localization function calculations. Importantly, the fundamental insights were successfully extended to the hydrophobization of PbS and are expected to be instructive in other fields with respect to the design of functionalized ligands.

## 4.2 Computational Details

The first-principles calculations were conducted with the Vienna *ab initio* Simulation Package (VASP).[32–35] The core electrons were treated by the projector augmented wave method.[36,37] The valence electronic configurations of the atoms adopted are H: $1s^1$, C: $2s^22p^2$, N: $2s^22p^3$, O: $2s^22p^4$, P: $3s^23p^3$, S: $3s^23p^4$ and Pb: $5d^{10}6s^26p^2$. The valence electrons were presented in planewaves with a kinetic energy cutoff of 450 eV. The exchange and correlation interactions were described by the Perdew-Burke-Ernzerhof generalized gradient approximation functional.[38]

The electronic occupancies were determined by the Gaussian smearing method at a smearing width of 0.05 eV, and the total energy extrapolated to zero broadening was used. The *k*-point mesh of 7 × 7 × 7, as sampled by the Monkhorst-Pack[39] scheme, was set for the PbS unit cell. The ligands were constructed with two carbon atoms in the tail and subsequently relaxed in a cubic simulation box of side length 30 Å at the Γ point only. The geometric structures were relaxed with the quasi-Newton algorithm until the total energy difference and the residual force were less than $10^{-6}$ eV and 0.02 eV/Å, respectively. Based on the fully optimized unit cell, a 2 × 3 slab model of PbS(100) with six atomic layers was built. A 30 Å vacuum layer was added between the slabs to minimize the interaction between the successive slabs. The top three atomic layers of PbS(100) were allowed to relax, whereas the bottom three layers were constrained at the bulk positions during optimization. The dipole correction in the direction perpendicular to the slab surface was included, and the spin polarization was also enabled.

The solvation effect was evaluated by the continuum implicit solvation model (VASPsol) implemented in VASP, which has been successfully employed for many interfacial adsorption studies.[40–43] Within this model, the thermodynamically-averaged effect of water is replaced by the electrostatic response of a continuum dielectric cavity along with the corrections for cavity formation and dispersion energies, in order to avoid the computationally prohibitive sampling of explicit solvent configurations. More details on the VASPsol can be found in Appendix C. Finally, the ligand−PbS(100) binding energy was calculated as,

$$\Delta E_{\mathrm{ads}} = E_{adsorbate/surface} - E_{adsorbate\_surface} \tag{4-1}$$

where $\Delta E_{\text{ads}}$ is the adsorption energy, $E_{adsorbate/surface}$ is the energy of the ligand–PbS(100) system, and $E_{adsorbate\_surface}$ is the energy of the reference system where the ligand sits in the middle of the vacuum layer.

The charge density difference map was constructed as,

$$\Delta\rho = \rho_{\text{X*PbS(100)}} - \rho_{\text{PbS(100)}} - \rho_{\text{X}} \qquad 4\text{-}2$$

where $\rho_{\text{X*PbS(100)}}$ is the charge density of the bound system, $\rho_{\text{PbS(100)}}$ and $\rho_{\text{X}}$ are the charge densities of the PbS(100) and the ligand without further geometric relaxations, respectively.

The electronegativity of the ligands was calculated with Gaussian [ub3lyp/6-311++g(3df,3pd)].[44–46] The previously optimized ligands in VASP were used without further optimizations for the corresponding anion and cation states. The electronegativity was calculated as,[47,48]

$$\chi = \frac{(IE+EA)}{2} \qquad 4\text{-}3$$

$$IE = IE_{\text{v}} = E_{tot}(X^{+}) - E_{tot}(X) \qquad 4\text{-}4$$

$$EA = EA_{\text{v}} = E_{tot}(X) - E_{tot}(X^{-}) \qquad 4\text{-}5$$

where $\chi$ is the electronegativity, $IE$ is the vertical ionization energy and $EA$ is the vertical electron affinity.

## 4.3 Results

The optimized PbS unit cell and PbS(100) are displayed in Figure 4.1. Clearly, PbS possesses a rock-salt structure where both the constituent Pb and S ions are octahedrally coordinated. The calculated lattice constants of $a = b = c = 6.01$ Å and the surface energy of 13 meV/Å$^2$ are close to the experimental lattice constant (5.93 Å)[49] and the surface energy (12.31 meV/Å$^2$) computed in previous study,[6] respectively, which in turn validates the reliability of the current computational method. The projected density of states (PDOS) of the optimized PbS(100) and bulk were also obtained. It is found that the electronic structures of S and Pb on PbS(100) closely resemble those in the bulk, as shown in Figure 4.1(b). Specifically, the PDOS of the clean PbS(100) highlights three typical regions in the range of −15 to 0 eV, i.e., the low valence band (VB) at –12.89 to −11.09 eV, the middle VB at −8.54 to –5.95 eV and the upper VB at −4.41 eV to the Fermi level (0 eV).

The low and middle VB regions comprise mainly the S 3s and the Pb 6s states, respectively. These deeply lying S 3s and Pb 6s states arise from the relative stabilization of the s electron pairs and become inert during the bonding interactions.[50] The high VB encompasses mostly the S 3p states, in contrast to the conduction band where the Pb 6p constitutes the major component. Notably, the S 3p states slightly hybridize with the limited Pb 6p states in the high VB region but with a dominant S 3p character, while the S and Pb orbitals barely overlap in the low and middle VB regions. These features indicate a very limited covalent nature of the S−Pb bond.[51,52] Overall, the energies, widths and compositions of the calculated electronic structure of PbS(100) agree well with the reported photoemission spectra.[53,54]

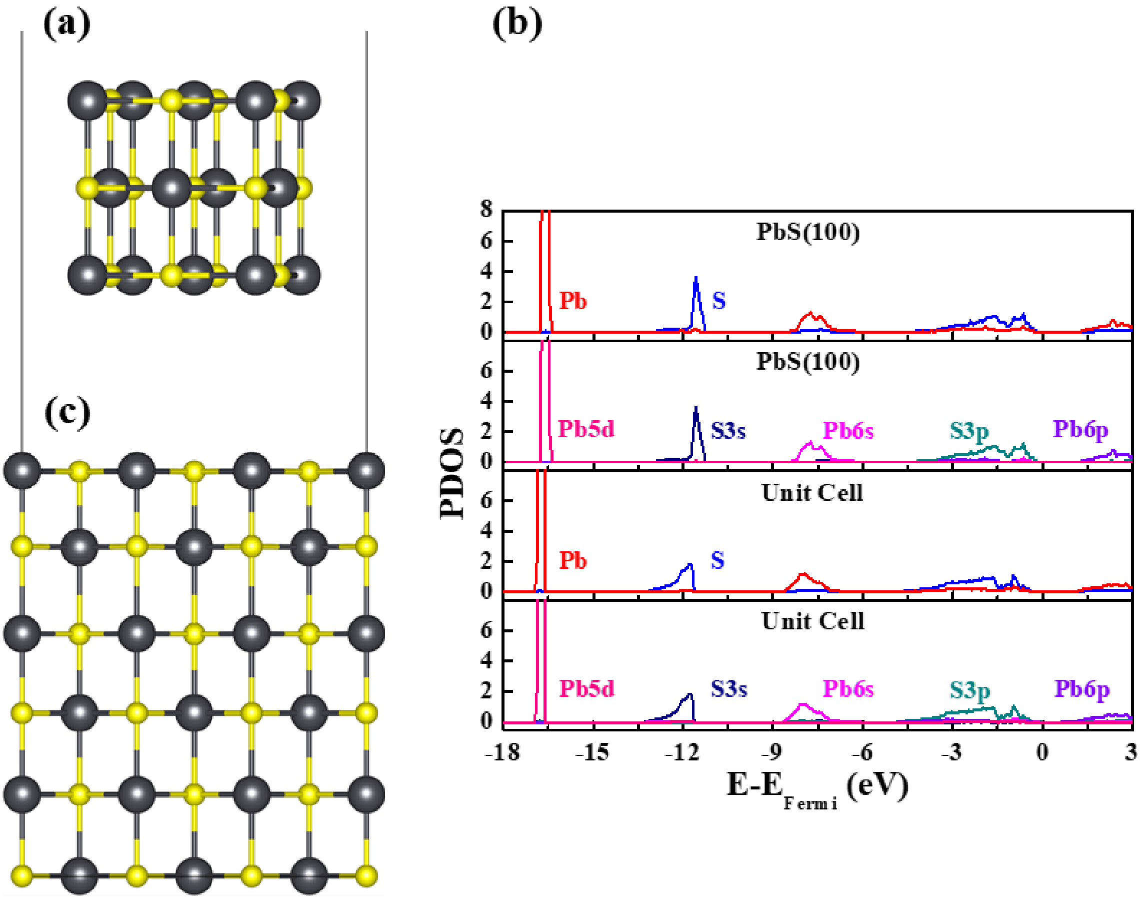

**Figure 4.1** (a) The optimized bulk PbS, (b) PDOS of Pb and S ions on PbS(100) and in bulk, (c) side view of the optimized PbS(100).

We then simulated the adsorption of DTC, EX, DTP and AA on the relaxed PbS(100) in a bridging bidentate pattern, as illustrated in Scheme 4.1.[31,55] The optimized adsorption configurations share similar features regardless of the different types of the ligands. The sulfur or oxygen ions from the ligand bind with two adjacent lead ions on PbS(100).

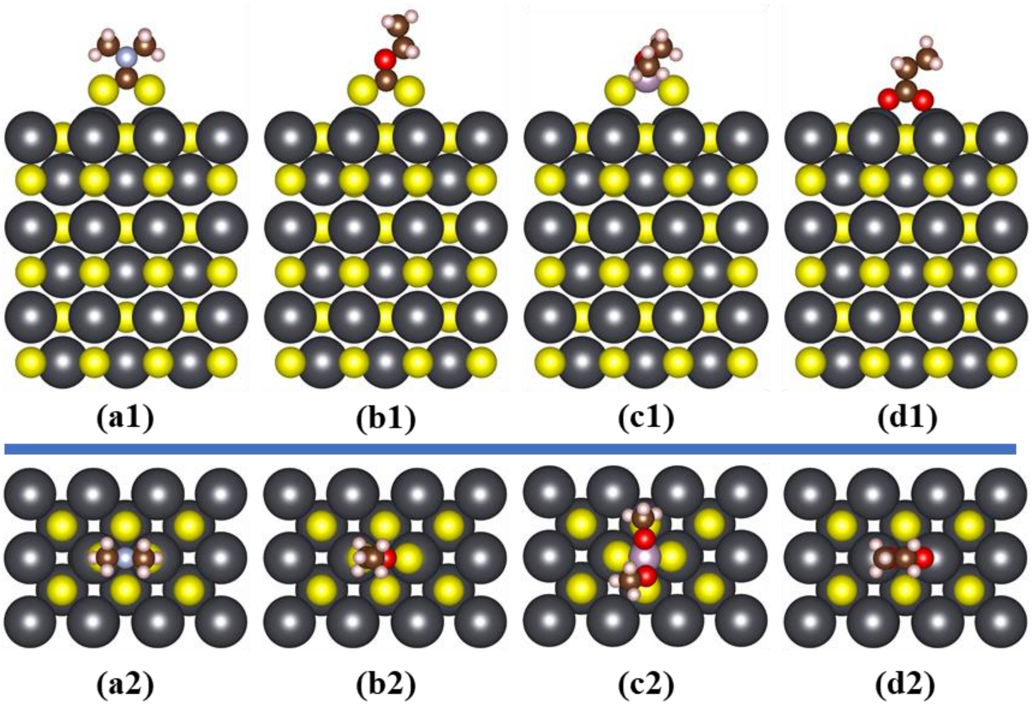

**Scheme 4.1** (a1−d1) Front views and (a2−d2) top views of (a) DTC/PbS(100), (b) EX/PbS(100), (c) DTP/PbS(100) and (d) AA/PbS(100). The atoms include H, white; C, brown; N, cyan; O, red; P, magenta; S, yellow and Pb, black.

The calculated average bond lengths of Pb–X are 2.904 Å, 2.899 Å, 2.892 Å and 2.400 Å for DTC, EX, DTP and AA, respectively. The relative bond length implies differences in the binding affinities of the ligands toward lead sulfide and agrees with the computed adsorption energies following the order DTC (–0.38 eV) > EX (–0.543 eV) > DTP (–0.818 eV) > AA (–1.602 eV). Apparently, AA binds more strongly with PbS(100) than those S-tailed ligands. Moreover, we evaluated the effect of water molecules on the adsorption energy using the implicit $\mathrm{VASP_{sol}}$ model. Under this model, the above interaction energies increase accordingly to –0.29 eV, –0.517 eV, –0.735 eV and –1.143 eV. Despite the weakened ligand–PbS(100) binding strength due to the implicit water molecules, the binding affinity trend remains unchanged. This is in good agreement with previous DFT studies using the S-tailed ligands with/without the presence of explicit water molecules.[29,31]

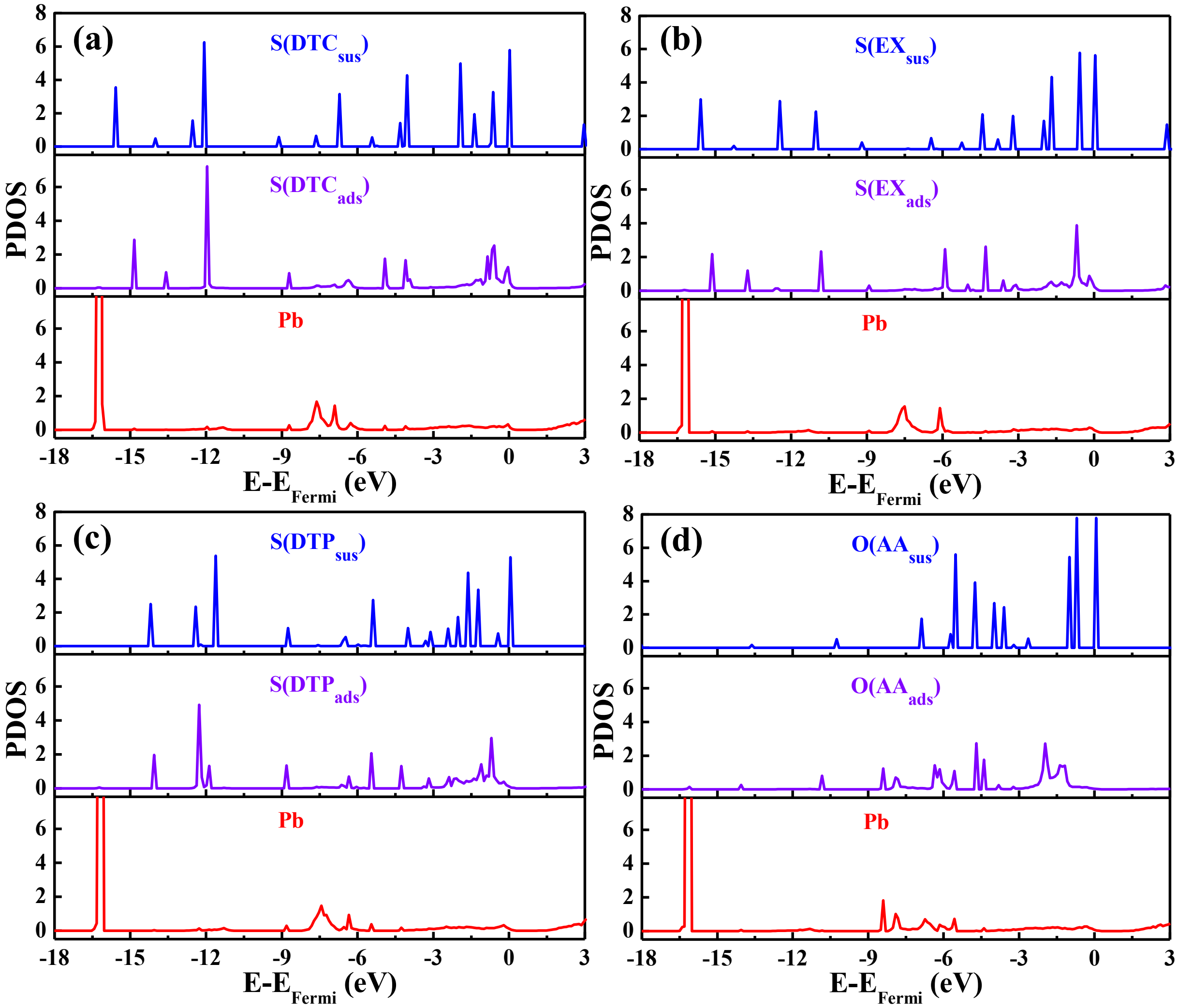

**Figure 4.2** PDOS of the bound Pb and S ions from (a) DTC/PbS(100), (b) EX/PbS(100), (c) DTP/PbS(100) and (d) AA/PbS(100).

To better understand the reasons credited for the distinct adsorption energies of the ligands on PbS(100), we calculated the PDOS of the ions directly participated in the bonding event, which has been proven helpful in revealing the underlying bonding mechanism.[56] The plots presented in Figure 4.2 include PDOS of the terminal ions ($S_{sus}$ or $O_{sus}$) from the ligands in the reference system and those from the adsorbed ligand on PbS(100) ($S_{ads}$ or $O_{ads}$) as well as the active Pb ions on the underlying surface. It is shown in Figure 4.2 (a)-(d) that the adsorption of ligand accompanies with evident electron structure changes around the Fermi level. Apparently, when coupled with the electronic states of the active Pb ions on PbS(100), the narrow ligand states become highly broadened. The states coupling is further verified by the appearance of the weak Pb states in those of the ligand. Likewise, the ligand states can also be seen within the PDOS of the Pb ions right below the Fermi energy. In comparison, the ligand states located below −3 eV only experience negligible changes owing to the inert nature of these low-lying energy states. The limited hybridization between the ligand and Pb ions suggests a weak covalent character of the ligand−PbS(100) bond. Moreover, it is observed that the ligand states around Fermi level shifted negatively upon the adsorption of ligands. Since states below the Fermi level are occupied by electrons, this means that the ligands obtained electrons from the underlying surface and hence indicates some ionic character of the ligand−PbS(100) chemical bond.

We also note that the overall PDOS involving the binding ions is very similar to those of the bare surface and the bulk in Figure 4.1(b). Meanwhile, the adsorption configuration of the ligands on PbS(100) restores the missing S−Pb bond on the surface.[7,31] Altogether, these suggest that the geometric and electronic features of the bulk lead sulfide can be used to predict the ligand−PbS(100) binding mechanism to a large extent.

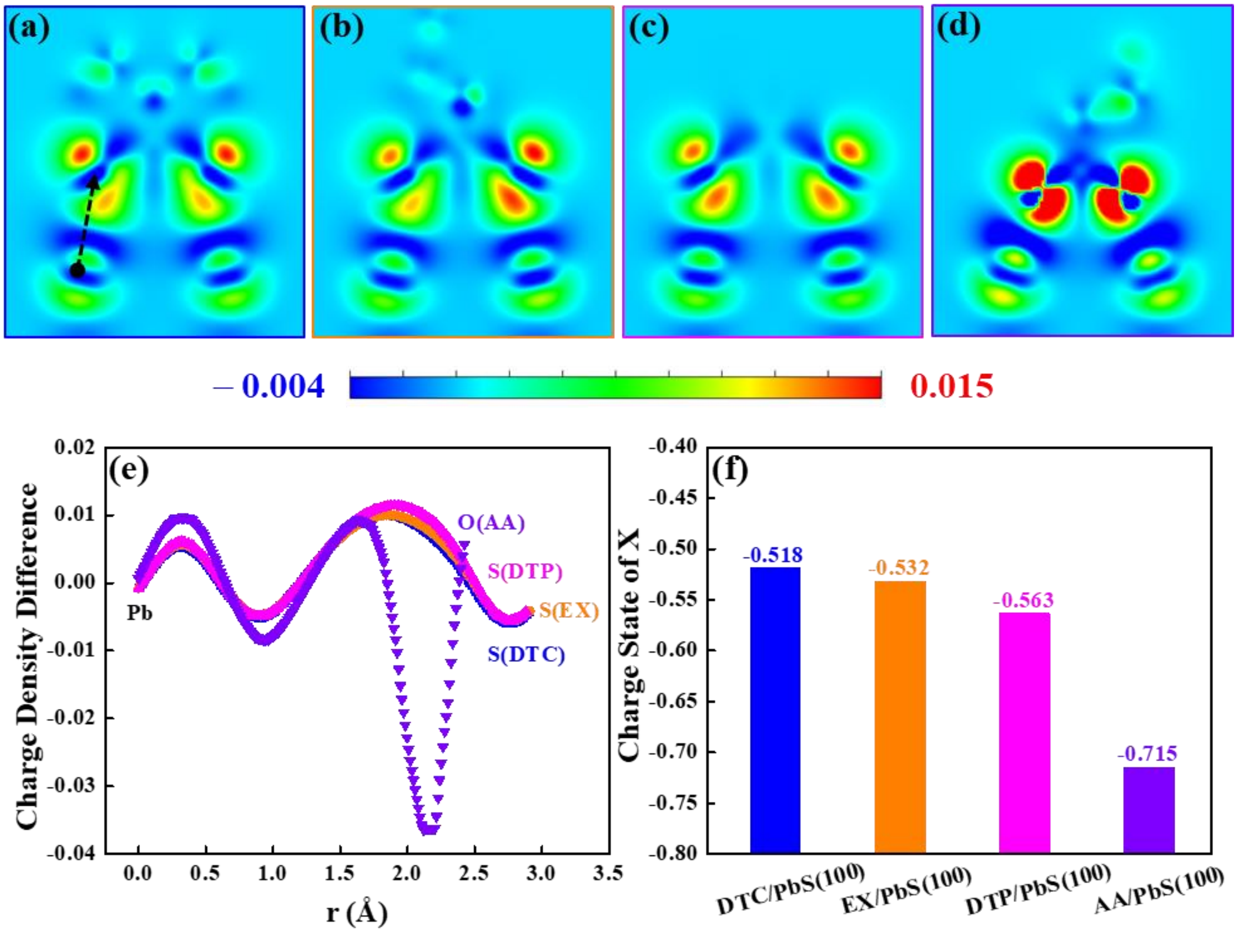

**Figure 4.3** Slices of charge density difference maps for (a) DTC/PbS(100), (b) EX/PbS(100), (c) DTP/PbS(100) and (d) AA/PbS(100), (e) line profiles along Pb−S or Pb−O, (f) charge state of the adsorbed ligands.

We know that the interaction between atoms can lead to the redistribution of electron density around the atomic nuclei and regions in between them (i.e., the bonding regions). These occurrences correspond to the two limits of the ionic bond and the covalent bond, respectively.[57] As such, the charge rearrangement due to the bonding interaction reveals more details on the ligand–PbS(100) bond character. The charge density difference contours (Δρ) containing the bonding ions are presented in Figure 4.3 (a)-(d). The negative and positive values mean the electron depletion and electron accumulation, respectively. For a more direct comparison, the line profiles starting from Pb to the bound ion of the ligands, as marked by the dashed black arrow line, are plotted in Figure 4.3(e).

From the charge difference maps, we can see that the adsorption of ligand leads to pronounced charge redistribution for all cases. The charge close to the bonding region is largely depleted. In comparison, the electrons accumulate intensively around the binding ions from the adsorbed ligand, and the O from AA exhibits the largest degree of electron accumulation. This phenomenon deviates from the ideal covalent situation where the electrons accumulate within the bonding region and locate at the middle point along the bond. Besides, it is worth noting that the electrons obtained by the ligands polarizes toward the underlying Pb ions, signaling considerable electrostatic contribution to the resulting interaction energy. These facts further manifest the dominant ionic nature of the ligand–PbS(100) interaction and support the observed minor bond covalency from the above PDOS analysis.

The adsorption induced electron transfer was further quantified using the Bader scheme on the basis of charge density.[58] This scheme divides the atoms with the so-called zero-flux surface where the charge density is a minimum perpendicular to the surface. The charge of specific atoms can then be obtained by integration of the electron density enclosed within the Bader regions. The calculated charge states of the adsorbed ligands are plotted in Figure 4.3(f). As can be seen, the charge states of the adsorbed ligands amount to −0.518, −0.532, −0.563 and −0.715 for DTC/PbS(100), EX/PbS(100), DTP/PbS(100) and AA/PbS(100), respectively, depending on the attracting abilities of the interacting ions toward the valence electrons. Not surprisingly, the O ion from AA exhibits the largest partial charge, thereby giving rise to the strongest ion-induced dipole interaction with the underlying lead ions among the four cases.

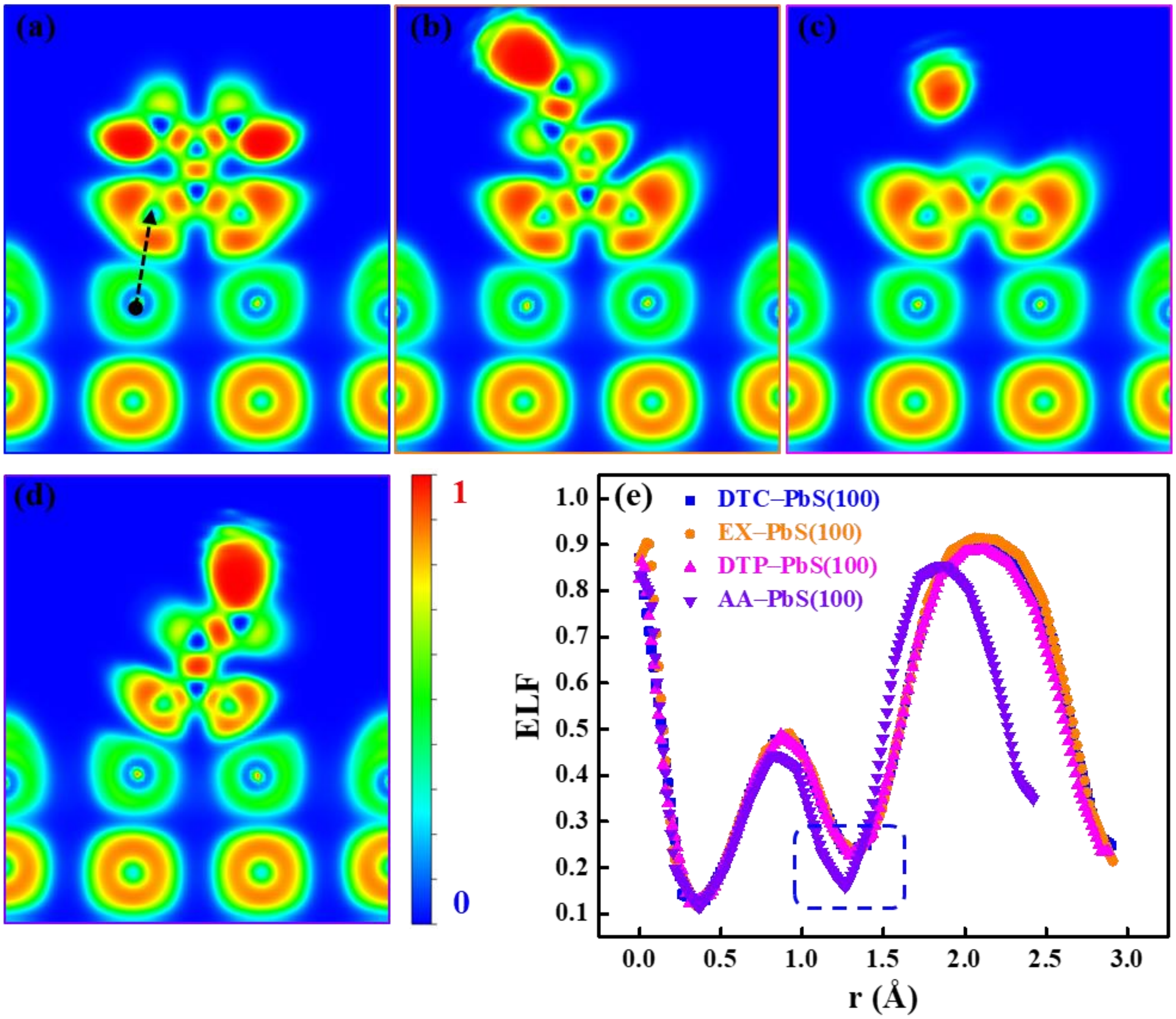

**Figure 4.4** 2-D displays of ELF for (a) DTC/PbS(100), (b) EX/PbS(100), (c) DTP/PbS(100) and (d) AA/PbS(100), (e) line profiles along Pb−S or Pb−O and the labeled area denotes the bonding region.

By far, we have demonstrated the dominant ionic character of the ligand–PbS(100) bonds. However, the ligands, particularly the thiol-based ligands, have been conventionally deemed to bind with metal sulfides covalently because of the small electronegativity difference between the atomic sulfur and metallic elements.[59] To further check the ligand–PbS(100) bond covalency, we resorted to the electron localization function (ELF) which reflects the probability of finding electron pairs. The value of ELF scales from 0 to 1, where 1 and 0.5 correspond to fully localized and fully delocalized electrons, respectively, whereas 0 indicates an extremely low charge density. The ELF along the bond, especially the minimum value within the bond region, has been suggested as persuasive proof of the relative bond covalency.[60] The ELF of the four cases are provided in Figure 4.4 (a)-(d), together with the corresponding line profiles in Figure 4.4 (e). Firstly, no obvious localization domains are observed within the ligand−PbS(100) bond regions for all the cases. The line profile also indicates that the ELF values of the bonding region are extremely low. The ELF, thus, provides extra evidence on the weak covalent nature of the ligand−PbS(100) interaction. Collectively, it is concluded that the ligand−PbS(100) bond is essentially ionic with minor covalency.

## 4.4 Discussion

As mentioned earlier, the computational binding energy has been widely used as the descriptor to assess the functionalities of a ligand. However, our results showed that the binding energy trend failed to match with the relative hydrophobic functionalities of the ligands toward PbS in the context of froth flotation. The solubility product ($pK_{sp}$) of the ligand−lead compound is the recognized experimental metric in terms of the hydrophobic functionality of the ligand toward PbS. We compared the ligand−PbS(100) binding strength with the corresponding $pK_{sp}$ in Figure 4.5 (a). It shows clearly that the binding strength trend (DTC < EX < DTP < AA) is completely opposite to that of $pK_{sp}$. This inconsistency is also encountered in previous studies but remains unclear.[31]

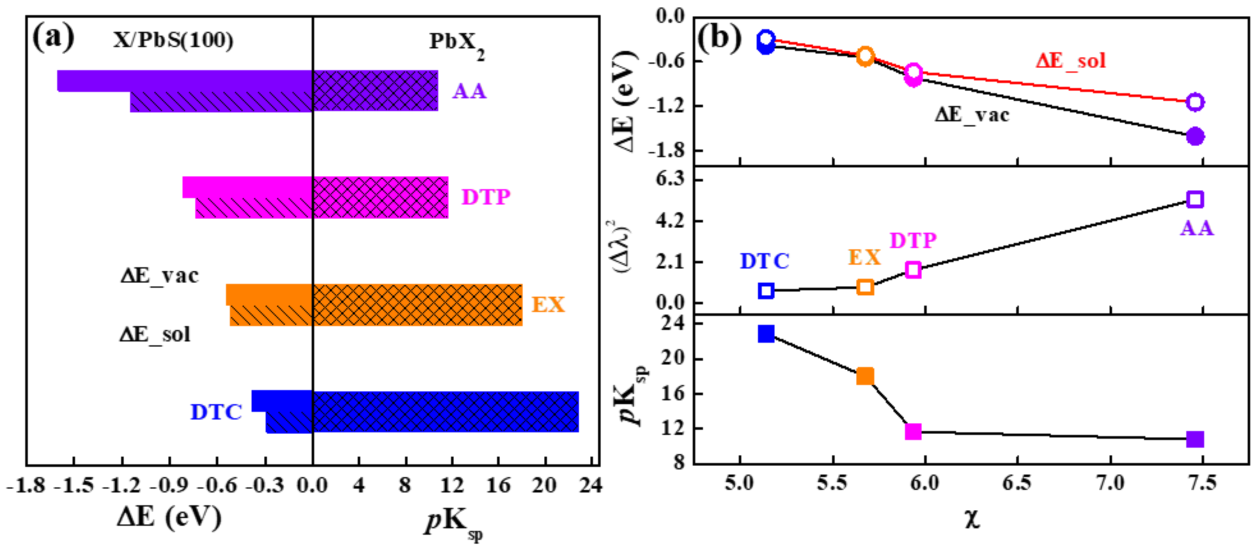

**Figure 4.5** (a) The binding energy (ΔE) of X−PbS(100) and the solubility product ($pK_{sp}$) of the corresponding $PbX_2$ compound (ten carbons were included for $PbAA_2$), (b) ΔE, $(\Delta\lambda)^2$ and $pK_{sp}$ plotted against the ligand electronegativity (χ).

According to our findings on the ligand−PbS(100) bond character, the ligands bind with PbS(100) predominantly ionically with very limited covalency. The ionic contribution thus in a first approximation plays a decisive role in the resulting adsorption energy. In this case, such binding strength trend (DTC < EX < DTP < AA) stems from the increasing ionic fraction of the ligand−PbS(100) interaction. Furthermore, it is well known that the S-tailed ligands with only 2-4 carbon atoms in the hydrocarbon tail can induce appreciable flotation performance of lead sulfide. Given the short hydrocarbon chain and similar ligand skeleton structure, the ligand−PbS(100) bond character has a significant impact on the resulting surface hydrophobicity. In addition, the widespread electronegativity model in the context of minerals flotation claims that the relative empirical electronegativity difference [$(\Delta\lambda)^2$] between the ligand and active metallic atom on mineral surface closely relates to the collecting ability of the ligand toward minerals.[59] The lower the value of $(\Delta\lambda)^2$ is, the larger the fraction of the resulting bond covalency and eventually a more hydrophobic surface. Although we found that the ligand−PbS(100) bond is essentially ionic, the relative covalency trend correlates with the spirit of the electronegativity theory. Under this connection, the thiol ligands (DTC, EX and DTP) and PbS(100) form less ionic bond that yields higher degree of surface hydrophobicity and consequently, desirable flotation performance of galena mineral particles can be achieved. On the other hand, the bond formed between the O-tailed ligand (AA) and PbS(100) possesses a considerably larger fraction of ionicity. Accordingly, the ligand with much longer hydrocarbon chain is needed to achieve comparable flotation performance of galena as that of the thiol collectors. Though it is difficult to explicitly classify and quantify the ionic and the covalent contributions to the resulting interaction energy, this qualitative analysis on the basis of the bond character points to a comprehensive elucidation of the discordance between the binding energy and the hydrophobic functionality of the ligand.

In light of the above clarification, we know that the ligand−PbS(100) bond character, rather than the commonly used binding energy, can more accurately predict the relative hydrophobic functionality of the ligand with a specific ligand tail toward galena. The ligand electronegativity ($\chi$) that can capture the relative ligand−PbS(100) bond iconicity hence holds the potential as a descriptor for rationally tailoring the hydrophobic functionality of the ligand. As shown in Figure 4.5(b), the $\chi$ extraordinarily relates to the corresponding adsorption energy ($\Delta E$), the empirical electronegativity difference $[(\Delta\lambda)^2]$ as well as the solubility product of $PbX_2$ ($pK_{sp}$), further corroborating its robustness as a descriptor. Therefore, this study not only helps to better understand the ligand−PbS(100) interaction mechanism, but also provides new insights into the computational design of improved ligands.

Calculations of the ligand electronegativity, DFT results on the bond character of Zn−C in dimethylzinc, supporting figures and other related information can be found in Appendix B.

## 4.5 Conclusions

Efficient modification of surface properties of metal sulfides through the adsorption of specially designed ligands plays a pivotal role in numerous engineering applications. We studied the adsorption of typical S/O-tailed ligands on the lead sulfide PbS(100) surface using density functional theory (DFT) calculations. Extensive analyses have been performed to comprehend the resulting ligand−PbS(100) bond character by the joint projected density of states (PDOS), charge density difference, Bader charge and electron localization function (ELF) calculations. The ligand−PbS(100) bond was revealed to be predominantly ionic with minor covalency, in direct contrast to the classical view of covalent bonding. Moreover, instead of the generally used binding energy, the ligand electronegativity ($\chi$) was established as a potential descriptor to accurately predict the relative ligand hydrophobic functionality toward PbS with a certain normal hydrocarbon tail. The effectiveness of this descriptor was strongly supported by its extraordinary correlations with both the recognized solubility product constant ($pK_{sp}$) of the corresponding ligand−Pb compound and the ligand/atomic lead electronegativity difference [$(\Delta\lambda)^2$]. Therefore, this study further advances our understanding on the interaction mechanism between the ligands and PbS(100). The insight on the ligand−metal sulfide bond character, together with its demonstrated applicability in the hydrophobization case of lead sulfide, offers new perspective on the descriptor-based design of ligand with tailored functionalities as well.

## 4.6 References

(1) Chia, X.; Eng, A. Y. S.; Ambrosi, A.; Tan, S. M.; Pumera, M. Electrochemistry of Nanostructured Layered Transition-Metal Dichalcogenides. *Chem. Rev.* **2015**, *115* (21), 11941–11966.

(2) Asadi, M.; Kim, K.; Liu, C.; Addepalli, A. V.; Abbasi, P.; Yasaei, P.; Phillips, P.; Behranginia, A.; Cerrato, J. M.; Haasch, R.; et al. Nanostructured Transition Metal Dichalcogenide Electrocatalysts for $CO_2$ Reduction in Ionic Liquid. *Science* **2016**, *353* (6298), 467–470.

(3) Tao, H.; Liu, S.; Luo, J. L.; Choi, P.; Liu, Q.; Xu, Z. Descriptor of Catalytic Activity of Metal Sulfides for Oxygen Reduction Reaction: A Potential Indicator for Mineral Flotation. *J. Mater. Chem. A* **2018**, *6* (20), 9650–9656.

(4) Gilbert, B.; Huang, F.; Lin, Z.; Goodell, C.; Zhang, H.; Banfield, J. F. Surface Chemistry Controls Crystallinity of ZnS Nanoparticles. *Nano Lett.* **2006**, *6* (4), 605–610.

(5) Tang, J.; Kemp, K. W.; Hoogland, S.; Jeong, K. S.; Liu, H.; Levina, L.; Furukawa, M.; Wang, X.; Debnath, R.; Cha, D.; et al. Colloidal-Quantum-Dot Photovoltaics Using Atomic-Ligand Passivation. *Nat. Mater.* **2011**, *10* (10), 765–771.

(6) Zherebetskyy, D.; Scheele, M.; Zhang, Y.; Bronstein, N.; Thompson, C.; Britt, D.; Salmeron, M.; Alivisatos, P.; Wang, L.-W. Hydroxylation of the Surface of PbS Nanocrystals Passivated with Oleic Acid. *Science* **2014**, *344* (6190), 1380–1384.

(7) Bealing, C. R.; Baumgardner, W. J.; Choi, J. J.; Hanrath, T.; Hennig, R. G. Predicting Nanocrystal Shape through Consideration of Surface-Ligand Interactions. *ACS Nano*

**2012**, *6* (3), 2118–2127.

(8) Rotenberg, B.; Patel, A. J.; Chandler, D. Molecular Explanation for Why Talc Surfaces Can Be Both Hydrophilic and Hydrophobic. *J. Am. Chem. Soc.* **2011**, *133* (50), 20521–20527.

(9) Xie, L.; Wang, J.; Shi, C.; Cui, X.; Huang, J.; Zhang, H.; Liu, Q.; Liu, Q.; Zeng, H. Mapping the Nanoscale Heterogeneity of Surface Hydrophobicity on the Sphalerite Mineral. *J. Phys. Chem. C* **2017**, *121* (10), 5620–5628.

(10) Chu, X. S.; Yousaf, A.; Li, D. O.; Tang, A. A.; Debnath, A.; Ma, D.; Green, A. A.; Santos, E. J. G.; Wang, Q. H. Direct Covalent Chemical Functionalization of Unmodified Two-Dimensional Molybdenum Disulfide. *Chem. Mater.* **2018**, *30* (6), 2112–2128.

(11) Rodríguez-Hermida, S.; Tsang, M. Y.; Vignatti, C.; Stylianou, K. C.; Guillerm, V.; Pérez-Carvajal, J.; Teixidor, F.; Viñas, C.; Choquesillo-Lazarte, D.; Verdugo-Escamilla, C. Switchable Surface Hydrophobicity–Hydrophilicity of a Metal–Organic Framework. *Angew. Chemie Int. Ed.* **2016**, *55* (52), 16049–16053.

(12) Comas, H.; Laporte, V.; Borcard, F.; Miéville, P.; Krauss Juillerat, F.; Caporini, M. A.; Gonzenbach, U. T.; Juillerat-Jeanneret, L.; Gerber-Lemaire, S. Surface Functionalization of Alumina Ceramic Foams with Organic Ligands. *ACS Appl. Mater. Interfaces* **2012**, *4* (2), 573–576.

(13) Xie, L.; Wang, J.; Shi, C.; Huang, J.; Zhang, H.; Liu, Q.; Liu, Q.; Zeng, H. Probing Surface Interactions of Electrochemically Active Galena Mineral Surface Using Atomic Force Microscopy. *J. Phys. Chem. C* **2016**, *120* (39), 22433–22442.

(14) Mu, Y.; Peng, Y.; Lauten, R. A. Electrochemistry Aspects of Pyrite in the Presence of Potassium Amyl Xanthate and a Lignosulfonate-Based Biopolymer Depressant. *Electrochim. Acta* **2015**, *174* (1), 133–142.

(15) Midya, L.; Patra, A. S.; Banerjee, C.; Panda, A. B.; Pal, S. Novel Nanocomposite Derived from ZnO/CdS QDs Embedded Crosslinked Chitosan: An Efficient Photocatalyst and Effective Antibacterial Agent. *J. Hazard. Mater.* **2019**, *369* (January), 398–407.

(16) Ng, W. S.; Forbes, E.; Franks, G. V.; Connal, L. A. Xanthate-Functional Temperature-Responsive Polymers: Effect on Lower Critical Solution Temperature Behavior and Affinity toward Sulfide Surfaces. *Langmuir* **2016**, *32* (30), 7443–7451.

(17) Moreels, I.; Fritzinger, B.; Martins, J. C.; Hens, Z. Surface Chemistry of Colloidal PbSe Nanocrystals. *J. Am. Chem. Soc.* **2008**, *130* (45), 15081–15086.

(18) Peterson, M. D.; Jensen, S. C.; Weinberg, D. J.; Weiss, E. A. Mechanisms for Adsorption of Methyl Viologen on Cds Quantum Dots. *ACS Nano* **2014**, *8* (3), 2826–2837.

(19) Larsson, M. L.; Holmgren, A.; Forsling, W. Xanthate Adsorbed on ZnS Studied by Polarized FTIR-ATR Spectroscopy. *Langmuir* **2000**, *16* (21), 8129–8133.

(20) Nørskov, J. K.; Bligaard, T.; Rossmeisl, J.; Christensen, C. H. Towards the Computational Design of Solid Catalysts. *Nat. Chem.* **2009**, *1* (1), 37–46.

(21) Maganas, D.; Neese, F.; Bistoni, G.; Ye, S.; Atanasov, M. Chemistry and Quantum Mechanics in 2019: Give Us Insight and Numbers. *J. Am. Chem. Soc.* **2019**, *141*(7), 2814–2824.

(22) Nørskov, J. K.; Bligaard, T.; Rossmeisl, J.; Christensen, C. H. Towards the Computational

Design of Solid Catalysts. *Nat. Chem.* **2009**, *1* (1), 37–46.

(23) Nørskov, J. K.; Abild-Pedersen, F.; Studt, F.; Bligaard, T. Density Functional Theory in Surface Chemistry and Catalysis. *Proc. Natl. Acad. Sci.* **2011**, *108* (3), 937–943.

(24) Schumann, J.; Medford, A. J.; Yoo, J. S.; Zhao, Z.; Bothra, P. Selectivity of Synthesis Gas Conversion to $C_{2+}$ Oxygenates on Fcc(111) Transition-Metal Surfaces. *ACS Catal.* **2018**, *8* (4), 3447–3453.

(25) Medford, A. J.; Wellendorff, J.; Vojvodic, A.; Studt, F.; Abild-pedersen, F.; Jacobsen, K. W.; Bligaard, T. Assessing the Reliability of Calculated Catalytic Ammonia Synthesis Rates. *Science* **2014**, *345* (6193), 197–200.

(26) Kulkarni, A.; Siahrostami, S.; Patel, A.; Nørskov, J. K. Understanding Catalytic Activity Trends in the Oxygen Reduction Reaction. *Chem. Rev.* **2018**, *118* (5), 2302–2312.

(27) Hammer, B.; Nørskov, J. K. Electronic Factors Determining the Reactivity of Metal Surfaces. *Surf. Sci.* **1995**, *343* (3), 211–220.

(28) He, Y.; Fishman, Z. S.; Yang, K. R.; Ortiz, B.; Liu, C.; Goldsamt, J.; Batista, V. S.; Pfefferle, L. D. Hydrophobic CuO Nanosheets Functionalized with Organic Adsorbates. *J. Am. Chem. Soc.* **2018**, *140* (5), 1824–1833.

(29) Yin, Z.; Hu, Y.; Sun, W.; Zhang, C.; He, J.; Xu, Z.; Zou, J.; Guan, C.; Zhang, C.; Guan, Q.; et al. Adsorption Mechanism of 4-Amino-5-Mercapto-1,2,4-Triazole as Flotation Reagent on Chalcopyrite. *Langmuir* **2018**, *34* (13), 4071–4083.

(30) Waterson, C. N.; Tasker, P. A.; Farinato, R.; Nagaraj, D. R.; Shackleton, N.; Morrison, C. A. A Computational and Experimental Study on the Binding of Dithio Ligands to

Sperrylite, Pentlandite, and Platinum. *J. Phys. Chem. C* **2016**, *120* (39), 22476–22488.

(31) Long, X.; Chen, Y.; Chen, J.; Xu, Z.; Liu, Q.; Du, Z. The Effect of Water Molecules on the Thiol Collector Interaction on the Galena (PbS) and Sphalerite (ZnS) Surfaces: A DFT Study. *Appl. Surf. Sci.* **2016**, *389*, 103–111.

(32) Kresse, G.; Hafner, J. Ab Initio Molecular Dynamics for Liquid Metals. *Phys. Rev. B* **1993**, *47* (1), 558–561.

(33) Kresse, G.; Hafner, J. Ab Initio Molecular-Dynamics Simulation of the Liquid-Metal–amorphous-Semiconductor Transition in Germanium. *Phys. Rev. B* **1994**, *49* (20), 14251–14269.

(34) Kresse, G.; Furthmüller, J. Efficiency of Ab-Initio Total Energy Calculations for Metals and Semiconductors Using a Plane-Wave Basis Set. *Comput. Mater. Sci.* **1996**, *6* (1), 15–50.

(35) Kresse, G.; Furthmüller, J. Efficient Iterative Schemes for Ab Initio Total-Energy Calculations Using a Plane-Wave Basis Set. *Phys. Rev. B* **1996**, *54* (16), 11169–11186.

(36) Blöchl, P. E. Projector Augmented-Wave Method. *Phys. Rev. B* **1994**, *50* (24), 17953–17979.

(37) Kresse, G. From Ultrasoft Pseudopotentials to the Projector Augmented-Wave Method. *Phys. Rev. B* **1999**, *59* (3), 1758–1775.

(38) Hammer, B.; Hansen, L. B.; Nørskov, J. K. Improved Adsorption Energetics within Density-Functional Theory Using Revised Perdew-Burke-Ernzerhof Functionals. *Phys. Rev. B* **1999**, *59* (11), 7413–7421.

(39) Monkhorst, H. J.; Pack, J. D. Special Points for Brillouin-Zone Integrations. *Phys. Rev. B* **1976**, *13* (12), 5188–5192.

(40) Mathew, K.; Sundararaman, R.; Letchworth-weaver, K.; Arias, T. A.; Hennig, R. G. Implicit Solvation Model for Density-Functional Study of Nanocrystal Surfaces and Reaction Pathways. *J. Chem. Phys.* **2014**, *140* (8), 084106.

(41) Fishman, M.; Zhuang, H. L.; Mathew, K.; Dirschka, W.; Hennig, R. G. Accuracy of Exchange-Correlation Functionals and Effect of Solvation on the Surface Energy of Copper. *Phys. Rev. B* **2013**, *87* (24), 245402.

(42) Kitchaev, D. A.; Ceder, G. Evaluating Structure Selection in the Hydrothermal Growth of $FeS_2$ Pyrite and Marcasite. *Nat. Commun.* **2016**, *7*, 13799.

(43) Garza, A.; Bell, A. T.; Head-Gordon, M. Is Subsurface Oxygen Necessary for the Electrochemical Reduction of $CO_2$ on Copper? *J. Phys. Chem. Lett.* **2018**, *9* (3), 601–606.

(44) Chowdhry, M. Theoretical Study on Reactivity of Different Sulfide Collectors and Their Binding Affinity Toward Cu (II), Zn (II) and Pb (II) Ions, Ph.D dissertation, University of Alberta, Edmonton, AB, 2015.

(45) Gaussian 16, Revision B.01, Frisch, M. J.; Trucks, G. W.; Schlegel, H. B.; Scuseria, G. E.; Robb, M. A.; Cheeseman, J. R.; Scalmani, G.; Barone, V.; Petersson, G. A.; Nakatsuji, H.; Li, X.; Caricato, M.; Marenich, A. V.; Bloino, J.; Janesko, B. G.; Gomperts, R.; Mennucci, B.; Hratchian, H. P.; Ortiz, J. V.; Izmaylov, A. F.; Sonnenberg, J. L.; Williams-Young, D.; Ding, F.; Lipparini, F.; Egidi, F.; Goings, J.; Peng, B.; Petrone, A.; Henderson, T.; Ranasinghe, D.; Zakrzewski, V. G.; Gao, J.; Rega, N.; Zheng, G.; Liang, W.; Hada,

M.; Ehara, M.; Toyota, K.; Fukuda, R.; Hasegawa, J.; Ishida, M.; Nakajima, T.; Honda, Y.; Kitao, O.; Nakai, H.; Vreven, T.; Throssell, K.; Montgomery, J. A., Jr.; Peralta, J. E.; Ogliaro, F.; Bearpark, M. J.; Heyd, J. J.; Brothers, E. N.; Kudin, K. N.; Staroverov, V. N.; Keith, T. A.; Kobayashi, R.; Normand, J.; Raghavachari, K.; Rendell, A. P.; Burant, J. C.; Iyengar, S. S.; Tomasi, J.; Cossi, M.; Millam, J. M.; Klene, M.; Adamo, C.; Cammi, R.; Ochterski, J. W.; Martin, R. L.; Morokuma, K.; Farkas, O.; Foresman, J. B.; Fox, D. J. Gaussian, Inc., Wallingford CT, 2016.

(46) Lee, Chengteh, Weitao Yang, and R. G. P. Development of the Colle-Salvetti Correlation-Energy Formula into a Functional of the Electron Density. *Phys. Rev. B* **1988**, *37* (2), 785–789.

(47) Rienstra-Kiracofe, J. C.; Tschumper, G. S.; Schaefer, H. F.; Nandi, S.; Ellison, G. B. Atomic and Molecular Electron Affinities: Photoelectron Experiments and Theoretical Computations. *Chem. Rev.* **2002**, *102* (1), 231–282.

(48) Thomas Heine, Jan-Ole Joswig, A. G. Computational Chemistry Workbook. *ChemPhysChem* **2011**, *12* (11), 2184.

(49) Downs, R. T.; Hall-Wallace, M. The American Mineralogist Crystal Structure Database. *Am. Mineral.* **2003**, *88* (1), 247–250.

(50) Becker, U.; Rosso, K. M. Step Edges on Galena(100): Probing the Basis for Defect Driven Surface Reactivity at the Atomic Scale. *Am. Mineral.* **2001**, *86* (7–8), 862–870.

(51) Vaughan, D. J. Chemical Bonding in Sulfide Minerals. *Rev. Mineral. Geochemistry* **2006**, *61* (1), 231–264.

(52) Mathew, K.; Sundararaman, R.; Letchworth-Weaver, K.; Arias, T. A.; Hennig, R. G. Implicit Solvation Model for Density-Functional Study of Nanocrystal Surfaces and Reaction Pathways. *J. Chem. Phys.* **2014**, *140* (8), 1–9.

(53) Rosso, K. M. Structure and Reactivity of Semiconducting Mineral Surfaces: Convergence of Molecular Modeling and Experiment. *Rev. Miner. Geochemistry* **2001**, *42* (1), 199–271.

(54) Grandke, T.; Ley, L.; Cardona, M. Angle-Resolved Uv Photoemission and Electronic Band Structures of the Lead Chalcogenides. *Phys. Rev. B* **1978**, *18* (8), 3847–3871.

(55) Li, R.; Bian, K.; Hanrath, T.; Bassett, W. A.; Wang, Z. Decoding the Superlattice and Interface Structure of Truncate PbS Nanocrystal-Assembled Supercrystal and Associated Interaction Forces. *J. Am. Chem. Soc.* **2014**, *136* (34), 12047–12055.

(56) Gudmundsdóttir, S.; Tang, W.; Henkelman, G.; Jónsson, H.; Skúlason, E. Local Density of States Analysis Using Bader Decomposition for $N_2$ and $CO_2$ Adsorbed on Pt(110)-(1 × 2) Electrodes. *J. Chem. Phys.* **2012**, *137* (16), 164705.

(57) Evarestov, R. A. *Quantum Chemistry of Solids: The LCAO First Principles Treatment of Crystals.* Springer Science & Business Media*,* 2007.

(58) Yu, M.; Trinkle, D. R. Accurate and Efficient Algorithm for Bader Charge Integration. *J. Chem. Phys.* **2011**, *134* (6), 1–19.

(59) Wang, D. *Flotation Reagents: Applied Surface Chemistry on Minerals Flotation and Energy Resources Beneficiation*. Springer Singapore, 2016.

(60) Silvi, B.; Savin, A. Classification of Chemical Bonds Based on Topological Analysis of

Electron Localization Functions. *Nature* **1994**, *371* (6499), 683-686.

# Chapter 5 Chemical Functionalization of ZnS: A Perspective from the Ligand–ZnS Bond Character

**Abstract:** Chemical functionalization of metal sulfides plays a critical role in many fields such as materials science and froth flotation. The commonly used thiol-bearing functionalization ligands are generally considered to bind with metal sulfides covalently, and the computed binding energy is widely used to evaluate the functionality of the ligands toward metal sulfides. Herein, we studied the surface chemistry of the model ZnS and its binding with typical S- and O-terminated ligands using density functional theory calculations with an emphasis on the resulting bond character. Surprisingly, it was found that the ligand–ZnS(110) bond is essentially ionic with limited covalency. This very fundamental finding was further extended to the hydrophobization of ZnS in the context of froth flotation and rationalized the previously unresolved phenomenon that the higher the ligand–ZnS(110) binding strength, the lower the ligand hydrophobic functionality toward ZnS. Meanwhile, instead of the binding energy, the electronegativity of the ligand was identified as potential computational descriptor which can accurately predict the relative ligand hydrophobic functionality toward ZnS. This work, therefore, further advanced our understanding of the intrinsic ligand–metal sulfide binding mechanism and highlighted the importance of computational parameters, beyond the binding energy, in guiding the first-principles design of ligands with enhanced functionalities or optimizing relevant industrial processes.

## 5.1 Introduction

Metal sulfides are fascinating materials which have been found useful in many engineering applications.[1–3] In catalysis, the metal-based (e.g., Ru-, Mo-, Ag-) chalcogenides are emerging as earth-abundant and cost-effective catalysts owing to the superior intrinsic catalytic activities toward oxygen reduction reaction (ORR),[4,5] hydrogen evolution reaction (HER)[6,7] and carbon dioxide reduction reaction ($CO_2$RR).[8,9] Moreover, certain semiconducting metal sulfide nanocrystals (e.g., CrS and ZnS) have been intensively studied as critical components in many electronic devices due to their distinctive electronic and optical properties.[10] In addition, the natural metal sulfides constitute the principal raw resources for a broad range of base metals and are mainly separated from the gangue or clay minerals in froth flotation on the basis of the surface hydrophobicity differences.[11,12] Importantly, studies have shown that surface functionalization of the materials with specially designed ligands can profoundly modify the surface physicochemical properties and thus hold the possibilities for more desired catalytic activity of the materials, better control of the functional nanocrystal synthesis or further optimization of relevant industrial practices.[3,13–15] However, rational design of such functionalization ligands calls for deep insights into the ligand–metal sulfide interaction and basic knowledge of the key parameters determining the macroscopic functionality of interest.

Over the past several decades, there has been significant drive in unravelling the ligand–metal sulfide binding mechanism to accelerate the design of ligands with enhanced functionalities toward metal sulfides, such as the hydrophobization of sphalerite in the context of mineral flotation. The spectroscopic tests using Raman spectroscopy,[16] Fourier transform infrared spectroscopy (FTIR)[17,18] and X-ray photoelectron spectroscopy (XPS)[3,12] have provided solid evidence on the presence of functionalization ligands on the metal sulfides while offering limited information on the binding process on an atomic scale. In response, the electronic structure calculations on the basis of the density functional theory (DFT) were widely performed. This method has been proven particularly helpful in identifying the intrinsic attributes of materials responsible for the activity variations from one material to another.[19,20] The computed binding energy has been widely used as the parameter to evaluate the functionality of surfactants.[21–23] For example, previous DFT calculations gave the binding energies of typical thiol surfactants with metal sulfides to compare the ligands' hydrophobic functionalities and hence the collecting abilities of the ligands toward metal sulfides in flotation.[24] Nevertheless, the calculated relative binding strengths followed a reverse order to the solubility product of the corresponding ligand–metal compound which is the recognized experimental metric for evaluating the ligand collecting abilities toward metal sulfides. Up to now, neither the underlying ligand–metal sulfide interaction mechanism nor the resultant bond character is well understood. Meanwhile, the descriptors enabling the rational design of ligands with enhanced hydrophobic functionalities remain unavailable. It is, therefore, highly desirable to explore computational parameters, other than the binding energy, to guide the directional design of functionalization ligands.

To this end, we studied the surface chemistry of the model ZnS using DFT calculations and subsequently explored the adsorption of commonly used functionalization ligands containing thiol [dimethyl dithiocarbamate (DTC, $C_2H_6NCS_2$), ethyl xanthate (EX, $C_2H_5OCS_2$) and dimethyl dithiophosphate (DTP, $C_2H_6O_2PS_2$)] and carboxyl [acetic acid (AA, $C_2H_5CO_2$)] groups on ZnS(110). The combined projected density of states (PDOS), charge density difference, Bader charge and electron localization function (ELF) calculations were carried out to elucidate the ligand−ZnS(110) binding mechanism as well as the resulting bond character. Based on the theoretical findings, we turned to the special case of ZnS hydrophobization to link the hydrophobization performance with the electronic properties of the functionalization ligand. Given the importance of functionalization in tailoring the catalytic activity of catalysts and synthesis of the functional nanocrystals, the methodology and results are expected to be applicable in similar studies and to invoke explorations of guiding computational descriptors other than the binding energy in terms of the ligand design.

## 5.2 Computational Details

The first-principles calculations were performed using the Vienna *ab initio* Simulation Package (VASP).[25–28] The projector-augmented wave method[29,30] was employed and the electron wavefunctions were presented by the planewave basis set at a cut-off energy 450 eV. The Perdew-Burke-Ernzerhof generalized gradient approximation functional[31] was selected to describe the exchange and correlation interactions. The occupancy of the one-electron states was calculated using an electronic temperature of $k_B$T = 0.05 eV and the resulting energies were extrapolated to 0 K. The $k$-point grids of 7 × 7 × 7 under the Monkhorst-Pack scheme[32] was set for the ZnS unit cell, whereas only the Gamma point was adopted for the functionalization ligands. The models were relaxed using the quasi-Newton algorithm as implemented in VASP. The convergence was assumed when the total energy difference between cycles and the residual forces were less than $10^{-4}$ eV and 0.05 eV/Å, respectively. After fully relaxed, the lattice constants of ZnS unit cell are $a = b = c = 5.45$ Å, close to the experimental lattice parameters of $a = b = c = 5.41$ Å.[33]

The ZnS(110) model which has been widely used as the representative surface for sphalerite was then constructed as a 2 × 3 slab with six atomic layers.[24,34] A vacuum layer with thickness of 30 Å was introduced to the slab to minimize the spurious interactions between periodic images.

During optimization, only the top three atomic layers of the slab models were relaxed, while the bottom three layers were constraint at the bulk positions. The computed surface energy of ZnS(110) is 0.6 J/m$^2$ which equals to that in previous calculation, further validating the above computational setups.[35]

The functionalization ligands were constructed containing two carbon atoms in the tail to largely exclude the effect of hydrocarbon chain on the interaction. The adsorption models were built with each of the ligand adsorbing on the 2 × 3 slab model of ZnS(110) for the purpose of this study. The solvation effect was approximately evaluated by means of the continuum implicit solvation model (VASPsol).[36,37] More details on VASPsol can be found in Appendix C. This model has been verified as being capable of reproducing solvation energies of a series of isolated molecules and has been successfully employed for many interfacial adsorption studies.[36–39] Finally, the binding energy of the ligand on ZnS(110) was calculated as,[24,40]

$$\Delta E_{ads} = E_{adsorbate/surface} - E_{adsorbate\_surface} \qquad \text{5-1}$$

where $\Delta E_{ads}$, $E_{adsorbate/surface}$ and $E_{adsorbate\_surface}$ are the adsorption energy, the energy of the ligand–ZnS(110) bound system and the energy of the reference system where the ligand suspends in the middle of the vacuum layer, respectively.

## 5.3 Results and Discussion

Prior to simulating the adsorption of functionalization ligands, the geometric and electronic structures of optimized ZnS(110) were examined to gain information on the surface reactivity. The side and top views of the relaxed ZnS(110) are presented in Figures 5.1 (a) and (b), respectively.

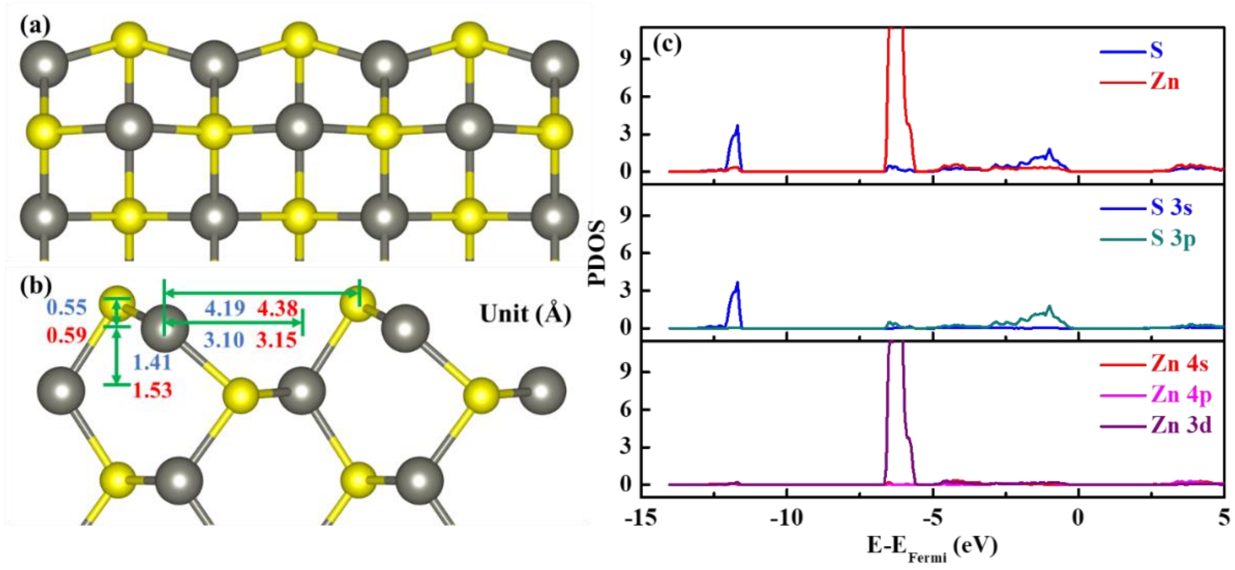

**Figure 5.1** (a) Side view and (b) top view of the optimized ZnS(110), (c) PDOS of the surface Zn and S ions.

Within the top layer, each ion is coordinated by three neighbors, while zinc cation from the inner layers and the bulk crystal is tetrahedrally connected with four neighbouring sulfur anions and vice versa. Upon being relaxed, the ZnS(110), particularly the top layer, underwent noteworthy relaxations and reconstructions and eventually appeared corrugated. It is shown in Figure 5.1(b) that the Zn and S ions on the top layer are downshifted by 0.4 Å and upshifted by 0.153 Å, respectively, with reference to the bulk configurations. Not surprisingly, the surface Zn–S bond length becomes shorter by 0.083 Å in comparison with those in the inner layers, deriving from the less coordinated environment on the surface.[35] Moreover, Figure 5.1(b) illustrates that the calculated geometric parameters (blue) are highly consistent with the corresponding experimental results (red), validating the accuracy and reliability of the present computational methods. The electronic structure of ZnS(110) was analyzed using the projected density of states (PDOS) of the surface Zn and S ions in Figure 5.1(c). Inspection of the PDOS reveals that the top of the valence band is dominated by the S 3p states with minor contribution from Zn 4sp states, ranging from −5 to 0 eV (i.e., the Fermi level). In comparison, the band at around −6 eV is mainly comprised of the Zn 3d states, while the S 3s states are much lower in energy (~11 eV below the Fermi level). The relative location and distribution of the electronic states in the calculated PDOS are in good agreements with the reported spectroscopic experiment results.[42]

With the relaxed ZnS(110), the adsorption of ligands was conducted and the optimized adsorption models of DTC, EX, DTP and AA on ZnS(110) are presented in Scheme 5.1. It is observed that the adsorption configurations experience little differences regardless of the different types of the bonding ligands. Specifically, the terminal ions from the ligands bind with the surface Zn ions in a bridging bidentate mode, in agreement with previous studies.[43–45] We then extracted and compared the calculated geometric parameters with those deduced from the polarized FTIR-ATR spectroscopy in Figure 5.2.[45] As seen, the two series of structural parameters are highly consistent which further supports the reliability of current DFT study.

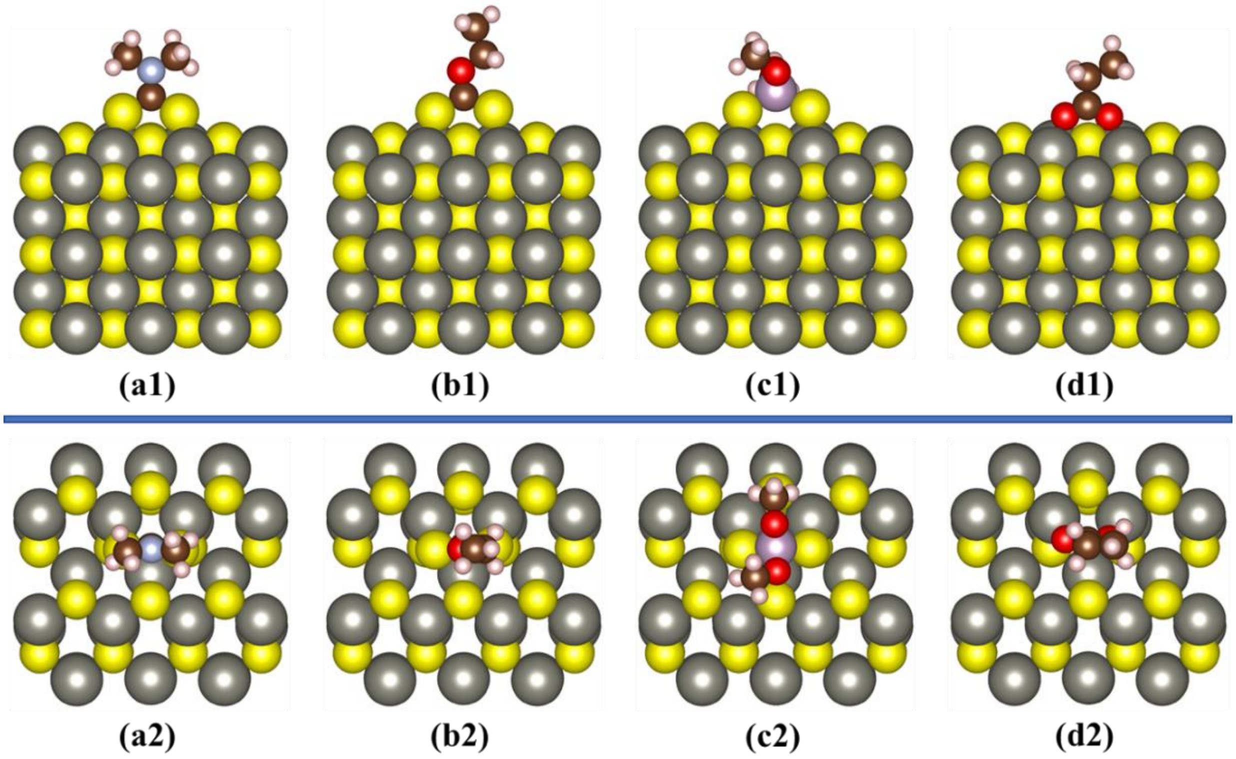

**Scheme 5.1** (a1−d1) Front views and (a2−d2) top views of the optimized structures of (a) DTC/ZnS(110), (b) EX/ZnS(110), (c) DTP/ZnS(110) and (d) AA/ZnS(110). The atoms include H(white), C (brown), N (cyan), O (red), P (magenta), S (yellow) and Zn (grey).

The adsorption of ligands has led to structural changes of the underlying surface. Probably the most striking change is that the active Zn ions on the surface are upshifted by 0.23, 0.25, 0.34 and 0.27 Å upon the adsorption of DTC, EX, DTP and AA, respectively. In this case, the preceding downshifts of the Zn ions due to the structural optimization are largely compensated, depending on the type of the binding ligand. Interestingly, after adsorption, the binding ions from the ligand, the bound Zn ion and the coordinated three sulfur ions on the surface connected in a pattern analogue to the bulk tetrahedral configurations. It is thus concluded that the ligands bind with the ZnS(110) in a preferable configuration restoring the tetrahedral configuration of the surface Zn ions as those in the inner layers or in the bulk crystal. Moreover, given the similar structures and the same type of the binding ions of the S-tailed ligands, the different variations of the position of the active Zn ions imply the different binding affinities of the ligand toward zinc sulfide. This speculation is confirmed by the calculated adsorption energies which followed the order of AA (–1.6 eV) < DTP (–0.865 eV) < EX (–0.597 eV) < DTC (–0.571 eV), indicative of a stronger binding affinity of AA toward the ZnS(110) than those of the S-tailed ligands. In addition, the effect of water molecules on the adsorption energy is approximately evaluated with the implicit $\mathrm{VASP_{sol}}$ model. Under this model, the above interaction energies increased accordingly to –1.114 eV, –0.74, –0.51 and –0.402, respectively. Although the ligand and ZnS(110) interact more weakly in the presence of implicit water molecules, the trend of the binding affinities remains unchanged, as also observed by previous DFT studies using the S-tailed ligands with and without explicit water molecules.[24]

| | DFT | Exp. |
|---|---|---|
| **Zn3–Zn4** | 3.59Å | 3.82Å |
| **O–C1** | 1.34Å | 1.39Å |
| **O–C2** | 1.46Å | 1.44Å |
| **∠OC1S1** | 111.60° | 113.20° |
| **∠OC1S2** | 120.00° | 122.00° |

**Figure 5.2** Comparison of the relevant geometrical parameters of the calculated and experimental EX/ZnS(110) system.[45]

We further calculated the PDOS of the ions directly involved in the bonding event to shed light on the distinct binding abilities of the ligands toward ZnS(110), which has been verified helpful in revealing the underlying bonding mechanism.[46,47] The plots presented in Figure 5.3 include PDOS of the binding ions from the ligand placed in the middle of the vacuum region ($S_{sus}$ or $O_{sus}$) and those from the adsorbed ligand on ZnS(110) ($S_{ads}$ or $O_{ads}$) as well as the active Zn ions on the underlying surface (Zn).

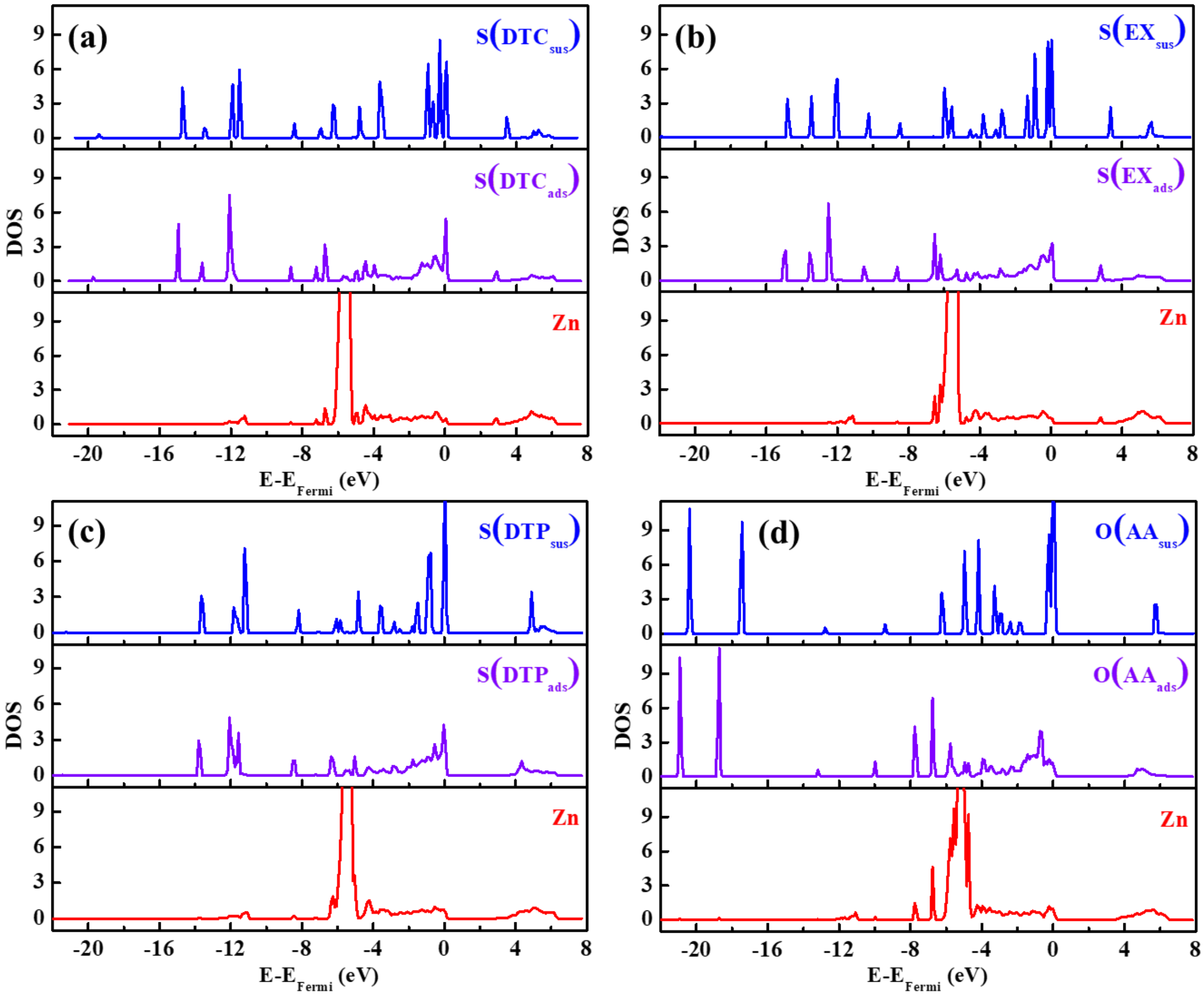

**Figure 5.3** PDOS of the binding ions for (a) DTC/ZnS(110), (b) EX/ZnS(110), (c) DTP/ZnS(110) and (d) AA/ZnS(110).

As shown, the adsorption of ligands induced clear PDOS variations in two typical energy ranges for all cases. From −6 eV to the Fermi level, the narrow and localized ligand states get widened and multiply split due to the coupling with the electronic states of the underneath Zn ions. This states coupling is further verified by the clear signature of Zn states in those of the ligand, and the ligand states can also be seen within the PDOS of the Zn ions in contact. Since the states resonance is a feature for covalency, the mixture of the electronic states of the ligand and Zn ions suggests a partial covalent character of the resulting ligand−ZnS(110) bond. In contrast, the shape of the ligand states below −6 eV only experienced negligible changes because of the inert nature of these low lied states in energy. However, these states are found to be negatively shifted upon the adsorption of ligands. This phenomenon, together with the filling of the states around the Fermi level, indicates the electron transfer from the surface to the adsorbed ligands. Furthermore, it is noted that the overall PDOS features involving the binding ions closely resemble those of the bare surface which indicates the similarities of the bond characters between ligand−ZnS(110) and that on the surface. Combining with the aforementioned adsorption configurations, it can be seen that the geometric and electronic structure of the bulk or inner layer of zinc sulfide predicts to a large extent the interaction mechanism of the ligands toward ZnS(110).

The interaction between atoms induces electron density redistributions around atomic nuclei or along the bonds, corresponding to the two limits of ionic bond and covalent bond, respectively.[48] Therefore, the electron flow during the bonding interaction can give more details on the ligand−ZnS(110) bond character, particularly the relative ionic portion of the bond. The charge density difference contours ($\Delta\rho$) containing the bonding ions was constructed and presented in

Figure 5.4.[49] The line profile starting from Zn to the bound ion of the ligand, as illustrated by the dashed black arrow line, is also presented in Figure 5.4(e).

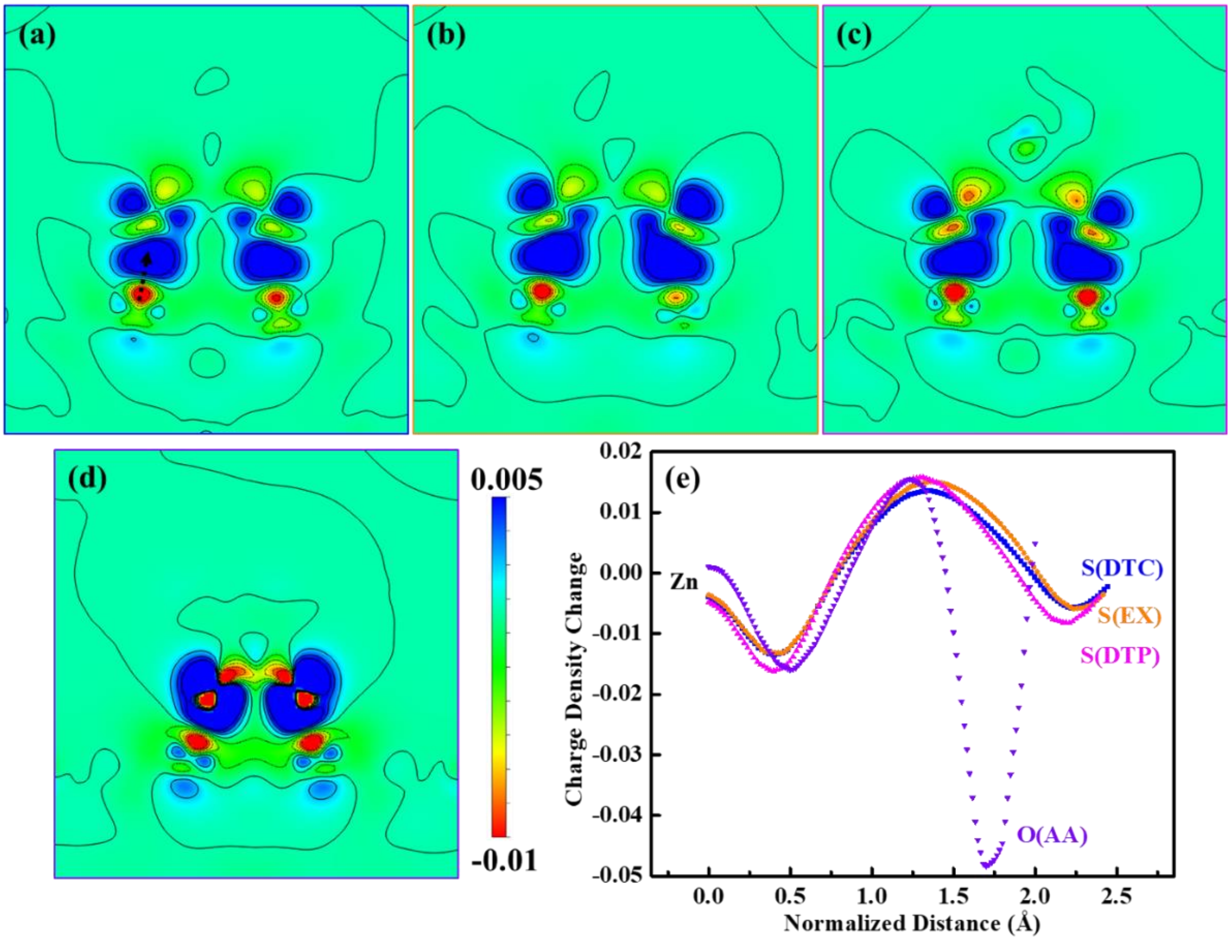

**Figure 5.4** Slices of the charge density difference profiles for (a) DTC/ZnS(110), (b) EX/ZnS(110), (c) DTP/ZnS(110) and (d) AA/ZnS(110), (e) the line profiles along Zn−S or Zn−O.

Clearly, the adsorption of ligand leads to pronounced charge redistributions for all the cases, where the charge density around Zn ions is largely depleted, whereas the electrons significantly accumulate around the binding ions from the adsorbed ligand, especially the O from AA which exhibited the largest degree of electron accumulation. This indicates considerable electrostatic contribution to the resulting interaction energy, consistent with the observed ionic interaction from the above PDOS analysis.[50]

The adsorption induced electron transfer can be quantized by integration of the electron density within the Bader regions using the Bader scheme.[51] The calculated Bader charges [Figure 5.5(a)] of the adsorbed ligands are −0.09, −0.22, −0.32 and −0.65 for DTC/ZnS(110), EX/ZnS(110), DTP/ZnS(110) and AA/ZnS(110), respectively. As expected, the largest partial charge is located on the O ion from AA, causing their positions to show the strongest ion-induced dipole interactions with the adjacent Zn ions.

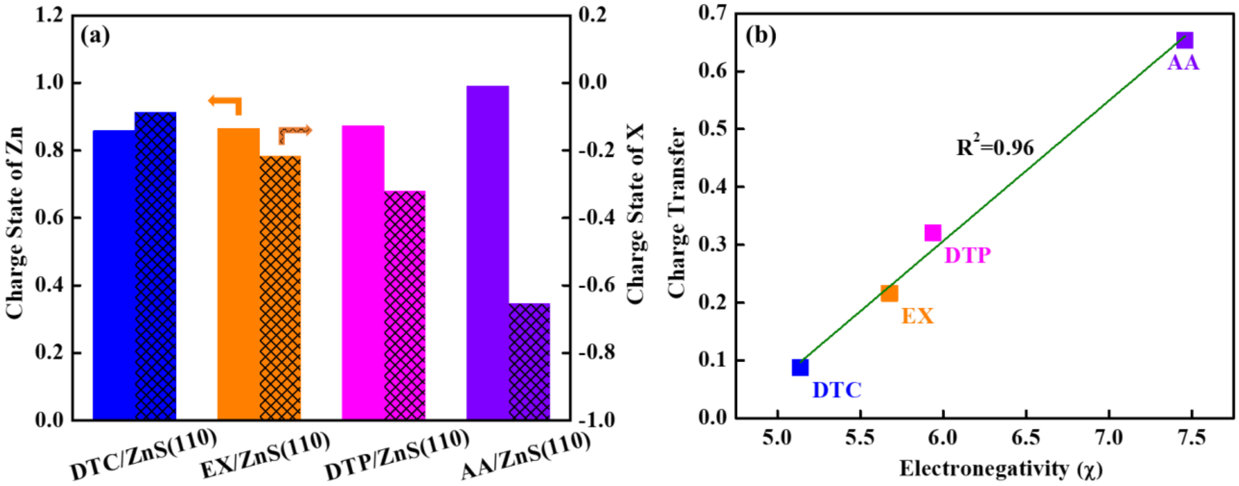

**Figure 5.5** (a) Bader charge states of the binding Zn ion (solid bars) and the bound ligand (patterned bars), (b) the transferred charge plotted against the electronegativity (χ).

As plotted in Figure 5.5(b), the relative charge states of the ligand are strongly related to the corresponding electronegativities of the isolated ligands, showing an approximately linear correlation. Therefore, the contrasting distributions of the electrons because of the adsorption of ligands can be attributed to the distinct attracting abilities of the interacting ions toward the valence electrons.[52,53] Such abilities can be measured by the intrinsic electronegativity of the ligand, and thereby providing extra evidence on the ionic nature of the ligand–ZnS(110) bond.

The resulting ligand–ZnS(110) bond character was further checked through the electron localization function (ELF) which reflects the probability of finding electron pairs and scales from 0 to 1. The ELF value along the bond indicates the relative degree of bond covalency in terms of electron pairing and hence has been widely adopted to measure the nature of chemical bonds.[54,55] The ELF of the four cases and the color scale bar are provided in Figure 5.6.

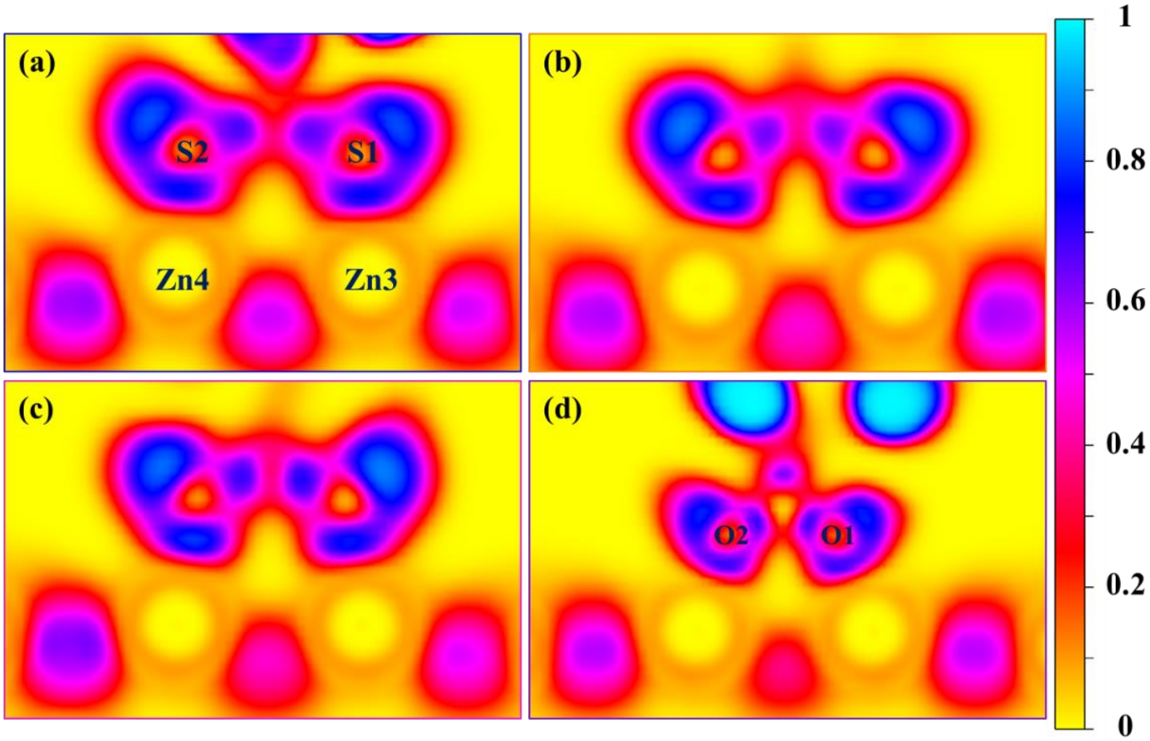

**Figure 5.6** Slices of the ELF profiles for (a) DTC/ZnS(110), (b) EX/ZnS(110), (c) DTP/ZnS(110) and (d) AA/ZnS(110).

The absence of the localized domains within the bonding regions further supports the weak covalency of the interaction. Collectively, we can safely draw the conclusion that the ligand−ZnS(110) bond is strongly ionic with limited covalency, in contrast to the implicit view of the conventional covalent interaction mechanism.

Having investigated the ligand−ZnS(110) interaction mechanism and the resulting bonding character, we now turn to the hydrophobic functionalization of zinc sulfide in the context of froth flotation. The goals are to address the previously un-elucidated inconsistency [Figure 5.7(a)] between the ligand−zinc sulfide binding energy and the hydrophobic functionality of the ligands toward zinc sulfide as measured by the solubility product, and then identify the key attribute of ligands determining the surface hydrophobicity. Since the ligands bind with ZnS(110) in a predominantly ionic bond with limited covalency, the resulting adsorption energy comprises of both the electrostatic and hybridization contributions. Apparently, the covalent interaction is not responsible for the increased binding strengths of the ligands with ZnS(110) from DTC, EX and DTP to AA.[56] The ionic interaction thus plays a decisive role in the resulting trend of the adsorption energy, assuming that the hybridization effect in the four cases are approximately equivalent because of the limited and comparable covalency. In this case, the trend of the ligand binding strength with ZnS(110) (i.e., DTC < EX < DTP < AA) is rationalized to arise from the increasing ionic contribution. Moreover, given the similar and short hydrocarbon chain (e.g., 5 carbon atoms in the tail for EX) of the ligands used in the flotation of sphalerite, the ligand−ZnS(110) bonding character, beyond any doubt, significantly affects the resulting surface hydrophobicity.

According to the electronegativity model in the context of minerals flotation, the relative electronegativity difference [$(\Delta\lambda)^2$] between the ligand head group (e.g., $-OCS_2$, $-NCS_2$ or $-O_2PS_2$) and the active metal atom on mineral surface (e.g., Cu, Pb or Fe) indicates the collecting ability of the ligand toward minerals.[57] Specifically, a smaller value of $(\Delta\lambda)^2$ indicates a stronger covalent bonding interaction which contributes to a more hydrophobic surface. Conversely, a larger value of $(\Delta\lambda)^2$ represents a weaker covalent bond and a less hydrophobic surface. Therefore, the less ionic bond between the thiol ligands and ZnS(110) gives rise to desired surface hydrophobicity, leading to high collecting efficiencies of the ligands toward sphalerite mineral particles. On the other hand, the O-tailed ligands bind with ZnS(110) in a more ionic character. As a result, the hydrocarbon chain containing more carbon atoms is required to achieve comparable collecting performance toward sphalerite as those of the S-tailed surfactants.[57]

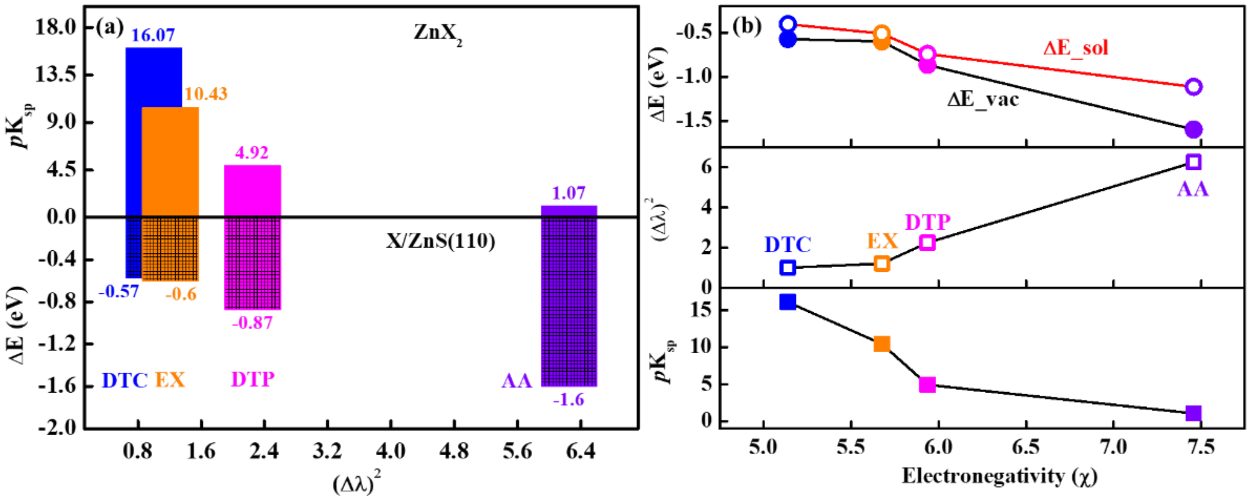

**Figure 5.7** (a) The solubility product ($pK_{sp}$) and binding energy (ΔE) plotted against the electronegativity difference [$(\Delta\lambda)^2$], (b) the $pK_{sp}$, ΔE and $(\Delta\lambda)^2$ as a function of the ligand electronegativity (χ).

We can now see that the ligand electronegativity (χ) can potentially serve as a powerful descriptor predicating the hydrophobic functionality of the ligand toward ZnS at a given hydrocarbon tail. This is further confirmed by the extraordinary correlations between the electronegativity and other critical and recognized evaluation parameters, i.e., the empirical electronegativity difference between ligand head group and atomic Zn [$(\Delta\lambda)^2$], the adsorption energy ($\Delta E$) and the solubility product of the ligand−Zn compound counterpart ($pK_{sp}$), as plotted in Figure 5.7(b). Therefore, when engineering the ligand for enhanced hydrophobic functionality toward metal sulfides, the ligand electronegativity should be particularly considered. Moreover, the methodology adopted is also instructive for other material functionalization cases in which the computational parameters other than the binding energy need to be considered depending on specific functionalization attempts.

## 5.4 Conclusions

Chemical functionalization of metal sulfides by the adsorption of specific ligands have drawn extensive attentions in a wide range of engineering applications. In this work, we performed density functional theory (DFT) calculations to explore the intrinsic interaction mechanism between the commonly used S- and O-tailed functionalization groups and ZnS(110) with a particular emphasis on the resulting bond character. The ligands were shown to preferably bind with ZnS(110) in a bidentate bridging mode, restoring the missing surface Zn−S bond as that in the bulk crystal or inner layers both geometrically and electronically. The combined projected density of states (PDOS), charge density difference, Bader charge and electron localization function (ELF) calculations demonstrated that the resulting ligand−ZnS(110) bond is predominantly ionic with minor covalency, in contrast to the implicit conventional assumption of a pure covalent interaction. Moreover, it was found that the ligand electronegativity ($\chi$) plays a central role in the ligand−ZnS(110) binding, leading to such trend of the ligand binding strengths (DTC < EX < DTP < AA) and strongly correlating with the solubility product constant ($pK_{sp}$) of the corresponding ligand−Zn compound as well as the empirical electronegativity difference between the ligand head group and atomic Zn [$(\Delta\lambda)^2$]. Consequently, the ligand electronegativity was proposed as the descriptor enabling accurate prediction of the ligand hydrophobic functionality toward ZnS at a given hydrocarbon tail. Therefore, this study further advanced our understandings on the ligand−ZnS(110) interaction, and the fundamental findings obtained can be instructive in identifying specific descriptors for functionalization of many other materials as well.

## 5.5 References

(1) Shao, M.; Chang, Q.; Dodelet, J.-P.; Chenitz, R. Recent Advances in Electrocatalysts for Oxygen Reduction Reaction. *Chem. Rev.* **2016**, *116* (6), 3594–3657.

(2) Chen, Z.; Higgins, D.; Yu, A.; Zhang, L.; Zhang, J. A Review on Non-Precious Metal Electrocatalysts for PEM Fuel Cells. *Energy Environ. Sci.* **2011**, *4* (9), 3167–3192.

(3) Voiry, D.; Goswami, A.; Kappera, R.; Silva, C. D. C. C. E.; Kaplan, D.; Fujita, T.; Chen, M.; Asefa, T.; Chhowalla, M. Covalent Functionalization of Monolayered Transition Metal Dichalcogenides by Phase Engineering. *Nat. Chem.* **2015**, *7* (1), 45–49.

(4) Tao, H.; Liu, S.; Luo, J. L.; Choi, P.; Liu, Q.; Xu, Z. Descriptor of Catalytic Activity of Metal Sulfides for Oxygen Reduction Reaction: A Potential Indicator for Mineral Flotation. *J. Mater. Chem. A* **2018**, *6* (20), 9650–9656.

(5) Falkowski, J. M.; Concannon, N. M.; Yan, B.; Surendranath, Y. Heazlewoodite, $Ni_3S_2$ : A Potent Catalyst for Oxygen Reduction to Water under Benign Conditions. *J. Am. Chem. Soc.* **2015**, *137* (25), 7978–7981.

(6) Staszak-Jirkovský, J.; Malliakas, C. D.; Lopes, P. P.; Danilovic, N.; Kota, S. S.; Chang, K.-C.; Genorio, B.; Strmcnik, D.; Stamenkovic, V. R.; Kanatzidis, M. G.; et al. Design of Active and Stable Co–Mo–Sx Chalcogels as PH-Universal Catalysts for the Hydrogen Evolution Reaction. *Nat. Mater.* **2015**, *15* (2), 197–203.

(7) Wang, D. Y.; Gong, M.; Chou, H. L.; Pan, C. J.; Chen, H. A.; Wu, Y.; Lin, M. C.; Guan, M.; Yang, J.; Chen, C. W.; et al. Highly Active and Stable Hybrid Catalyst of Cobalt-Doped $FeS_2$ Nanosheets-Carbon Nanotubes for Hydrogen Evolution Reaction. *J. Am.*

*Chem. Soc.* **2015**, *137* (4), 1587–1592.

(8) Asadi, M.; Kim, K.; Liu, C.; Addepalli, A. V.; Abbasi, P.; Yasaei, P.; Phillips, P.; Behranginia, A.; Cerrato, J. M.; Haasch, R.; et al. Nanostructured Transition Metal Dichalcogenide Electrocatalysts for $CO_2$ Reduction in Ionic Liquid. *Science* **2016**, *353* (6298), 467–470.

(9) Liu, S.; Tao, H.; Liu, Q.; Xu, Z.; Liu, Q.; Luo, J.-L. Rational Design of Silver Sulfide Nanowires for Efficient $CO_2$ Electroreduction in Ionic Liquid. *ACS Catal.* **2018**, *8* (2), 1469–1475.

(10) Sarma, S. Das; Adam, S.; Hwang, E. H.; Rossi, E. Electronic Transport in Two Dimensional Graphene. *Rev. Mod. Phys.* **2010**, *83* (2), 407–470.

(11) Vaughan, D. J. Sulfide Mineralogy and Geochemistry: Introduction and Overview. *Rev. Mineral. Geochemistry* **2006**, *61* (1), 1–5.

(12) Xie, L.; Wang, J.; Shi, C.; Cui, X.; Huang, J.; Zhang, H.; Liu, Q.; Liu, Q.; Zeng, H. Mapping the Nanoscale Heterogeneity of Surface Hydrophobicity on the Sphalerite Mineral. *J. Phys. Chem. C* **2017**, *121* (10), 5620–5628.

(13) Potapova, I.; Mruk, R.; Hübner, C.; Zentel, R.; Basché, T.; Mews, A. CdSe/ZnS Nanocrystals with Dye-Functionalized Polymer Ligands Containing Many Anchor Groups. *Angew. Chemie - Int. Ed.* **2005**, *44* (16), 2437–2440.

(14) Rodríguez-Hermida S, Tsang MY, Vignatti C, Stylianou KC, Guillerm V, Pérez-Carvajal J, Teixidor F, Viñas C, Choquesillo-Lazarte D, Verdugo-Escamilla C, P. I. Switchable Surface Hydrophobicity–Hydrophilicity of a Metal–Organic Framework. *Angew. Chemie -*

*Int. Ed.* **2016**, *55* (52), 16049–16053.

(15) Lu, Z.; Chen, G.; Siahrostami, S.; Chen, Z.; Liu, K.; Xie, J.; Liao, L.; Wu, T.; Lin, D.; Liu, Y.; et al. High-Efficiency Oxygen Reduction to Hydrogen Peroxide Catalysed by Oxidized Carbon Materials. *Nat. Catal.* **2018**, *1* (2), 156–162.

(16) Schlücker, S. Surface-Enhanced Raman Spectroscopy: Concepts and Chemical Applications. *Angew. Chemie - Int. Ed.* **2014**, *53* (19), 4756–4795.

(17) Gilbert, B.; Huang, F.; Lin, Z.; Goodell, C.; Zhang, H.; Banfield, J. F. Surface Chemistry Controls Crystallinity of ZnS Nanoparticles. *Nano Lett.* **2006**, *6* (4), 605–610.

(18) Yang, H.; Li, F.; Shan, C.; Han, D.; Zhang, Q.; Niu, L.; Ivaska, A. Covalent Functionalization of Chemically Converted Graphene Sheets via Silane and Its Reinforcement. *J. Mater. Chem.* **2009**, *19* (26), 4632–4638.

(19) Abild-pedersen, F.; Studt, F.; Bligaard, T. Density Functional Theory in Surface Chemistry and Catalysis. *Proc. Natl. Acad. Sci.* **2011**, *108* (3), 937–943.

(20) Nørskov, J. K.; Bligaard, T.; Rossmeisl, J.; Christensen, C. H. Towards the Computational Design of Solid Catalysts. *Nat. Chem.* **2009**, *1* (1), 37–46.

(21) He, Y.; Fishman, Z. S.; Yang, K. R.; Ortiz, B.; Liu, C.; Goldsamt, J.; Batista, V. S.; Pfefferle, L. D. Hydrophobic CuO Nanosheets Functionalized with Organic Adsorbates. *J. Am. Chem. Soc.* **2018**, *140* (5), 1824–1833.

(22) Bealing, C. R.; Baumgardner, W. J.; Choi, J. J.; Hanrath, T.; Hennig, R. G. Predicting Nanocrystal Shape through Consideration of Surface-Ligand Interactions. *ACS Nano* **2012**, *6* (3), 2118–2127.

(23) Zherebetskyy, D.; Scheele, M.; Zhang, Y.; Bronstein, N.; Thompson, C.; Britt, D.; Salmeron, M.; Alivisatos, P.; Wang, L.-W. Hydroxylation of the Surface of PbS Nanocrystals Passivated with Oleic Acid. *Science* **2014**, *344* (6190), 1380–1384.

(24) Long, X.; Chen, Y.; Chen, J.; Xu, Z.; Liu, Q.; Du, Z. The Effect of Water Molecules on the Thiol Collector Interaction on the Galena (PbS) and Sphalerite (ZnS) Surfaces: A DFT Study. *Appl. Surf. Sci.* **2016**, *389*, 103–111.

(25) Kresse, G.; Hafner, J. Ab Initio Molecular Dynamics for Liquid Metals. *Phys. Rev. B* **1993**, *47* (1), 558–561.

(26) Kresse, G.; Hafner, J. Ab Initio Molecular-Dynamics Simulation of the Liquid-Metal–amorphous-Semiconductor Transition in Germanium. *Phys. Rev. B* **1994**, *49* (20), 14251–14269.

(27) Kresse, G.; Furthmüller, J. Efficiency of Ab-Initio Total Energy Calculations for Metals and Semiconductors Using a Plane-Wave Basis Set. *Comput. Mater. Sci.* **1996**, *6* (1), 15–50.

(28) Kresse, G.; Furthmüller, J. Efficient Iterative Schemes for Ab Initio Total-Energy Calculations Using a Plane-Wave Basis Set. *Phys. Rev. B* **1996**, *54* (16), 11169–11186.

(29) Blöchl, P. E. Projector Augmented-Wave Method. *Phys. Rev. B* **1994**, *50* (24), 17953–17979.

(30) Kresse, G. From Ultrasoft Pseudopotentials to the Projector Augmented-Wave Method. *Phys. Rev. B* **1999**, *59* (3), 1758–1775.

(31) Hammer, B.; Hansen, L. B.; Nørskov, J. K. Improved Adsorption Energetics within

Density-Functional Theory Using Revised Perdew-Burke-Ernzerhof Functionals. *Phys. Rev. B* **1999**, *59* (11), 7413–7421.

(32) Monkhorst, H. J.; Pack, J. D. Special Points for Brillouin-Zone Integrations. *Phys. Rev. B* **1976**, *13* (12), 5188–5192.

(33) Downs, R. T.; Hall-Wallace, M. The American Mineralogist Crystal Structure Database. *Am. Mineral.* **2003**, *88* (1), 247–250.

(34) Liu, J.; Wen, S.; Deng, J.; Chen, X.; Feng, Q. DFT Study of Ethyl Xanthate Interaction with Sphalerite(110) Surface in the Absence and Presence of Copper. *Appl. Surf. Sci.* **2014**, *311*, 258–263.

(35) Balantseva, E.; Berlier, G.; Camino, B.; Lessio, M.; Ferrari, A. M. Surface Properties of ZnS Nanoparticles: A Combined DFT and Experimental Study. *J. Phys. Chem. C* **2014**, *118* (41), 23853–23862.

(36) Mathew, K.; Sundararaman, R.; Letchworth-weaver, K.; Arias, T. A.; Hennig, R. G. Implicit Solvation Model for Density-Functional Study of Nanocrystal Surfaces and Reaction Pathways. *J. Chem. Phys.* **2014**, *140* (8), 084106.

(37) Fishman, M.; Zhuang, H. L.; Mathew, K.; Dirschka, W.; Hennig, R. G. Accuracy of Exchange-Correlation Functionals and Effect of Solvation on the Surface Energy of Copper. *Phys. Rev. B* **2013**, *87* (24), 245402.

(38) Kitchaev, D. A.; Ceder, G. Evaluating Structure Selection in the Hydrothermal Growth of $FeS_2$ Pyrite and Marcasite. *Nat. Commun.* **2016**, *7*, 13799.

(39) Garza, A.; Bell, A. T.; Head-Gordon, M. Is Subsurface Oxygen Necessary for the

Electrochemical Reduction of $CO_2$ on Copper? *J. Phys. Chem. Lett.* **2018**, *9* (3), 601–606.

(40) Gordon, W. O.; Xu, Y.; Mullins, D. R.; Overbury, S. H. Temperature Evolution of Structure and Bonding of Formic Acid and Formate on Fully Oxidized and Highly Reduced $CeO_2$(111). *Phys. Chem. Chem. Phys.* **2009**, *11* (47), 11171–11183.

(41) Chowdhry, M. Theoretical Study on Reactivity of Different Sulfide Collectors and Their Binding Affinity Toward Cu (II), Zn (II) and Pb (II) Ions, Ph.D dissertation, University of Alberta, Edmonton, AB, 2015.

(42) Vaughan, D. J. Chemical Bonding in Sulfide Minerals. *Rev. Mineral. Geochemistry* **2006**, *61* (1), 231–264.

(43) Long, X.; Chen, J.; Chen, Y. Adsorption of Ethyl Xanthate on ZnS(110) Surface in the Presence of Water Molecules: A DFT Study. *Appl. Surf. Sci.* **2016**, *370*, 11–18.

(44) Porento, M.; Hirva, P. Effect of Copper Atoms on the Adsorption of Ethyl Xanthate on a Sphalerite Surface. *Surf. Sci.* **2005**, *576* (1–3), 98–106.

(45) Larsson, M. L.; Holmgren, A.; Forsling, W. Xanthate Adsorbed on ZnS Studied by Polarized FTIR-ATR Spectroscopy. *Langmuir* **2000**, *16* (21), 8129–8133.

(46) Gudmundsdóttir, S.; Tang, W.; Henkelman, G.; Jónsson, H.; Skúlason, E. Local Density of States Analysis Using Bader Decomposition for $N_2$ and $CO_2$ Adsorbed on Pt(110)-(1 × 2) Electrodes. *J. Chem. Phys.* **2012**, *137* (16), 164705.

(47) Zheng, C.; Apeloig, Y.; Hoffmann, R. Bonding and Coupling of C1 Fragments on Metal Surfaces. *J. Am. Chem. Soc.* **1988**, *110* (3), 749–774.

(48) Evarestov, R. A. *Quantum Chemistry of Solids: The LCAO First Principles Treatment of Crystals. Springer Science & Business Media,* 2007.

(49) Mondal, B.; Bag, R.; Ghorai, S.; Bakthavachalam, K.; Jemmis, E. D.; Ghosh, S. Synthesis, Structure, Bonding, and Reactivity of Metal Complexes Comprising Diborane(4) and Diborene(2): $[\{Cp^*Mo(CO)_2\}_2\{\mu\text{-}\eta^2{:}\eta^2\text{-}B_2H_4\}]$ and $[\{Cp^*M(CO)_2\}_2B_2H_2M(CO)_4]$, M=Mo,W. *Angew. Chemie - Int. Ed.* **2018**, *57* (27), 8079–8083.

(50) Hollerer, M.; Lüftner, D.; Hurdax, P.; Ules, T.; Soubatch, S.; Tautz, F. S.; Koller, G.; Puschnig, P.; Sterrer, M.; Ramsey, M. G. Charge Transfer and Orbital Level Alignment at Inorganic/Organic Interfaces: The Role of Dielectric Interlayers. *ACS Nano* **2017**, *11* (6), 6252–6260.

(51) Yu, M.; Trinkle, D. R. Accurate and Efficient Algorithm for Bader Charge Integration. *J. Chem. Phys.* **2011**, *134* (6), 1–19.

(52) Bassett, C. A. L.; Herrmann, I. A Quantitative Theory of the Character of Chemical Bonding in Binary Compounds. *Nature* **1961**, *192* (4798), 133–135.

(53) Ormeci, A.; Simon, A.; Grin, Y. Structural Topology and Chemical Bonding in Laves Phases. *Angew. Chemie - Int. Ed.* **2010**, *49* (47), 8997–9001.

(54) Silvi, B.; Savin, A. Classification of Chemical Bonds Based on Topological Analysis of Electron Localization Functions. *Nature* **1994**, *371(6499)*, 683-686.

(55) Tsuji, Y.; Dasari, P. L. V. K.; Elatresh, S. F.; Hoffmann, R.; Ashcroft, N. W. Structural Diversity and Electron Confinement in Li4N: Potential for 0-D, 2-D, and 3-D Electrides. *J. Am. Chem. Soc.* **2016**, *138* (42), 14108–14120.

(56) Shayeghi, A.; Johnston, R. L.; Rayner, D. M.; Schäfer, R.; Fielicke, A. The Nature of Bonding between Argon and Mixed Gold-Silver Trimers. *Angew. Chemie - Int. Ed.* **2015**, *54* (36), 10675–10680.

(57) Wang, D. *Flotation Reagents: Applied Surface Chemistry on Minerals Flotation and Energy Resources Beneficiation*; Springer Singapore, 2016.

# Chapter 6 Conclusions and Future Work

## 6.1 Major conclusions

The work presented in this dissertation explored the catalytic activity trend of metal sulfides for oxygen reduction reaction (ORR) and the ligand−metal sulfide binding mechanism.

The ORR activities of metal sulfides were studied using density functional theory (DFT) calculations. The Gibbs free energy diagram revealed that the ORR activities of $FeS_2$ and $CuFeS_2$ are similar to that of Pt, but different from those of PbS and ZnS. The relative theoretical overpotentials agree well with the experimental trend Pt < $FeS_2$ < $CuFeS_2$ < PbS < ZnS. The distinct ORR behaviors were found to originate from the different oxygen binding energies, as governed by the underlying electronic structure. Moreover, the bulk centroid (relative to the Fermi level) of the occupied S-3p band of metal sulfide was established as the potential descriptor which correlates well with the experimental rest potentials for sulfide minerals in xanthate solutions.

The adsorption mechanism of typical S/O-tailed ligands on the lead sulfide PbS(100) surface was studied using DFT calculations. Extensive analyses have been performed to comprehend the resulting ligand−PbS(100) bond character by the joint projected density of states (PDOS), charge density difference, Bader charge and electron localization function (ELF) calculations. The ligand−PbS(100) bond was revealed to be predominantly ionic with minor covalency, in direct contrast to the classical view of covalent bonding. Moreover, instead of the generally used binding energy concept, the ligand electronegativity ($\chi$) was established as the potential descriptor allowing more accurate prediction of the relative ligand hydrophobic functionality toward PbS with a certain normal hydrocarbon tail. The effectiveness of this descriptor was supported by its extraordinary correlations with both the recognized solubility product constant ($pK_{sp}$) of the corresponding ligand−Pb compound and the ligand/atomic Pb electronegativity difference [$(\Delta\lambda)^2$].

Using DFT calculations, we studied the binding mechanism between the commonly used S- and O-tailed functionalization groups and ZnS(110) with an emphasis on the resulting bond character. The combined PDOS, charge density difference, Bader charge and ELF calculations demonstrated that the resulting ligand−ZnS(110) bond is predominantly ionic with minor covalency, in contrast to the conventional assumption of a pure covalent interaction. Moreover, it was found that the ligand electronegativity ($\chi$) plays a central role in the ligand−ZnS(110) binding, leading to such trend of the ligand binding strengths (DTC < EX < DTP < AA) and strongly correlating with the solubility product constant ($pK_{sp}$) of the corresponding ligand−Zn compound as well as the empirical electronegativity difference between the ligand head group and atomic Zn [$(\Delta\lambda)^2$]. Consequently, the ligand electronegativity was proposed as the potential descriptor enabling accurate prediction of the ligand hydrophobic functionality toward ZnS at a given hydrocarbon tail.

## 6.2 Original contributions

DFT calculations in combination with the computational hydrogen model was applied for the first time to study the catalytic activities of metal sulfides for ORR in the context of froth flotation. This work provided atomistic insights into the distinct catalyzing abilities of metal sulfides for ORR. Moreover, we identified an effective descriptor linking the intrinsic attribute of metal sulfides with the critical experimental metric in connection with the flotation of sulfide minerals. The established descriptor–activity relationship holds the promise in prediction of the overall electrochemical behavior of sulfide minerals and hence potentially benefits the mineral flotation.

In stark contrast to the conventional assumption of a pure covalent interaction, we revealed that the ligand−metal sulfide (galena and sphalerite) bond is essential ionic with limited covalency. Besides, we addressed the failure of the ligand−metal sulfide binding energy in predicting the hydrophobic functionality of the ligand toward metal sulfide. Instead, we proposed that the ligand electronegativity allows more accurate prediction of the hydrophobic functionality of the ligand toward metal sulfide. This work further advanced our understandings on the ligand−metal sulfide interaction. The fundamental insights into the ligand−metal sulfide bond character, together with its demonstrated applicability in the hydrophobization case of metal sulfides, offer new perspective on the descriptor-based design of ligand with tailored functionalities as well.

## 6.3 Suggestions for future work

(1) Existing DFT studies have been mainly focused on the ligand–metal sulfide binding with an emphasis on pyrite ($FeS_2$), chalcopyrite ($CuFeS_2$), galena (PbS) and sphalerite (ZnS) due to the relatively simple crystal structure and well-defined cleavages. The metal sulfides which are commonly encountered such as pyrrhotite ($Fe_{1-x}S$, $x$ = 0-0.17) and pentlandite ($(Fe,Ni)_9S_8$)should also be investigated.

(2) Different computational methods have been employed in specific studies, while systematic studies covering a broad class of metal sulfides remain unavailable. Systematic simulations with well-converged geometries should be conducted to build a unified database for reference.

(3) Metal ion plays a critical role in flotation of metal sulfide minerals. The effect of metal ions on ORR activity of metal sulfide and ligand–metal sulfide binding as well as the corresponding descriptors should be studied.

(4) The flotation process in real flotation pulp is very complicated, and simulations with more complex technical flavors and model chemistries should be further explored.

# Bibliography

(1-1) Wills, B. A.; Finch, J. A. *Wills' Mineral Processing Technology: An Introduction to the Practical Aspects of Ore Treatment and Mineral Recovery*; Butterworth-Heinemann, 2016.

(1-2) Vaughan, D. J. Sulfide Mineralogy and Geochemistry: Introduction and Overview. *Rev. Mineral. Geochemistry* **2006**, *61* (1), 1–5.

(1-3) Xie, L.; Wang, J.; Shi, C.; Cui, X.; Huang, J.; Zhang, H.; Liu, Q.; Liu, Q.; Zeng, H. Mapping the Nanoscale Heterogeneity of Surface Hydrophobicity on the Sphalerite Mineral. *J. Phys. Chem. C* **2017**, *121* (10), 5620–5628.

(1-4) Strand, A.; Zasadowski, D.; Norgren, M.; Hedenstrom, E.; Willfor, S.; Sundberg, A. Selective Froth Flotation of Pitch Components from Spruce TMP Process Water. *Appita J.* **2012**, *65* (4), 337–346.

(1-5) Allison, S.; Goold, L.; Granville, A. A Determination of the Products of Reaction Between Various Sulfide Minerals and Aqueous Xanthate Solution, and a Correlation of the Products with Electrode Rest Potentials. *Metall. Trans.* **1972**, *3* (10), 2613–2618.

(1-6) Mu, Y.; Peng, Y.; Lauten, R. A. Electrochemistry Aspects of Pyrite in the Presence of Potassium Amyl Xanthate and a Lignosulfonate-Based Biopolymer Depressant. *Electrochim. Acta* **2015**, *174* (1), 133–142.

(1-7) Schlücker, S. Surface-Enhanced Raman Spectroscopy: Concepts and Chemical Applications. *Angew. Chemie - Int. Ed.* **2014**, *53* (19), 4756–4795.

(1-8) Gilbert, B.; Huang, F.; Lin, Z.; Goodell, C.; Zhang, H.; Banfield, J. F. Surface Chemistry Controls Crystallinity of ZnS Nanoparticles. *Nano Lett.* **2006**, *6* (4), 605–610.

(1-9) Yang, H.; Li, F.; Shan, C.; Han, D.; Zhang, Q.; Niu, L.; Ivaska, A. Covalent Functionalization of Chemically Converted Graphene Sheets via Silane and Its Reinforcement. *J. Mater. Chem.* **2009**, *19* (26), 4632–4638.

(1-10) Voiry, D.; Goswami, A.; Kappera, R.; Silva, C. D. C. C. E.; Kaplan, D.; Fujita, T.; Chen, M.; Asefa, T.; Chhowalla, M. Covalent Functionalization of Monolayered Transition Metal Dichalcogenides by Phase Engineering. *Nat. Chem.* **2015**, *7* (1), 45–49.

(1-11) Xie, L.; Wang, J.; Shi, C.; Huang, J.; Zhang, H.; Liu, Q.; Liu, Q.; Zeng, H. Probing Surface Interactions of Electrochemically Active Galena Mineral Surface Using Atomic Force Microscopy. *J. Phys. Chem. C* **2016**, *120* (39), 22433–22442.

(1-12) Chandra, A. P.; Gerson, A. R. A Review of the Fundamental Studies of the Copper Activation Mechanisms for Selective Flotation of the Sulfide Minerals, Sphalerite and Pyrite. *Adv. Colloid Interface Sci.* **2009**, *145* (1–2), 97–110.

(1-13) Kohn, W.; Becke, A. D.; Parr, R. G. Density Functional Theory of Electronic Structure. *J. Phys. Chem.* **1996**, *100* (31), 12974–12980.

(1-14) Lee, J. G. *Computational Materials Science: An Introduction*; Crc Press, 2016.

(1-15) Cramer, C. J. *Essentials of Computational Chemistry Theories and Models*, Second Edi.; John Willey & Sons Ltd: Chichester, 2004.

(1-16) Pierre, H.; Kohn, W. Inhomogeneous Electron Gas. *Phys. Chem. Chem. Phys.* **1964**, *136* (3B), 864–871.

(1-17) Kohn, W. and Sham, L. J. Self-Consistent Equations Including Exchange and Correlation Effects. *Phys. Rev.* **1965**, *140* (4A), A1133.

(1-18) Perdew, J. P.; Wang, Y. Accurate and Simple Analytic Representation of the Electron Gas Correlation Energy. *Phys. Rev. B* **1992**, *45* (23), 13244–13249.

(1-19) Perdew, J. P.; Burke, K.; Ernzerhof, M. Generalized Gradient Approximation Made Simple. *Phys. Rev. Lett.* **1996**, *77* (18), 3865–3868.

(1-20) Hammer, B.; Hansen, L. B.; Nørskov, J. K. Improved Adsorption Energetics within Density-Functional Theory Using Revised Perdew-Burke-Ernzerhof Functionals. *Phys. Rev. B* **1999**, *59* (11), 7413–7421.

(1-21) Perdew, J. P.; Ernzerhof, M.; Burke, K. Rationale for Mixing Exact Exchange with Density Functional Approximations. *J. Chem. Phys.* **1996**, *105* (22), 9982–9985.

(1-22) Heyd, J.; Scuseria, G. E.; Ernzerhof, M. Hybrid Functionals Based on a Screened Coulomb Potential. *J. Chem. Phys.* **2003**, *118* (18), 8207–8215.

(1-23) Blöchl, P. E. Projector Augmented-Wave Method. *Phys. Rev. B* **1994**, *50* (24), 17953–17979.

(1-24) Nørskov, J. K.; Bligaard, T.; Rossmeisl, J.; Christensen, C. H. Towards the Computational Design of Solid Catalysts. *Nat. Chem.* **2009**, *1* (1), 37–46.

(1-25) Neese, F., Atanasov, M., Bistoni, G., Maganas, D. and Ye, S. Chemistry and Quantum Mechanics in 2019: Give Us Insight and Numbers. *J. Am. Chem. Soc.* **2019**, *141* (7), 2814–2824.

(1-26) Nørskov, J. K.; Abild-Pedersen, F.; Studt, F.; Bligaard, T. Density Functional Theory in Surface Chemistry and Catalysis. *Proc. Natl. Acad. Sci.* **2011**, *108* (3), 937–943.

(1-27) Kulkarni, A.; Siahrostami, S.; Patel, A.; Nørskov, J. K. Understanding Catalytic Activity Trends in the Oxygen Reduction Reaction. *Chem. Rev.* **2018**, *118* (5), 2302–2312.

(1-28) Hammer, B.; Nørskov, J. K. Electronic Factors Determining the Reactivity of Metal Surfaces. *Surf. Sci.* **1995**, *343* (3), 211–220.

(1-29) Chen, J.; Long, X.; Chen, Y. Comparison of Multilayer Water Adsorption on the Hydrophobic Galena (PbS) and Hydrophilic Pyrite ($FeS_2$) Surfaces: A DFT Study. *J. Phys. Chem. C* **2014**, *118* (22), 11657–11665.

(1-30) Li, Y., Chen, J., Chen, Y., Zhu, Y. and Liu, Y. DFT Simulation on Interaction of $H_2O$ Molecules with ZnS and Cu-Activated Surfaces. *J. Phys. Chem. C* **2019**, *123* (5), 3048–3057.

(1-31) Sarvaramini, A.; Larachi, F. Understanding the Interactions of Thiophosphorus Collectors with Chalcopyrite through DFT Simulation. *Comput. Mater. Sci.* **2017**, *132*, 137–145.

(1-32) Waterson, C. N.; Sindt, J. O.; Cheng, J.; Tasker, P. A.; Morrison, C. A. First-Principles Study on Ligand Binding and Positional Disorder in Pentlandite. *J. Phys. Chem. C* **2015**, *119* (45), 25457–25468.

(1-33) Chen, Y.; Chen, J.; Lan, L.; Yang, M. The Influence of the Impurities on the Flotation Behaviors of Synthetic ZnS. *Miner. Eng.* **2012**, *27–28*, 65–71.

(1-34) Long, X.; Chen, Y.; Chen, J.; Xu, Z.; Liu, Q.; Du, Z. The Effect of Water Molecules on the Thiol Collector Interaction on the Galena (PbS) and Sphalerite (ZnS) Surfaces: A DFT Study. *Appl. Surf. Sci.* **2016**, *389*, 103–111.

(1-35) Sarvaramini, A.; Larachi, F.; Hart, B. Collector Attachment to Lead-Activated Sphalerite–Experiments and DFT Study on PH and Solvent Effects. *Appl. Surf. Sci.* **2016**, *367*, 459–472.

(1-36) Yin, Z.; Hu, Y.; Sun, W.; Zhang, C.; He, J.; Xu, Z.; Zou, J.; Guan, C.; Zhang, C.; Guan, Q.; et al. Adsorption Mechanism of 4-Amino-5-Mercapto-1,2,4-Triazole as Flotation Reagent on Chalcopyrite. *Langmuir* **2018**, *34* (13), 4071–4083.

(2-1) Kresse, G.; Hafner, J. Ab Initio Molecular Dynamics for Liquid Metals. *Phys. Rev. B* **1993**, *47* (1), 558–561.

(2-2) Kresse, G.; Hafner, J. Ab Initio Molecular-Dynamics Simulation of the Liquid-Metal–amorphous-Semiconductor Transition in Germanium. *Phys. Rev. B* **1994**, *49* (20), 14251–14269.

(2-3) Kresse, G.; Furthmüller, J. Efficiency of Ab-Initio Total Energy Calculations for Metals and Semiconductors Using a Plane-Wave Basis Set. *Comput. Mater. Sci.* **1996**, *6* (1), 15–50.

(2-4) Kresse, G.; Furthmüller, J. Efficient Iterative Schemes for Ab Initio Total-Energy Calculations Using a Plane-Wave Basis Set. *Phys. Rev. B* **1996**, *54* (16), 11169–11186.

(2-5) Blöchl, P. E. Projector Augmented-Wave Method. *Phys. Rev. B* **1994**, *50* (24), 17953–17979.

(2-6) Kresse, G. From Ultrasoft Pseudopotentials to the Projector Augmented-Wave Method.

*Phys. Rev. B* **1999**, *59* (3), 1758–1775.

(2-7) Hafner, J. Ab-Initio Simulations of Materials Using VASP: Density-Functional Theory and Beyond. *J. Comput. Chem.* **2018**, *29* (13), 2044–2078.

(2-8) Mathew, K.; Sundararaman, R.; Letchworth-weaver, K.; Arias, T. A.; Hennig, R. G. Implicit Solvation Model for Density-Functional Study of Nanocrystal Surfaces and Reaction Pathways. *J. Chem. Phys.* **2014**, *140* (8), 084106.

(2-9) Fishman, M.; Zhuang, H. L.; Mathew, K.; Dirschka, W.; Hennig, R. G. Accuracy of Exchange-Correlation Functionals and Effect of Solvation on the Surface Energy of Copper. *Phys. Rev. B* **2013**, *87* (24), 245402.

(2-10) Kitchaev, D. A.; Ceder, G. Evaluating Structure Selection in the Hydrothermal Growth of $FeS_2$ Pyrite and Marcasite. *Nat. Commun.* **2016**, *7*, 13799.

(2-11) Garza, A.; Bell, A. T.; Head-Gordon, M. Is Subsurface Oxygen Necessary for the Electrochemical Reduction of $CO_2$ on Copper? *J. Phys. Chem. Lett.* **2018**, *9* (3), 601–606.

(2-12) Yu, M.; Trinkle, D. R. Accurate and Efficient Algorithm for Bader Charge Integration. *J. Chem. Phys.* **2011**, *134* (6), 1–19.

(2-13) Fuentealba, P., Chamorro, E. and Santos, J. C. Understanding and Using the Electron Localization. *Theor. Asp. Chem. React.* **2007**, *19*, 57–85.

(2-14) Silvi, B.; Savin, A. Classification of Chemical Bonds Based on Topological Analysis of Electron Localization Functions. *Nature* **1994**, *371*, 683–686.

(2-15) Tsuji, Y.; Dasari, P. L. V. K.; Elatresh, S. F.; Hoffmann, R.; Ashcroft, N. W. Structural

Diversity and Electron Confinement in $Li_4N$: Potential for 0-D, 2-D, and 3-D Electrides. *J. Am. Chem. Soc.* **2016**, *138* (42), 14108–14120.

(3-1) Zhang, H.; Kim, Y. K.; Hunter, T. N.; Brown, A. P.; Lee, J. W.; Harbottle, D. Organically Modified Clay with Potassium Copper Hexacyanoferrate for Enhanced $Cs^+$ Adsorption Capacity and Selective Recovery by Flotation. *J. Mater. Chem. A* **2017**, *5* (29), 15130–15143.

(3-2) Xing, Y.; Gui, X.; Cao, Y. The Hydrophobic Force for Bubble–particle Attachment in Flotation–a Brief Review. *Phys. Chem. Chem. Phys.* **2017**, *19* (36), 24421–24435.

(3-3) Anthore-Dalion, L.; Liu, Q.; Zard, S. Z. A Radical Bidirectional Fragment Coupling Route to Unsymmetrical Ketones. *J. Am. Chem. Soc.* **2016**, *138* (27), 8404–8407.

(3-4) Chandra, A. P.; Gerson, A. R. A Review of the Fundamental Studies of the Copper Activation Mechanisms for Selective Flotation of the Sulfide Minerals, Sphalerite and Pyrite. *Adv. Colloid Interface Sci.* **2009**, *145* (1–2), 97–110.

(3-5) Xie, L.; Wang, J.; Shi, C.; Huang, J.; Zhang, H.; Liu, Q.; Liu, Q.; Zeng, H. Probing Surface Interactions of Electrochemically Active Galena Mineral Surface Using Atomic Force Microscopy. *J. Phys. Chem. C* **2016**, *120* (39), 22433–22442.

(3-6) Rand, D. A. J. Oxygen Reduction on Sulphide Minerals: Part III. Comparison of Activities of Various Copper, Iron, Lead and Nickel Mineral Electrodes. *J. Electroanal. Chem. Interfacial Electrochem.* **1977**, *83* (1), 19–32.

(3-7) Allison, S.; Goold, L.; Granville, A. A Determination of the Products of Reaction Between Various Sulfide Minerals and Aqueous Xanthate Solution, and a Correlation of the Products with Electrode Rest Potentials. *Metall. Trans.* **1972**, *3* (10), 2613–2618.

(3-8) Friebel, D.; Louie, M. W.; Bajdich, M.; Sanwald, K. E.; Cai, Y.; Wise, A. M.; Cheng, M. J.; Sokaras, D.; Weng, T. C.; Alonso-Mori, R.; et al. Identification of Highly Active Fe Sites in (Ni,Fe)OOH for Electrocatalytic Water Splitting. *J. Am. Chem. Soc.* **2015**, *137* (3), 1305–1313.

(3-9) Seh, Z. W.; Kibsgaard, J.; Dickens, C. F.; Chorkendorff, I.; Nørskov, J. K.; Jaramillo, T. F. Combining Theory and Experiment in Electrocatalysis: Insights into Materials Design. *Science* **2017**, *355* (6321), 1–12.

(3-10) Nørskov, J. K.; Bligaard, T.; Rossmeisl, J.; Christensen, C. H. Towards the Computational Design of Solid Catalysts. *Nat. Chem.* **2009**, *1* (1), 37–46.

(3-11) Tritsaris, G. A.; Nørskov, J. K.; Rossmeisl, J. Trends in Oxygen Reduction and Methanol Activation on Transition Metal Chalcogenides. *Electrochim. Acta* **2011**, *56* (27), 9783–9788.

(3-12) Hammer, B.; Nørskov, J. K. Theoretical Surface Science and Catalysis – Calculations and Concepts. *Adv. Catal.* **2000**, *45*, 71–129.

(3-13) Nørskov, J. K.; Rossmeisl, J.; Logadottir, A.; Lindqvist, L.; Kitchin, J. R.; Bligaard, T.; Jónsson, H. Origin of the Overpotential for Oxygen Reduction at a Fuel-Cell Cathode. *J. Phys. Chem. B* **2004**, *108* (46), 17886–17892.

(3-14) Suntivich, J.; Gasteiger, H. A.; Yabuuchi, N.; Nakanishi, H.; Goodenough, J. B.; Shao-horn, Y. On Perovskite Oxide Catalysts for Fuel Cells and Metal–Air Batteries. *Nat. Chem.* **2011**, *3* (7), 546–550.

(3-15) Grimaud, A.; May, K. J.; Carlton, C. E.; Lee, Y.-L.; Risch, M.; Hong, W. T.; Zhou, J.; Shao-Horn, Y. Double Perovskites as a Family of Highly Active Catalysts for Oxygen

Evolution in Alkaline Solution. *Nat. Commun.* **2013**, *4*, 1–7.

(3-16) Lee, Y.-L.; Kleis, J.; Rossmeisl, J.; Shao-Horn, Y.; Morgan, D. Prediction of Solid Oxide Fuel Cell Cathode Activity with First-Principles Descriptors. *Energy Environ. Sci.* **2011**, *4* (10), 3966–3970.

(3-17) Blizanac, B. B.; Lucas, C. A.; Gallagher, M. E.; Arenz, M.; Ross, P. N.; Markovic, N. M. Anion Adsorption, CO Oxidation, and Oxygen Reduction Reaction on a Au(100) Surface: The PH Effect. *J. Phys. Chem. B* **2004**, *108* (2), 625–634.

(3-18) Hong, W. T.; Risch, M.; Stoerzinger, K. A.; Grimaud, A.; Suntivich, J.; Shao-Horn, Y. Toward the Rational Design of Non-Precious Transition Metal Oxides for Oxygen Electrocatalysis. *Energy Environ. Sci.* **2015**, *8* (5), 1404–1427.

(3-19) Nørskov, J. K.; Bligaard, T.; Logadottir, A.; Bahn, S.; Hansen, L. B.; Bollinger, M.; Bengaard, H.; Hammer, B.; Sljivancanin, Z.; Mavrikakis, M.; et al. Universality in Heterogeneous Catalysis. *J. Catal.* **2002**, *209* (2), 275–278.

(3-20) Stamenkovic, V.; Mun, B. S.; Mayrhofer, K. J. J.; Ross, P. N.; Markovic, N. M.; Rossmeisl, J.; Greeley, J.; Nørskov, J. K. Changing the Activity of Electrocatalysts for Oxygen Reduction by Tuning the Surface Electronic Structure. *Angew. Chemie Int. Ed.* **2006**, *45* (18), 2897–2901.

(3-21) Viswanathan, V.; Hansen, H. A.; Rossmeisl, J.; Nørskov, J. K. Universality in Oxygen Reduction Electrocatalysis on Metal Surfaces. *ACS Catal.* **2012**, *2* (8), 1654–1660.

(3-22) McCrum, I. T.; Hickner, M. A.; Janik, M. J. First-Principles Calculation of Pt Surface Energies in an Electrochemical Environment: Thermodynamic Driving Forces for Surface Faceting and Nanoparticle Reconstruction. *Langmuir* **2017**, *33* (28), 7043–7052.

(3-23) Andersson, K. J.; Ogasawara, H.; Nordlund, D.; Brown, G. E.; Nilsson, A. Preparation, Structure, and Orientation of Pyrite FeS$_2${100} Surfaces: Anisotropy, Sulfur Monomers, Dimer Vacancies, and a Possible Fes Surface Phase. *J. Phys. Chem. C* **2014**, *118* (38), 21896–21903.

(3-24) Chen, V. H. Y.; Mallia, G.; Martínez-Casado, R.; Harrison, N. M. Surface Morphology of CuFeS$_2$: The Stability of the Polar (112)/$(11\bar{2})$ Surface Pair. *Phys. Rev. B* **2015**, *92* (15), 1–9.

(3-25) Zherebetskyy, D.; Scheele, M.; Zhang, Y.; Bronstein, N.; Thompson, C.; Britt, D.; Salmeron, M.; Alivisatos, P.; Wang, L.-W. Hydroxylation of the Surface of PbS Nanocrystals Passivated with Oleic Acid. *Science* **2014**, *344* (6190), 1380–1384.

(3-26) Hamad, S.; Cristol, S.; Catlow, C. R. A. Surface Structures and Crystal Morphology of ZnS: Computational Study. *J. Phys. Chem. B* **2002**, *106* (42), 11002–11008.

(3-27) Alonso-Vante, N.; Malakho, I. V; Nikitenko, S. G.; Sa, E. R. The Structure Analysis of the Active Centers of Ru-Containing Electrocatalysts for the Oxygen Reduction. An in Situ EXAFS Study. *Electrochim. Acta* **2002**, *47* (22–23), 3807–3814.

(3-28) Karamad, M.; Hansen, H. A.; Rossmeisl, J.; Nørskov, J. K. Mechanistic Pathway in the Electrochemical Reduction of CO$_2$ on RuO$_2$. *ACS Catal.* **2015**, *5* (7), 4075–4081.

(3-29) Jacobsen, C. J. H.; Dahl, S.; Clausen, B. G. S.; Bahn, S.; Logadottir, A.; Nørskov, J. K. Catalyst Design by Interpolation in the Periodic Table: Bimetallic Ammonia Synthesis Catalysts. *J. Am. Chem. Soc.* **2001**, *123* (34), 8404–8405.

(3-30) Ahlberg, E.; Broo, A. E. Oxygen Reduction at Sulphide Minerals. 1. A Rotating Ring Disc Electrode (RRDE) Study at Galena and Pyrite. *Int. J. Miner. Process.* **1996**, *46* (1–2),

73–89.

(3-31) Siahrostami, S.; Li, G.-L.; Viswanathan, V.; Nørskov, J. K. One- or Two-Electron Water Oxidation, Hydroxyl Radical or $H_2O_2$ Evolution. *J. Phys. Chem. Lett.* **2017**, *8* (6), 1157–1160.

(3-32) Rosen, J.; Hutchings, G. S.; Lu, Q.; Rivera, S.; Zhou, Y.; Vlachos, D. G.; Jiao, F. Mechanistic Insights into the Electrochemical Reduction of $CO_2$ to CO on Nanostructured Ag Surfaces. *ACS Catal.* **2015**, *5* (7), 4293–4299.

(3-33) Man, I. C.; Su, H. Y.; Calle-Vallejo, F.; Hansen, H. A.; Martínez, J. I.; Inoglu, N. G.; Kitchin, J.; Jaramillo, T. F.; Nørskov, J. K.; Rossmeisl, J. Universality in Oxygen Evolution Electrocatalysis on Oxide Surfaces. *ChemCatChem* **2011**, *3* (7), 1159–1165.

(3-34) Kim, D.; Xie, C.; Becknell, N.; Yu, Y.; Karamad, M.; Chan, K.; Crumlin, E. J.; Nørskov, J. K.; Yang, P. Electrochemical Activation of $CO_2$ through Atomic Ordering Transformations of AuCu Nanoparticles. *J. Am. Chem. Soc.* **2017**, *139* (24), 8329–8336.

(3-35) Bajdich, M.; García-Mota, M.; Vojvodic, A.; Nørskov, J. K.; Bell, A. T. Theoretical Investigation of the Activity of Cobalt Oxides for the Electrochemical Oxidation of Water. *J. Am. Chem. Soc.* **2013**, *135* (36), 13521–13530.

(3-36) Stamenkovic, V.; Mun, B. S.; Mayrhofer, K. J. J.; Ross, P. N.; Markovic, N. M.; Rossmeisl, J.; Greeley, J.; Nørskov, J. K. Changing the Activity of Electrocatalysts for Oxygen Reduction by Tuning the Surface Electronic Structure. *Angew. Chemie Int. Ed.* **2006**, *45* (18), 2897–2901.

(3-37) Suntivich, J.; Gasteiger, H. A.; Yabuuchi, N.; Nakanishi, H.; Goodenough, J. B.; Shao-Horn, Y. Design Principles for Oxygen-Reduction Activity on Perovskite Oxide Catalysts for Fuel Cells and Metal-Air Batteries. *Nat. Chem.* **2011**, *3* (7), 546–550.

(3-38) Kim, C.; Jeon, H. S.; Eom, T.; Jee, M. S.; Kim, H.; Friend, C. M.; Min, B. K.; Hwang, Y. J. Achieving Selective and Efficient Electrocatalytic Activity for $CO_2$ Reduction Using Immobilized Silver Nanoparticles. *J. Am. Chem. Soc.* **2015**, *137* (43), 13844–13850.

(3-39) Zhang, J.; Vukmirovic, M. B.; Xu, Y.; Mavrikakis, M.; Adzic, R. R. Controlling the Catalytic Activity of Platinum-Monolayer Electrocatalysts for Oxygen Reduction with Different Substrates. *Angew. Chemie Int. Ed.* **2005**, *44* (14), 2132–2135.

(3-40) Nørskov, J. K. Electronic Factors in Catalysis. *Prog. Surf. Sci.* **1991**, *38* (2), 103–144.

(3-41) Hammer, B.; Nørskov, J. K. Why Gold Is the Noblest of All the Metals. *Nature* **1995**, *376* (6537), 238–240.

(3-42) Asadi, M.; Kim, K.; Liu, C.; Addepalli, A. V.; Abbasi, P.; Yasaei, P.; Phillips, P.; Behranginia, A.; Cerrato, J. M.; Haasch, R.; et al. Nanostructured Transition Metal Dichalcogenide Electrocatalysts for $CO_2$ Reduction in Ionic Liquid. *Science (80-. ).* **2016**, *353* (6298), 467–470.

(3-43) Bligaard, T.; Nørskov, J. K. *Chemical Bonding at Surfaces and Interfaces*; Elsevier B.V.: Oxford, 2008.

(3-44) Chen, J.; Li, Y.; Lan, L.; Guo, J. Interactions of Xanthate with Pyrite and Galena Surfaces in the Presence and Absence of Oxygen. *J. Ind. Eng. Chem.* **2014**, *20* (1), 268–273.

(3-45) Kulkarni, P.; Sanna Kotrappanavar, N.; Balakrishna, G. R.; Nagaraju, D. H.; Reddy, M. V. V. Nanostructured Binary and Ternary Metal Sulfides: Synthesis Methods and Its Application in Energy Conversion and Storage Devices. *J. Mater. Chem. A* **2017**, *5* (42),

22040–22094.

(3-46) Eftekhari, A. Tungsten Dichalcogenides ($WS_2$, $WSe_2$, and $WTe_2$): Materials Chemistry and Applications. *J. Mater. Chem. A* **2017**, *5* (35), 18299–18325.

(3-47) Shao, M.; Chang, Q.; Dodelet, J.-P.; Chenitz, R. Recent Advances in Electrocatalysts for Oxygen Reduction Reaction. *Chem. Rev.* **2016**, *116* (6), 3594–3657.

(3-48) Wang, F.; Shifa, T. A.; Zhan, X.; Huang, Y.; Liu, K.; Cheng, Z.; Jiang, C.; He, J. Recent Advances in Transition-Metal Dichalcogenide Based Nanomaterials for Water Splitting. *Nanoscale* **2015**, *7* (47), 19764–19788.

(3-49) Chen, Z.; Higgins, D.; Yu, A.; Zhang, L.; Zhang, J. A Review on Non-Precious Metal Electrocatalysts for PEM Fuel Cells. *Energy Environ. Sci.* **2011**, *4* (9), 3167–3192.

(3-50) Feng, Y.; Gago, A.; Timperman, L.; Alonso-vante, N. Electrochimica Acta Chalcogenide Metal Centers for Oxygen Reduction Reaction: Activity and Tolerance. *Electrochim. Acta* **2011**, *56* (3), 1009–1022.

(4-1) Chia, X.; Eng, A. Y. S.; Ambrosi, A.; Tan, S. M.; Pumera, M. Electrochemistry of Nanostructured Layered Transition-Metal Dichalcogenides. *Chem. Rev.* **2015**, *115* (21), 11941–11966.

(4-2) Asadi, M.; Kim, K.; Liu, C.; Addepalli, A. V.; Abbasi, P.; Yasaei, P.; Phillips, P.; Behranginia, A.; Cerrato, J. M.; Haasch, R.; et al. Nanostructured Transition Metal Dichalcogenide Electrocatalysts for $CO_2$ Reduction in Ionic Liquid. *Science* **2016**, *353* (6298), 467–470.

(4-3) Tao, H.; Liu, S.; Luo, J. L.; Choi, P.; Liu, Q.; Xu, Z. Descriptor of Catalytic Activity of

Metal Sulfides for Oxygen Reduction Reaction: A Potential Indicator for Mineral Flotation. *J. Mater. Chem. A* **2018**, *6* (20), 9650–9656.

(4-4) Gilbert, B.; Huang, F.; Lin, Z.; Goodell, C.; Zhang, H.; Banfield, J. F. Surface Chemistry Controls Crystallinity of ZnS Nanoparticles. *Nano Lett.* **2006**, *6* (4), 605–610.

(4-5) Tang, J.; Kemp, K. W.; Hoogland, S.; Jeong, K. S.; Liu, H.; Levina, L.; Furukawa, M.; Wang, X.; Debnath, R.; Cha, D.; et al. Colloidal-Quantum-Dot Photovoltaics Using Atomic-Ligand Passivation. *Nat. Mater.* **2011**, *10* (10), 765–771.

(4-6) Zherebetskyy, D.; Scheele, M.; Zhang, Y.; Bronstein, N.; Thompson, C.; Britt, D.; Salmeron, M.; Alivisatos, P.; Wang, L.-W. Hydroxylation of the Surface of PbS Nanocrystals Passivated with Oleic Acid. *Science* **2014**, *344* (6190), 1380–1384.

(4-7) Bealing, C. R.; Baumgardner, W. J.; Choi, J. J.; Hanrath, T.; Hennig, R. G. Predicting Nanocrystal Shape through Consideration of Surface-Ligand Interactions. *ACS Nano* **2012**, *6* (3), 2118–2127.

(4-8) Rotenberg, B.; Patel, A. J.; Chandler, D. Molecular Explanation for Why Talc Surfaces Can Be Both Hydrophilic and Hydrophobic. *J. Am. Chem. Soc.* **2011**, *133* (50), 20521–20527.

(4-9) Xie, L.; Wang, J.; Shi, C.; Cui, X.; Huang, J.; Zhang, H.; Liu, Q.; Liu, Q.; Zeng, H. Mapping the Nanoscale Heterogeneity of Surface Hydrophobicity on the Sphalerite Mineral. *J. Phys. Chem. C* **2017**, *121* (10), 5620–5628.

(4-10) Chu, X. S.; Yousaf, A.; Li, D. O.; Tang, A. A.; Debnath, A.; Ma, D.; Green, A. A.; Santos, E. J. G.; Wang, Q. H. Direct Covalent Chemical Functionalization of Unmodified

Two-Dimensional Molybdenum Disulfide. *Chem. Mater.* **2018**, *30* (6), 2112–2128.

(4-11) Rodríguez-Hermida, S.; Tsang, M. Y.; Vignatti, C.; Stylianou, K. C.; Guillerm, V.; Pérez-Carvajal, J.; Teixidor, F.; Viñas, C.; Choquesillo-Lazarte, D.; Verdugo-Escamilla, C. Switchable Surface Hydrophobicity–Hydrophilicity of a Metal–Organic Framework. *Angew. Chemie Int. Ed.* **2016**, *55* (52), 16049–16053.

(4-12) Comas, H.; Laporte, V.; Borcard, F.; Miéville, P.; Krauss Juillerat, F.; Caporini, M. A.; Gonzenbach, U. T.; Juillerat-Jeanneret, L.; Gerber-Lemaire, S. Surface Functionalization of Alumina Ceramic Foams with Organic Ligands. *ACS Appl. Mater. Interfaces* **2012**, *4* (2), 573–576.

(4-13) Xie, L.; Wang, J.; Shi, C.; Huang, J.; Zhang, H.; Liu, Q.; Liu, Q.; Zeng, H. Probing Surface Interactions of Electrochemically Active Galena Mineral Surface Using Atomic Force Microscopy. *J. Phys. Chem. C* **2016**, *120* (39), 22433–22442.

(4-14) Mu, Y.; Peng, Y.; Lauten, R. A. Electrochemistry Aspects of Pyrite in the Presence of Potassium Amyl Xanthate and a Lignosulfonate-Based Biopolymer Depressant. *Electrochim. Acta* **2015**, *174* (1), 133–142.

(4-15) Midya, L.; Patra, A. S.; Banerjee, C.; Panda, A. B.; Pal, S. Novel Nanocomposite Derived from ZnO/CdS QDs Embedded Crosslinked Chitosan: An Efficient Photocatalyst and Effective Antibacterial Agent. *J. Hazard. Mater.* **2019**, *369* (January), 398–407.

(4-16) Ng, W. S.; Forbes, E.; Franks, G. V.; Connal, L. A. Xanthate-Functional Temperature-Responsive Polymers: Effect on Lower Critical Solution Temperature Behavior and Affinity toward Sulfide Surfaces. *Langmuir* **2016**, *32* (30), 7443–7451.

(4-17) Moreels, I.; Fritzinger, B.; Martins, J. C.; Hens, Z. Surface Chemistry of Colloidal PbSe Nanocrystals. *J. Am. Chem. Soc.* **2008**, *130* (45), 15081–15086.

(4-18) Peterson, M. D.; Jensen, S. C.; Weinberg, D. J.; Weiss, E. A. Mechanisms for Adsorption of Methyl Viologen on Cds Quantum Dots. *ACS Nano* **2014**, *8* (3), 2826–2837.

(4-19) Larsson, M. L.; Holmgren, A.; Forsling, W. Xanthate Adsorbed on ZnS Studied by Polarized FTIR-ATR Spectroscopy. *Langmuir* **2000**, *16* (21), 8129–8133.

(4-20) Nørskov, J. K.; Bligaard, T.; Rossmeisl, J.; Christensen, C. H. Towards the Computational Design of Solid Catalysts. *Nat. Chem.* **2009**, *1* (1), 37–46.

(4-21) Maganas, D.; Neese, F.; Bistoni, G.; Ye, S.; Atanasov, M. Chemistry and Quantum Mechanics in 2019: Give Us Insight and Numbers. *J. Am. Chem. Soc.* **2019**, *141*(7), 2814–2824.

(4-22) Nørskov, J. K.; Bligaard, T.; Rossmeisl, J.; Christensen, C. H. Towards the Computational Design of Solid Catalysts. *Nat. Chem.* **2009**, *1* (1), 37–46.

(4-23) Nørskov, J. K.; Abild-Pedersen, F.; Studt, F.; Bligaard, T. Density Functional Theory in Surface Chemistry and Catalysis. *Proc. Natl. Acad. Sci.* **2011**, *108* (3), 937–943.

(4-24) Schumann, J.; Medford, A. J.; Yoo, J. S.; Zhao, Z.; Bothra, P. Selectivity of Synthesis Gas Conversion to $C_{2+}$ Oxygenates on Fcc(111) Transition-Metal Surfaces. *ACS Catal.* **2018**, *8* (4), 3447–3453.

(4-25) Medford, A. J.; Wellendorff, J.; Vojvodic, A.; Studt, F.; Abild-pedersen, F.; Jacobsen, K. W.; Bligaard, T. Assessing the Reliability of Calculated Catalytic Ammonia Synthesis Rates. *Science* **2014**, *345* (6193), 197–200.

(4-26) Kulkarni, A.; Siahrostami, S.; Patel, A.; Nørskov, J. K. Understanding Catalytic Activity Trends in the Oxygen Reduction Reaction. *Chem. Rev.* **2018**, *118* (5), 2302–2312.

(4-27) Hammer, B.; Nørskov, J. K. Electronic Factors Determining the Reactivity of Metal Surfaces. *Surf. Sci.* **1995**, *343* (3), 211–220.

(4-28) He, Y.; Fishman, Z. S.; Yang, K. R.; Ortiz, B.; Liu, C.; Goldsamt, J.; Batista, V. S.; Pfefferle, L. D. Hydrophobic CuO Nanosheets Functionalized with Organic Adsorbates. *J. Am. Chem. Soc.* **2018**, *140* (5), 1824–1833.

(4-29) Yin, Z.; Hu, Y.; Sun, W.; Zhang, C.; He, J.; Xu, Z.; Zou, J.; Guan, C.; Zhang, C.; Guan, Q.; et al. Adsorption Mechanism of 4-Amino-5-Mercapto-1,2,4-Triazole as Flotation Reagent on Chalcopyrite. *Langmuir* **2018**, *34* (13), 4071–4083.

(4-30) Waterson, C. N.; Tasker, P. A.; Farinato, R.; Nagaraj, D. R.; Shackleton, N.; Morrison, C. A. A Computational and Experimental Study on the Binding of Dithio Ligands to Sperrylite, Pentlandite, and Platinum. *J. Phys. Chem. C* **2016**, *120* (39), 22476–22488.

(4-31) Long, X.; Chen, Y.; Chen, J.; Xu, Z.; Liu, Q.; Du, Z. The Effect of Water Molecules on the Thiol Collector Interaction on the Galena (PbS) and Sphalerite (ZnS) Surfaces: A DFT Study. *Appl. Surf. Sci.* **2016**, *389*, 103–111.

(4-32) Kresse, G.; Hafner, J. Ab Initio Molecular Dynamics for Liquid Metals. *Phys. Rev. B* **1993**, *47* (1), 558–561.

(4-33) Kresse, G.; Hafner, J. Ab Initio Molecular-Dynamics Simulation of the Liquid-Metal–amorphous-Semiconductor Transition in Germanium. *Phys. Rev. B* **1994**, *49* (20), 14251–14269.

(4-34) Kresse, G.; Furthmüller, J. Efficiency of Ab-Initio Total Energy Calculations for Metals and Semiconductors Using a Plane-Wave Basis Set. *Comput. Mater. Sci.* **1996**, *6* (1), 15–50.

(4-35) Kresse, G.; Furthmüller, J. Efficient Iterative Schemes for Ab Initio Total-Energy Calculations Using a Plane-Wave Basis Set. *Phys. Rev. B* **1996**, *54* (16), 11169–11186.

(4-36) Blöchl, P. E. Projector Augmented-Wave Method. *Phys. Rev. B* **1994**, *50* (24), 17953–17979.

(4-37) Kresse, G. From Ultrasoft Pseudopotentials to the Projector Augmented-Wave Method. *Phys. Rev. B* **1999**, *59* (3), 1758–1775.

(4-38) Hammer, B.; Hansen, L. B.; Nørskov, J. K. Improved Adsorption Energetics within Density-Functional Theory Using Revised Perdew-Burke-Ernzerhof Functionals. *Phys. Rev. B* **1999**, *59* (11), 7413–7421.

(4-39) Monkhorst, H. J.; Pack, J. D. Special Points for Brillouin-Zone Integrations. *Phys. Rev. B* **1976**, *13* (12), 5188–5192.

(4-40) Mathew, K.; Sundararaman, R.; Letchworth-weaver, K.; Arias, T. A.; Hennig, R. G. Implicit Solvation Model for Density-Functional Study of Nanocrystal Surfaces and Reaction Pathways. *J. Chem. Phys.* **2014**, *140* (8), 084106.

(4-41) Fishman, M.; Zhuang, H. L.; Mathew, K.; Dirschka, W.; Hennig, R. G. Accuracy of Exchange-Correlation Functionals and Effect of Solvation on the Surface Energy of Copper. *Phys. Rev. B* **2013**, *87* (24), 245402.

(4-42) Kitchaev, D. A.; Ceder, G. Evaluating Structure Selection in the Hydrothermal Growth of

$FeS_2$ Pyrite and Marcasite. *Nat. Commun.* **2016**, *7*, 13799.

(4-43) Garza, A.; Bell, A. T.; Head-Gordon, M. Is Subsurface Oxygen Necessary for the Electrochemical Reduction of $CO_2$ on Copper? *J. Phys. Chem. Lett.* **2018**, *9* (3), 601–606.

(4-44) Chowdhry, M. Theoretical Study on Reactivity of Different Sulfide Collectors and Their Binding Affinity Toward Cu (II), Zn (II) and Pb (II) Ions, Ph.D dissertation, University of Alberta, Edmonton, AB, 2015.

(4-45) Gaussian 16, Revision B.01, Frisch, M. J.; Trucks, G. W.; Schlegel, H. B.; Scuseria, G. E.; Robb, M. A.; Cheeseman, J. R.; Scalmani, G.; Barone, V.; Petersson, G. A.; Nakatsuji, H.; Li, X.; Caricato, M.; Marenich, A. V.; Bloino, J.; Janesko, B. G.; Gomperts, R.; Mennucci, B.; Hratchian, H. P.; Ortiz, J. V.; Izmaylov, A. F.; Sonnenberg, J. L.; Williams-Young, D.; Ding, F.; Lipparini, F.; Egidi, F.; Goings, J.; Peng, B.; Petrone, A.; Henderson, T.; Ranasinghe, D.; Zakrzewski, V. G.; Gao, J.; Rega, N.; Zheng, G.; Liang, W.; Hada, M.; Ehara, M.; Toyota, K.; Fukuda, R.; Hasegawa, J.; Ishida, M.; Nakajima, T.; Honda, Y.; Kitao, O.; Nakai, H.; Vreven, T.; Throssell, K.; Montgomery, J. A., Jr.; Peralta, J. E.; Ogliaro, F.; Bearpark, M. J.; Heyd, J. J.; Brothers, E. N.; Kudin, K. N.; Staroverov, V. N.; Keith, T. A.; Kobayashi, R.; Normand, J.; Raghavachari, K.; Rendell, A. P.; Burant, J. C.; Iyengar, S. S.; Tomasi, J.; Cossi, M.; Millam, J. M.; Klene, M.; Adamo, C.; Cammi, R.; Ochterski, J. W.; Martin, R. L.; Morokuma, K.; Farkas, O.; Foresman, J. B.; Fox, D. J. Gaussian, Inc., Wallingford CT, 2016.

(4-46) Lee, Chengteh, Weitao Yang, and R. G. P. Development of the Colle-Salvetti Correlation-Energy Formula into a Functional of the Electron Density. *Phys. Rev. B* **1988**, *37* (2), 785–789.

(4-47) Rienstra-Kiracofe, J. C.; Tschumper, G. S.; Schaefer, H. F.; Nandi, S.; Ellison, G. B. Atomic and Molecular Electron Affinities: Photoelectron Experiments and Theoretical Computations. *Chem. Rev.* **2002**, *102* (1), 231–282.

(4-48) Thomas Heine, Jan-Ole Joswig, A. G. Computational Chemistry Workbook. *ChemPhysChem* **2011**, *12* (11), 2184.

(4-49) Downs, R. T.; Hall-Wallace, M. The American Mineralogist Crystal Structure Database. *Am. Mineral.* **2003**, *88* (1), 247–250.

(4-50) Becker, U.; Rosso, K. M. Step Edges on Galena(100): Probing the Basis for Defect Driven Surface Reactivity at the Atomic Scale. *Am. Mineral.* **2001**, *86* (7–8), 862–870.

(4-51) Vaughan, D. J. Chemical Bonding in Sulfide Minerals. *Rev. Mineral. Geochemistry* **2006**, *61* (1), 231–264.

(4-52) Mathew, K.; Sundararaman, R.; Letchworth-Weaver, K.; Arias, T. A.; Hennig, R. G. Implicit Solvation Model for Density-Functional Study of Nanocrystal Surfaces and Reaction Pathways. *J. Chem. Phys.* **2014**, *140* (8), 1–9.

(4-53) Rosso, K. M. Structure and Reactivity of Semiconducting Mineral Surfaces: Convergence of Molecular Modeling and Experiment. *Rev. Miner. Geochemistry* **2001**, *42* (1), 199–271.

(4-54) Grandke, T.; Ley, L.; Cardona, M. Angle-Resolved Uv Photoemission and Electronic Band Structures of the Lead Chalcogenides. *Phys. Rev. B* **1978**, *18* (8), 3847–3871.

(4-55) Li, R.; Bian, K.; Hanrath, T.; Bassett, W. A.; Wang, Z. Decoding the Superlattice and Interface Structure of Truncate PbS Nanocrystal-Assembled Supercrystal and Associated

Interaction Forces. *J. Am. Chem. Soc.* **2014**, *136* (34), 12047–12055.

(4-56) Gudmundsdóttir, S.; Tang, W.; Henkelman, G.; Jónsson, H.; Skúlason, E. Local Density of States Analysis Using Bader Decomposition for $N_2$ and $CO_2$ Adsorbed on Pt(110)-(1 × 2) Electrodes. *J. Chem. Phys.* **2012**, *137* (16), 164705.

(4-57) Evarestov, R. A. *Quantum Chemistry of Solids: The LCAO First Principles Treatment of Crystals.* Springer Science & Business Media*,* 2007.

(4-58) Yu, M.; Trinkle, D. R. Accurate and Efficient Algorithm for Bader Charge Integration. *J. Chem. Phys.* **2011**, *134* (6), 1–19.

(4-59) Wang, D. *Flotation Reagents: Applied Surface Chemistry on Minerals Flotation and Energy Resources Beneficiation*. Springer Singapore, 2016.

(4-60) Silvi, B.; Savin, A. Classification of Chemical Bonds Based on Topological Analysis of Electron Localization Functions. *Nature* **1994**, *371* (6499), 683-686.

(5-1) Shao, M.; Chang, Q.; Dodelet, J.-P.; Chenitz, R. Recent Advances in Electrocatalysts for Oxygen Reduction Reaction. *Chem. Rev.* **2016**, *116* (6), 3594–3657.

(5-2) Chen, Z.; Higgins, D.; Yu, A.; Zhang, L.; Zhang, J. A Review on Non-Precious Metal Electrocatalysts for PEM Fuel Cells. *Energy Environ. Sci.* **2011**, *4* (9), 3167–3192.

(5-3) Voiry, D.; Goswami, A.; Kappera, R.; Silva, C. D. C. C. E.; Kaplan, D.; Fujita, T.; Chen, M.; Asefa, T.; Chhowalla, M. Covalent Functionalization of Monolayered Transition Metal Dichalcogenides by Phase Engineering. *Nat. Chem.* **2015**, *7* (1), 45–49.

(5-4) Tao, H.; Liu, S.; Luo, J. L.; Choi, P.; Liu, Q.; Xu, Z. Descriptor of Catalytic Activity of

Metal Sulfides for Oxygen Reduction Reaction: A Potential Indicator for Mineral Flotation. *J. Mater. Chem. A* **2018**, *6* (20), 9650–9656.

(5-5) Falkowski, J. M.; Concannon, N. M.; Yan, B.; Surendranath, Y. Heazlewoodite, $Ni_3S_2$ : A Potent Catalyst for Oxygen Reduction to Water under Benign Conditions. *J. Am. Chem. Soc.* **2015**, *137* (25), 7978–7981.

(5-6) Staszak-Jirkovský, J.; Malliakas, C. D.; Lopes, P. P.; Danilovic, N.; Kota, S. S.; Chang, K.-C.; Genorio, B.; Strmcnik, D.; Stamenkovic, V. R.; Kanatzidis, M. G.; et al. Design of Active and Stable Co–Mo–Sx Chalcogels as PH-Universal Catalysts for the Hydrogen Evolution Reaction. *Nat. Mater.* **2015**, *15* (2), 197–203.

(5-7) Wang, D. Y.; Gong, M.; Chou, H. L.; Pan, C. J.; Chen, H. A.; Wu, Y.; Lin, M. C.; Guan, M.; Yang, J.; Chen, C. W.; et al. Highly Active and Stable Hybrid Catalyst of Cobalt-Doped $FeS_2$ Nanosheets-Carbon Nanotubes for Hydrogen Evolution Reaction. *J. Am. Chem. Soc.* **2015**, *137* (4), 1587–1592.

(5-8) Asadi, M.; Kim, K.; Liu, C.; Addepalli, A. V.; Abbasi, P.; Yasaei, P.; Phillips, P.; Behranginia, A.; Cerrato, J. M.; Haasch, R.; et al. Nanostructured Transition Metal Dichalcogenide Electrocatalysts for $CO_2$ Reduction in Ionic Liquid. *Science* **2016**, *353* (6298), 467–470.

(5-9) Liu, S.; Tao, H.; Liu, Q.; Xu, Z.; Liu, Q.; Luo, J.-L. Rational Design of Silver Sulfide Nanowires for Efficient $CO_2$ Electroreduction in Ionic Liquid. *ACS Catal.* **2018**, *8* (2), 1469–1475.

(5-10) Sarma, S. Das; Adam, S.; Hwang, E. H.; Rossi, E. Electronic Transport in Two

Dimensional Graphene. *Rev. Mod. Phys.* **2010**, *83* (2), 407–470.

(5-11) Vaughan, D. J. Sulfide Mineralogy and Geochemistry: Introduction and Overview. *Rev. Mineral. Geochemistry* **2006**, *61* (1), 1–5.

(5-12) Xie, L.; Wang, J.; Shi, C.; Cui, X.; Huang, J.; Zhang, H.; Liu, Q.; Liu, Q.; Zeng, H. Mapping the Nanoscale Heterogeneity of Surface Hydrophobicity on the Sphalerite Mineral. *J. Phys. Chem. C* **2017**, *121* (10), 5620–5628.

(5-13) Potapova, I.; Mruk, R.; Hübner, C.; Zentel, R.; Basché, T.; Mews, A. CdSe/ZnS Nanocrystals with Dye-Functionalized Polymer Ligands Containing Many Anchor Groups. *Angew. Chemie - Int. Ed.* **2005**, *44* (16), 2437–2440.

(5-14) Rodríguez-Hermida S, Tsang MY, Vignatti C, Stylianou KC, Guillerm V, Pérez-Carvajal J, Teixidor F, Viñas C, Choquesillo-Lazarte D, Verdugo-Escamilla C, P. I. Switchable Surface Hydrophobicity–Hydrophilicity of a Metal–Organic Framework. *Angew. Chemie - Int. Ed.* **2016**, *55* (52), 16049–16053.

(5-15) Lu, Z.; Chen, G.; Siahrostami, S.; Chen, Z.; Liu, K.; Xie, J.; Liao, L.; Wu, T.; Lin, D.; Liu, Y.; et al. High-Efficiency Oxygen Reduction to Hydrogen Peroxide Catalysed by Oxidized Carbon Materials. *Nat. Catal.* **2018**, *1* (2), 156–162.

(5-16) Schlücker, S. Surface-Enhanced Raman Spectroscopy: Concepts and Chemical Applications. *Angew. Chemie - Int. Ed.* **2014**, *53* (19), 4756–4795.

(5-17) Gilbert, B.; Huang, F.; Lin, Z.; Goodell, C.; Zhang, H.; Banfield, J. F. Surface Chemistry Controls Crystallinity of ZnS Nanoparticles. *Nano Lett.* **2006**, *6* (4), 605–610.

(5-18) Yang, H.; Li, F.; Shan, C.; Han, D.; Zhang, Q.; Niu, L.; Ivaska, A. Covalent

Functionalization of Chemically Converted Graphene Sheets via Silane and Its Reinforcement. *J. Mater. Chem.* **2009**, *19* (26), 4632–4638.

(5-19) Abild-pedersen, F.; Studt, F.; Bligaard, T. Density Functional Theory in Surface Chemistry and Catalysis. *Proc. Natl. Acad. Sci.* **2011**, *108* (3), 937–943.

(5-20) Nørskov, J. K.; Bligaard, T.; Rossmeisl, J.; Christensen, C. H. Towards the Computational Design of Solid Catalysts. *Nat. Chem.* **2009**, *1* (1), 37–46.

(5-21) He, Y.; Fishman, Z. S.; Yang, K. R.; Ortiz, B.; Liu, C.; Goldsamt, J.; Batista, V. S.; Pfefferle, L. D. Hydrophobic CuO Nanosheets Functionalized with Organic Adsorbates. *J. Am. Chem. Soc.* **2018**, *140* (5), 1824–1833.

(5-22) Bealing, C. R.; Baumgardner, W. J.; Choi, J. J.; Hanrath, T.; Hennig, R. G. Predicting Nanocrystal Shape through Consideration of Surface-Ligand Interactions. *ACS Nano* **2012**, *6* (3), 2118–2127.

(5-23) Zherebetskyy, D.; Scheele, M.; Zhang, Y.; Bronstein, N.; Thompson, C.; Britt, D.; Salmeron, M.; Alivisatos, P.; Wang, L.-W. Hydroxylation of the Surface of PbS Nanocrystals Passivated with Oleic Acid. *Science* **2014**, *344* (6190), 1380–1384.

(5-24) Long, X.; Chen, Y.; Chen, J.; Xu, Z.; Liu, Q.; Du, Z. The Effect of Water Molecules on the Thiol Collector Interaction on the Galena (PbS) and Sphalerite (ZnS) Surfaces: A DFT Study. *Appl. Surf. Sci.* **2016**, *389*, 103–111.

(5-25) Kresse, G.; Hafner, J. Ab Initio Molecular Dynamics for Liquid Metals. *Phys. Rev. B* **1993**, *47* (1), 558–561.

(5-26) Kresse, G.; Hafner, J. Ab Initio Molecular-Dynamics Simulation of the Liquid-Metal–

amorphous-Semiconductor Transition in Germanium. *Phys. Rev. B* **1994**, *49* (20), 14251–14269.

(5-27) Kresse, G.; Furthmüller, J. Efficiency of Ab-Initio Total Energy Calculations for Metals and Semiconductors Using a Plane-Wave Basis Set. *Comput. Mater. Sci.* **1996**, *6* (1), 15–50.

(5-28) Kresse, G.; Furthmüller, J. Efficient Iterative Schemes for Ab Initio Total-Energy Calculations Using a Plane-Wave Basis Set. *Phys. Rev. B* **1996**, *54* (16), 11169–11186.

(5-29) Blöchl, P. E. Projector Augmented-Wave Method. *Phys. Rev. B* **1994**, *50* (24), 17953–17979.

(5-30) Kresse, G. From Ultrasoft Pseudopotentials to the Projector Augmented-Wave Method. *Phys. Rev. B* **1999**, *59* (3), 1758–1775.

(5-31) Hammer, B.; Hansen, L. B.; Nørskov, J. K. Improved Adsorption Energetics within Density-Functional Theory Using Revised Perdew-Burke-Ernzerhof Functionals. *Phys. Rev. B* **1999**, *59* (11), 7413–7421.

(5-32) Monkhorst, H. J.; Pack, J. D. Special Points for Brillouin-Zone Integrations. *Phys. Rev. B* **1976**, *13* (12), 5188–5192.

(5-33) Downs, R. T.; Hall-Wallace, M. The American Mineralogist Crystal Structure Database. *Am. Mineral.* **2003**, *88* (1), 247–250.

(5-34) Liu, J.; Wen, S.; Deng, J.; Chen, X.; Feng, Q. DFT Study of Ethyl Xanthate Interaction with Sphalerite(110) Surface in the Absence and Presence of Copper. *Appl. Surf. Sci.* **2014**, *311*, 258–263.

(5-35) Balantseva, E.; Berlier, G.; Camino, B.; Lessio, M.; Ferrari, A. M. Surface Properties of ZnS Nanoparticles: A Combined DFT and Experimental Study. *J. Phys. Chem. C* **2014**, *118* (41), 23853–23862.

(5-36) Mathew, K.; Sundararaman, R.; Letchworth-weaver, K.; Arias, T. A.; Hennig, R. G. Implicit Solvation Model for Density-Functional Study of Nanocrystal Surfaces and Reaction Pathways. *J. Chem. Phys.* **2014**, *140* (8), 084106.

(5-37) Fishman, M.; Zhuang, H. L.; Mathew, K.; Dirschka, W.; Hennig, R. G. Accuracy of Exchange-Correlation Functionals and Effect of Solvation on the Surface Energy of Copper. *Phys. Rev. B* **2013**, *87* (24), 245402.

(5-38) Kitchaev, D. A.; Ceder, G. Evaluating Structure Selection in the Hydrothermal Growth of $FeS_2$ Pyrite and Marcasite. *Nat. Commun.* **2016**, *7*, 13799.

(5-39) Garza, A.; Bell, A. T.; Head-Gordon, M. Is Subsurface Oxygen Necessary for the Electrochemical Reduction of $CO_2$ on Copper? *J. Phys. Chem. Lett.* **2018**, *9* (3), 601–606.

(5-40) Gordon, W. O.; Xu, Y.; Mullins, D. R.; Overbury, S. H. Temperature Evolution of Structure and Bonding of Formic Acid and Formate on Fully Oxidized and Highly Reduced $CeO_2$(111). *Phys. Chem. Chem. Phys.* **2009**, *11* (47), 11171–11183.

(5-41) Chowdhry, M. Theoretical Study on Reactivity of Different Sulfide Collectors and Their Binding Affinity Toward Cu (II), Zn (II) and Pb (II) Ions, Ph.D dissertation, University of Alberta, Edmonton, AB, 2015.

(5-42) Vaughan, D. J. Chemical Bonding in Sulfide Minerals. *Rev. Mineral. Geochemistry* **2006**, *61* (1), 231–264.

(5-43) Long, X.; Chen, J.; Chen, Y. Adsorption of Ethyl Xanthate on ZnS(110) Surface in the Presence of Water Molecules: A DFT Study. *Appl. Surf. Sci.* **2016**, *370*, 11–18.

(5-44) Porento, M.; Hirva, P. Effect of Copper Atoms on the Adsorption of Ethyl Xanthate on a Sphalerite Surface. *Surf. Sci.* **2005**, *576* (1–3), 98–106.

(5-45) Larsson, M. L.; Holmgren, A.; Forsling, W. Xanthate Adsorbed on ZnS Studied by Polarized FTIR-ATR Spectroscopy. *Langmuir* **2000**, *16* (21), 8129–8133.

(5-46) Gudmundsdóttir, S.; Tang, W.; Henkelman, G.; Jónsson, H.; Skúlason, E. Local Density of States Analysis Using Bader Decomposition for $N_2$ and $CO_2$ Adsorbed on Pt(110)-(1 × 2) Electrodes. *J. Chem. Phys.* **2012**, *137* (16), 164705.

(5-47) Zheng, C.; Apeloig, Y.; Hoffmann, R. Bonding and Coupling of C1 Fragments on Metal Surfaces. *J. Am. Chem. Soc.* **1988**, *110* (3), 749–774.

(5-48) Evarestov, R. A. *Quantum Chemistry of Solids: The LCAO First Principles Treatment of Crystals. Springer Science & Business Media,* 2007.

(5-49) Mondal, B.; Bag, R.; Ghorai, S.; Bakthavachalam, K.; Jemmis, E. D.; Ghosh, S. Synthesis, Structure, Bonding, and Reactivity of Metal Complexes Comprising Diborane(4) and Diborene(2): $[\{Cp^*Mo(CO)_2\}_2\{\mu\text{-}\eta^2\text{:}\eta^2\text{-}B_2H_4\}]$ and $[\{Cp^*M(CO)_2\}_2B_2H_2M(CO)_4]$, M=Mo,W. *Angew. Chemie - Int. Ed.* **2018**, *57* (27), 8079–8083.

(5-50) Hollerer, M.; Lüftner, D.; Hurdax, P.; Ules, T.; Soubatch, S.; Tautz, F. S.; Koller, G.; Puschnig, P.; Sterrer, M.; Ramsey, M. G. Charge Transfer and Orbital Level Alignment at Inorganic/Organic Interfaces: The Role of Dielectric Interlayers. *ACS Nano* **2017**, *11* (6),

6252–6260.

(5-51) Yu, M.; Trinkle, D. R. Accurate and Efficient Algorithm for Bader Charge Integration. *J. Chem. Phys.* **2011**, *134* (6), 1–19.

(5-52) Bassett, C. A. L.; Herrmann, I. A Quantitative Theory of the Character of Chemical Bonding in Binary Compounds. *Nature* **1961**, *192* (4798), 133–135.

(5-53) Ormeci, A.; Simon, A.; Grin, Y. Structural Topology and Chemical Bonding in Laves Phases. *Angew. Chemie - Int. Ed.* **2010**, *49* (47), 8997–9001.

(5-54) Silvi, B.; Savin, A. Classification of Chemical Bonds Based on Topological Analysis of Electron Localization Functions. *Nature* **1994**, *371(6499)*, 683-686.

(5-55) Tsuji, Y.; Dasari, P. L. V. K.; Elatresh, S. F.; Hoffmann, R.; Ashcroft, N. W. Structural Diversity and Electron Confinement in Li4N: Potential for 0-D, 2-D, and 3-D Electrides. *J. Am. Chem. Soc.* **2016**, *138* (42), 14108–14120.

(5-56) Shayeghi, A.; Johnston, R. L.; Rayner, D. M.; Schäfer, R.; Fielicke, A. The Nature of Bonding between Argon and Mixed Gold-Silver Trimers. *Angew. Chemie - Int. Ed.* **2015**, *54* (36), 10675–10680.

(5-57) Wang, D. *Flotation Reagents: Applied Surface Chemistry on Minerals Flotation and Energy Resources Beneficiation*; Springer Singapore, 2016.

# Appendix A Supporting Information for Chapter 3

## A.1 DFT Calculations

The Vienna *ab initio* Simulation Package (VASP)[1–4] with the projector augmented wave method[5,6] was performed for the first-principles calculations in this study. The electron wavefunctions were presented by the planewave basis set and the cutoff energy for plane-wave basis functions was set at 450 eV. For all calculations, the spin polarization was enabled. For adsorption models of the oxygen reduction reaction (ORR) intermediates over the representative metal sulfides (i.e., Pt, $FeS_2$, $CuFeS_2$, PbS, ZnS), the revised Perdew-Burke-Ernzerhof generalized gradient approximation (GGA) functional[7] was adopted to describe the exchange and correlation interactions. The occupancy of the one-electron states was calculated using an electronic temperature of $k_BT = 0.05$ eV for surfaces and 0.01 eV for molecules in vacuum. All energies were extrapolated to T = 0 K. The slab models of Pt(111), $FeS_2(100)$, $CuFeS_2(112)$, PbS(100) and ZnS(110) comprising four, nine, six, six and six atomic layers, respectively, and the vacuum layer with thickness of 20 Å. The cleavage planes of (111), (100), (112), (100) and (110) were adopted for Pt,[8,9] $FeS_2$,[10] $CuFeS_2$,[11] PbS[12] and ZnS,[13] respectively, because they have been considered as stable and easily exposed planes, which have been extensively used as the model surfaces. We subsequently built the relevant ORR models with the metallic cations on the surface as the active center, attempting to understand the distinct activities of these materials for ORR. Meanwhile, the surface models were built with similar side lengths and contain eight metallic sites on the surface to guarantee the intermediate coverage of 1/8 ML. During the geometry optimization of the slab models, half of the bottom atomic layers were constraint, while other layers were relaxed. The structures were geometrically optimized until the force components were less than 0.05 eV/Å. The similar density of Monkhorst-Pack *k*-point grids[14] (i.e., 7 × 7 × 7 for unit cell of galena) was set to sample the Brillouin zone for all the surface models, while only the Gamma point was included for molecules.

Given that metal sulfides present different crystal structures and contain various metallic cations, different GGA functionals were tested for full optimization of the unit cells before calculating the bulk descriptor (i.e., the bulk centroid of the occupied S 3p band relative to the Fermi level). The experimental lattice constants and the lattice constants calculated with different GGA functionals are listed in Table A.1. It shows that DFT calculations with the GGA_PBE functional reproduced experimental crystal structures better than the results obtained with other GGA functionals. However, even crystal structures optimized with the GGA_PBE functional present various levels of discrepancies. Therefore, we calculated the electronic structures for internally optimized crystals using the GGA_PBE functional, as enlightened by previous research on perovskite.[15] Moreover, the surface descriptors were also calculated for metal sulfides possessing ideal cleavage planes. The surface models were built directly with the internally optimized structures of the unit cells and then optimized in the same way as that for the ORR models. The descriptor was calculated for sulfur anions on the first layer of the surface and was shown in Figure 3.3(c). The descriptor was determined by taking the centroid of the occupied projected density of states of the sulfur p states or metal d states relative to the Fermi level using the commonly used formula,[16–19]

$$band\ center = \frac{\int E \cdot f(E) dE}{\int f(E) dE} \qquad \text{A-1}$$

where $E$ is the electron energy, $f(E)$ is the corresponding PDOS value.

Regarding the chemisorption of the atomic oxygen, we also calculated the oxygen binding strength on the typical sulfur site on the surface. The calculated oxygen chemisorption energy on the sulfur sites is compared with that on the metallic cation sites in Figure A.1.

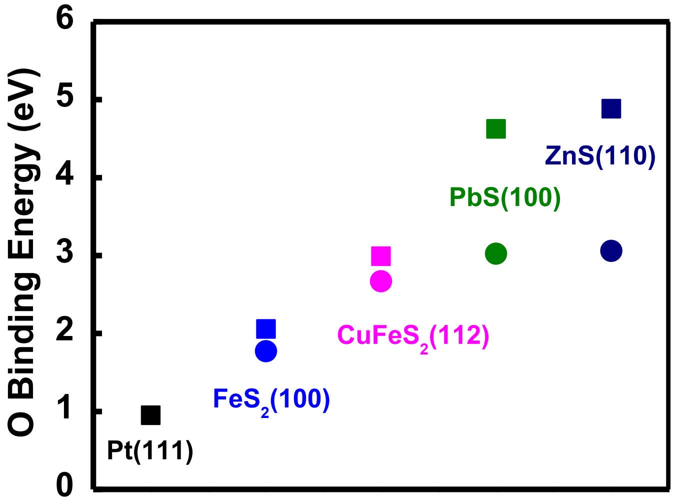

**Figure A.1** The DFT calculated oxygen binding energy on metal sites (Square) and sulfur sites (Circle).

In Figure S1, smaller values of the O binding energy indicate stronger chemisorption of oxygen on the surface. The relative oxygen chemisorption energies reflect the different levels of competitive adsorption of oxygen on the sulfur sites with that of the metal sites on the surface. It is noteworthy that oxygen binds much more strongly on the sulfur sites than that on the metal sites on the PbS and ZnS surfaces, which exhibit very poor catalytic activities for the ORR. The substantially stronger tendency of the adsorption of oxygen on the sulfur sites on surface of PbS and ZnS, as compared to those of $FeS_2$ and $CuFeS_2$, further highlights the dominating role of the metallic cations on the catalytic activity of metal sulfides for the ORR. Moreover, the consideration of choosing metallic cation as the active centers to build ORR models is based on previous experimental and theoretical studies.[15,20–27] Therefore, we believe that the selection of metallic cations as the active center to study the activity of metal sulfides for the ORR is reasonable and persuasive, as also supported by the established descriptor–activity relationship in our work.

In our study, we calculated both the occupied bulk metal d-band center and the bulk S p-band center. The correlation between the rest potential and the bulk d-band center is shown in Figure A.2. As seen, the experimental rest potential exhibits a much better correlation with the bulk S p-band center with a coefficient of determination (i.e., $R^2$) of 0.88 as compared to that with the bulk d-band center ($R^2$=0.71). Therefore, the sulfur p-band center was selected to the build the descriptor–activity relationship.

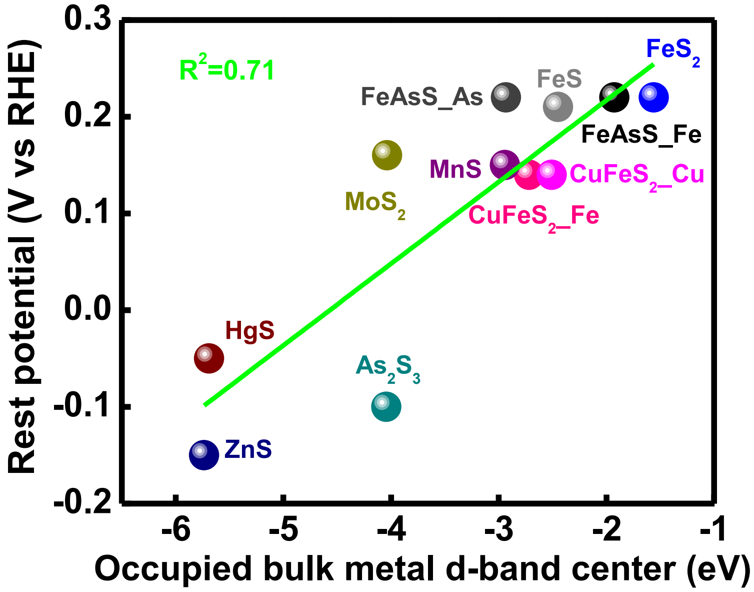

**Figure A.2** The experimental rest potentials plotted against the occupied bulk metal d-band center relative to the Fermi energy. The d-band center of galena is −16.84 which is not included in this plot.

### A.2 Gibbs free energy diagram

Gibbs free energy diagram for ORR was constructed through thermodynamically corrected DFT calculation results in combination with the computational hydrogen electrode (CHE) model where each electrochemical reaction step is treated as a simultaneous transfer of the proton-electron pair as a function of the applied potential.[7,28] The associative model was adopted for the ORR,[25]

$$\begin{gathered} 4H^+ + 4e + O_2 + * \\ \downarrow \\ 3H^+ + 3e + OOH/* \\ \downarrow \\ 2H^+ + 2e + H_2O + O/* \\ \downarrow \\ H^+ + e + H_2O + OH/* \\ \downarrow \\ 2H_2O + * \end{gathered}$$

where * indicates the underlying surface. Using the final state where two gaseous water molecules freely above an empty surface as the reference, the Gibbs free energies of each elementary step were represented as,

$$G[0] = G[O_2] + 4G[H^+ + e^-] + G[*] - (G[*] + 2G[H_2O]) \tag{A-2}$$

$$G[1] = G[OOH^*] + 3G[H^+ + e^-] - (G[*] + 2G[H_2O]) \tag{A-3}$$

$$G[2] = G[O^*] + 2G[H^+ + e^-] - (G[*] + G[H_2O]) \tag{A-4}$$

$$G[3] = G[OH^*] + G[H^+ + e^-] - (G[*] + G[H_2O]) \tag{A-5}$$

$$G[5] = 0 \tag{A-6}$$

The free energies for relevant species were then calculated with the expression,

$$G = E_{DFT} + E_{ZPE} + \int C_p dT - TS + E_w \quad \text{A-7}$$

where $E_{DFT}$ is the DFT calculated electronic energy with VASP; $E_{ZPE}$ is the zero-point vibrational energy; $\int C_p dT$ is the enthalpy correction; $TS$ is the entropy contribution and $E_w$ is the stabilization of water molecules on the adsorbed intermediates which were obtained from the previous researches on platinum and metal sulfides for ORR.[9,29,30] In their studies, ice-like water bilayer structure on the surface was constructed, where half of the water molecules are $* H_2O$ and the other half have an O–H bond pointing down, as proposed by H. Ogasawara et al. and S. Maier et al.[31,32]

## A.3 Thermodynamic corrections

To construct the Gibbs free energy diagram, the DFT calculated electronic energies were corrected with contributions to thermodynamic quantities from translational, electronic, rotational and vibrational motions. The contributions to entropy and enthalpy from different components were calculated with the standard methods.[33] The basic ideas and equations used for relevant calculations will be briefly introduced in this section, more details can go to the reference. For non-adsorbed molecules, the standard ideal gas methods were employed, where the contributions to enthalpy and entropy are calculated as,[33,34]

$$H(T) = E_{DFT} + E_{ZPE} + \int_0^{298.15} C_p dT \quad \text{A-8}$$

$$C_p = C_{V,trans} + C_{V,rot} + C_{V,vib} + C_{V,elec} + k_B \quad \text{A-9}$$

$$S(T,P) = S(T,P^0) - k_B ln\frac{P}{P^0} = S_{trans} + S_{rot} + S_{elec} + S_{vib} + k_B ln\frac{P}{P^0} \quad \text{A-10}$$

Where $H(T)$ is the ideal-gas enthalpy; $C_p$ is the constant-pressure heat capacity; $C_V$ is the constant-volume heat capacity which is separated into translational ($C_{V,trans}$), rotational ($C_{V,rot}$), vibrational ($C_{V,vib}$) and electronic ($C_{V,elec}$) parts. The translational heat capacity is $1.5k_B$ for a three-dimensional gas; the rotational heat capacity is $k_B$ for linear molecule and $1.5k_B$ for nonlinear molecule; the electronic heat capacity is assumed to be 0. $S(T,P)$is the ideal-gas entropy comprising contributions from the four components. The equations for the integrated vibrational heat capacity and different contributions to the entropy are expressed as,

$$\int_0^T C_{V,vib} dT = \sum_i^{\mathrm{DOF}} \frac{hw_i}{e^{hw_i/k_BT}-1} \tag{A-11}$$

$$S_{trans} = k_B\{ln[(\frac{2\pi M k_B T}{h^2})^{3/2} \frac{k_BT}{P^0}] + \frac{5}{2}\} \tag{A-12}$$

$$S_{rot} = k_B\{\ln\left[\frac{\sqrt{\pi I_A I_B I_C}}{\sigma}\left(\frac{8\pi^2 k_B T}{h^2}\right)^{\frac{3}{2}}\right] + \frac{3}{2}\} \quad \text{for non-linear molecule} \tag{A-13}$$

$$= k_B\left[ln\left(\frac{8\pi^2 I k_B T}{\sigma h^2}\right) + 1\right] \quad \text{for linear molecule} \tag{A-14}$$

$$S_{vib} = k_B \sum_i^{\mathrm{DOF}}[\frac{hw_i}{k_BT(e^{hw_i/k_BT}-1)} - \ln(1 - e^{-\frac{hw_i}{k_BT}})] \tag{A-15}$$

$$S_{elec} = k_B \ln[2S+1] \tag{A-16}$$

Where $M$ is the molecular weight, $w_i$ is the vibrational frequency, $h$ is the Planck constant, $k_B$ is the Boltzmann constant, $I$ is the moment inertia, $\sigma$ is the symmetry number of the molecule, $S$ is the spin multiplicity, $DOF$ indicates the degree of freedom which is $3N-5$ for linear molecule and $3N-6$ for non-linear molecule, $N$ is the number of atoms in the molecule.

For adsorbed molecules on the surface, the harmonic limit method was adopted. Within this scheme, the harmonic approximation where all $3N$ degrees of freedom were treated as frustrated harmonic vibrations was used to treat the adsorbates, with negligible contributions from the underlying surfaces, and the $PV$ contributions were neglected. Thus, the enthalpy and entropy of the adsorbate are calculated as,

$$H(T) = E_{DFT} + E_{ZPE} + \sum_i^{3N} \frac{hw_i}{e^{hw_i/k_BT}-1} \tag{A-17}$$

$$S(T) = S_{vib} = k_B \sum_i^{3N} [\frac{hw_i}{k_BT(e^{hw_i/k_BT}-1)} - ln(1 - e^{-\frac{hw_i}{k_BT}})] \tag{A-18}$$

The entropy of $H_2O$ is calculated at 0.035 bar, corresponding to the equilibrium pressure of $H_2O$ at room temperature, and the free energy of this state is therefore equal to that of liquid water. Furthermore, within the CHE model,[9] the free energy of the proton-electron pair is related to that of the gaseous hydrogen molecule under standard conditions,

$$G[H^+(aq) + e^-] = G\left[{}^1/_2\, H_2(g)\right] \tag{A-19}$$

Since $pH$ in the practical electrochemical system is not 0, the reversible hydrogen electrode (RHE) is adopted. The difference between the SHE and RHE scales corresponds to the free energy difference of going from $pH = 0$ to a different $pH$, where the free energy of hydrogen ion is corrected with $G(pH) = k_BTln(a_{H^+}) = -k_BT(ln10)pH$. Considering that the free energy trend of different elementary steps is not affected by the $pH$ value, and the experimental catalytic activity trend for ORR of the representative materials remains the same in both acidic and alkaline conditions,[35] for simplicity, the $pH$ value was set as 0. At a different electrode potential $U$, the Gibbs free energy for all states are shifted down by $-eU$. The effect of the external potential on the adsorbed intermediate was neglected due to the relatively small corrections as shown by previous research.[9,29] The chemical potential of the proton-electron pair can thus be expressed as,

$$G[H^+(aq)] + e^-] = G[{}^1/_2\, H_2(g)]) - eU \qquad \text{A-20}$$

The atomic oxygen binding energy ($\Delta E_O$) was calculated as the reaction energy,[25]

$$\Delta E_O = E_{surface/O} + \ E_{H_2} - E_{surface} - E_{H_2O} \qquad \text{A-21}$$

where $E_{surface/O}$and $E_{surface}$ are the DFT calculated electronic energies of the slab with and without adsorbed $O$, respectively. $E_{H_2O}$ and $E_{H_2}$ are the gas phase energies of water and hydrogen molecule, respectively. All the relevant thermodynamic data calculated for construction of the Gibbs free energy diagrams is listed in Table A.2.

**Table A.1** Experimental crystal structures of sulfide minerals[36] and the DFT optimized crystal structures with different GGA functionals implemented in VASP.

| **Sulfides** | **Experimental (Å)** | | | **Functional** | **Optimized (Å)** | | | **Δ (%)** | | |
|---|---|---|---|---|---|---|---|---|---|---|
| | **a** | **b** | **c** | | **a** | **b** | **c** | **a** | **b** | **c** |
| Alabandite<br>$Mn_4S_4$ | 5.225 | 5.225 | 5.225 | PW91 | 5.117 | 5.117 | 5.117 | -2.051 | -2.051 | -2.051 |
| | | | | PBE | 5.126 | 5.126 | 5.126 | -1.880 | -1.880 | -1.880 |
| | | | | PBEsol | 5.117 | 5.117 | 5.117 | -2.051 | -2.051 | -2.051 |
| | | | | RPBE | 5.090 | 5.090 | 5.090 | -2.569 | -2.569 | -2.569 |
| Arsenopyrite<br>$Fe_4As_4S_4$ | 5.744 | 5.675 | 5.785 | PW91 | 5.749 | 5.673 | 5.765 | 0.084 | -0.027 | -0.342 |
| | | | | PBE | 5.742 | 5.671 | 5.761 | -0.028 | -0.075 | -0.413 |
| | | | | PBEsol | 5.663 | 5.595 | 5.687 | -1.409 | -1.411 | -1.690 |
| | | | | RPBE | 5.765 | 5.693 | 5.783 | 0.366 | 0.309 | -0.034 |
| Chalcopyrite<br>$Cu_4Fe_4S_8$ | 5.290 | 5.290 | 10.422 | PW91 | 5.276 | 5.276 | 10.179 | -0.267 | -0.267 | -2.330 |
| | | | | PBE | 5.288 | 5.288 | 10.296 | -0.041 | -0.041 | -1.208 |
| | | | | PBEsol | 5.048 | 5.048 | 9.930 | -4.573 | -4.573 | -4.715 |
| | | | | RPBE | 5.358 | 5.358 | 10.576 | 1.286 | 1.286 | 1.476 |
| Cinnabar<br>$Hg_3S_3$ | 4.150 | 4.150 | 9.510 | PW91 | 3.952 | 3.952 | 9.669 | -4.759 | -4.759 | 1.670 |
| | | | | PBE | 3.948 | 3.948 | 9.668 | -4.873 | -4.873 | 1.662 |
| | | | | PBEsol | 3.867 | 3.867 | 9.471 | -6.823 | -6.823 | -0.405 |
| | | | | RPBE | 3.999 | 3.999 | 9.764 | -3.644 | -3.644 | 2.673 |
| Galena<br>$Pb_4S_4$ | 5.936 | 5.936 | 5.936 | PW91 | 6.005 | 6.005 | 6.005 | 1.166 | 1.166 | 1.166 |
| | | | | PBE | 6.008 | 6.008 | 6.008 | 1.207 | 1.207 | 1.207 |
| | | | | PBEsol | 5.900 | 5.900 | 5.900 | -0.603 | -0.603 | -0.603 |
| | | | | RPBE | 6.072 | 6.072 | 6.072 | 2.280 | 2.280 | 2.280 |
| Molybdenite<br>$Mo_2S_4$ | 3.161 | 3.161 | 12.295 | PW91 | 3.197 | 3.197 | 14.044 | 1.133 | 1.133 | 14.228 |
| | | | | PBE | 3.190 | 3.190 | 14.389 | 0.910 | 0.910 | 17.032 |
| | | | | PBEsol | 3.147 | 3.147 | 12.566 | -0.444 | -0.444 | 2.208 |
| | | | | RPBE | 3.208 | 3.208 | 14.690 | 1.478 | 1.478 | 19.476 |

| | | | | | | | | | | |
|---|---|---|---|---|---|---|---|---|---|---|
| Orpiment | 11.475 | 9.577 | 4.256 | PW91 | 11.426 | 10.875 | 4.557 | -0.431 | 13.554 | 7.077 |
| $As_2S_3$ | | | | PBE | 11.414 | 10.975 | 4.578 | -0.531 | 14.600 | 7.575 |
| | | | | PBEsol | 11.507 | 9.500 | 4.049 | 0.281 | -0.804 | -4.870 |
| | | | | RPBE | 11.459 | 12.029 | 5.013 | -0.142 | 25.608 | 17.776 |
| Pyrite | 5.417 | 5.417 | 5.417 | PW91 | 5.415 | 5.415 | 5.415 | -0.039 | -0.039 | -0.039 |
| $Fe_4S_8$ | | | | PBE | 5.408 | 5.408 | 5.408 | -0.167 | -0.167 | -0.167 |
| | | | | PBEsol | 5.329 | 5.329 | 5.329 | -1.616 | -1.616 | -1.616 |
| | | | | RPBE | 5.440 | 5.440 | 5.440 | 0.427 | 0.427 | 0.427 |
| Sphalerite | 5.409 | 5.409 | 5.409 | PW91 | 5.451 | 5.451 | 5.451 | 0.779 | 0.779 | 0.779 |
| $Zn_4S_4$ | | | | PBE | 5.448 | 5.448 | 5.448 | 0.715 | 0.715 | 0.715 |
| | | | | PBEsol | 5.367 | 5.367 | 5.367 | -0.777 | -0.777 | -0.777 |
| | | | | RPBE | 5.538 | 5.538 | 5.538 | 2.374 | 2.374 | 2.374 |
| Stibnite | 11.282 | 3.830 | 11.225 | PW91 | 11.916 | 3.876 | 11.281 | 5.621 | 1.218 | 0.501 |
| $Sb_2S_3$ | | | | PBE | 12.098 | 3.872 | 11.252 | 7.234 | 1.111 | 0.237 |
| | | | | PBEsol | 11.278 | 3.829 | 10.909 | -0.036 | -0.014 | -2.814 |
| | | | | RPBE | 13.969 | 3.882 | 11.860 | 23.818 | 1.372 | 5.660 |
| Troilite | 5.965 | 5.965 | 11.757 | PW91 | 5.843 | 5.843 | 10.452 | -2.053 | -2.053 | -11.099 |
| $Fe_{12}S_{12}$ | | | | PBE | 5.835 | 5.835 | 10.433 | -2.173 | -2.173 | -11.264 |
| | | | | PBEsol | 5.711 | 5.711 | 10.304 | -4.251 | -4.251 | -12.356 |
| | | | | RPBE | 5.944 | 5.944 | 10.848 | -0.354 | -0.354 | -7.731 |

**Table A.2** Thermodynamic corrections for molecules and ORR intermediates adsorbed on Pt(111), $FeS_2$(100), PbS(100), ZnS(110), $CuFeS_2$(112)_Fe and $CuFeS_2$(112)_Cu.

| **Species/Adsorbate** | **Pressure (Pa)** | **$E_{ZPE}$ (eV)** | **$\int C_p dT$ (eV)** | **− TS (eV)** | **G − $E_{DFT}$ (eV)** |
|---|---|---|---|---|---|
| $H_2$ | 101325 | 0.279 | 0.090 | -0.462 | -0.093 |
| $H_2O$ | 3500 | 0.566 | 0.104 | -0.673 | -0.003 |
| $O_2$ | 101325 | 0.101 | 0.123 | -0.563 | -0.339 |
| Pt111 | | | | | 0.000 |
| *O | | 0.067 | 0.034 | -0.061 | 0.040 |
| *OH | | 0.356 | 0.048 | -0.084 | 0.320 |
| *OOH | | 0.426 | 0.100 | -0.229 | 0.297 |
| Pyrite100 | | | | | 0.000 |
| *O | | 0.067 | 0.034 | -0.061 | 0.040 |
| *OH | | 0.348 | 0.054 | -0.095 | 0.307 |
| *OOH | | 0.403 | 0.109 | -0.225 | 0.287 |
| Galena100 | | | | | 0.000 |
| *O | | 0.033 | 0.051 | -0.109 | -0.025 |
| *OH | | 0.322 | 0.067 | -0.134 | 0.255 |
| *OOH | | 0.410 | 0.113 | -0.254 | 0.269 |
| Sphalerite110 | | | | | 0.000 |
| *O | | 0.032 | 0.053 | -0.129 | -0.044 |
| *OH | | 0.323 | 0.068 | -0.143 | 0.248 |
| *OOH | | 0.417 | 0.097 | -0.217 | 0.297 |
| Chalcopyrite112_Fe | | | | | 0.000 |
| *O | | 0.038 | 0.051 | -0.151 | -0.061 |
| *OH | | 0.329 | 0.068 | -0.162 | 0.235 |
| *OOH | | 0.429 | 0.100 | -0.206 | 0.323 |
| Chalcopyrite112_Cu | | | | | 0.000 |
| *O | | 0.057 | 0.044 | -0.101 | 0.000 |
| *OH | | 0.334 | 0.062 | -0.137 | 0.259 |
| *OOH | | 0.423 | 0.106 | -0.295 | 0.234 |

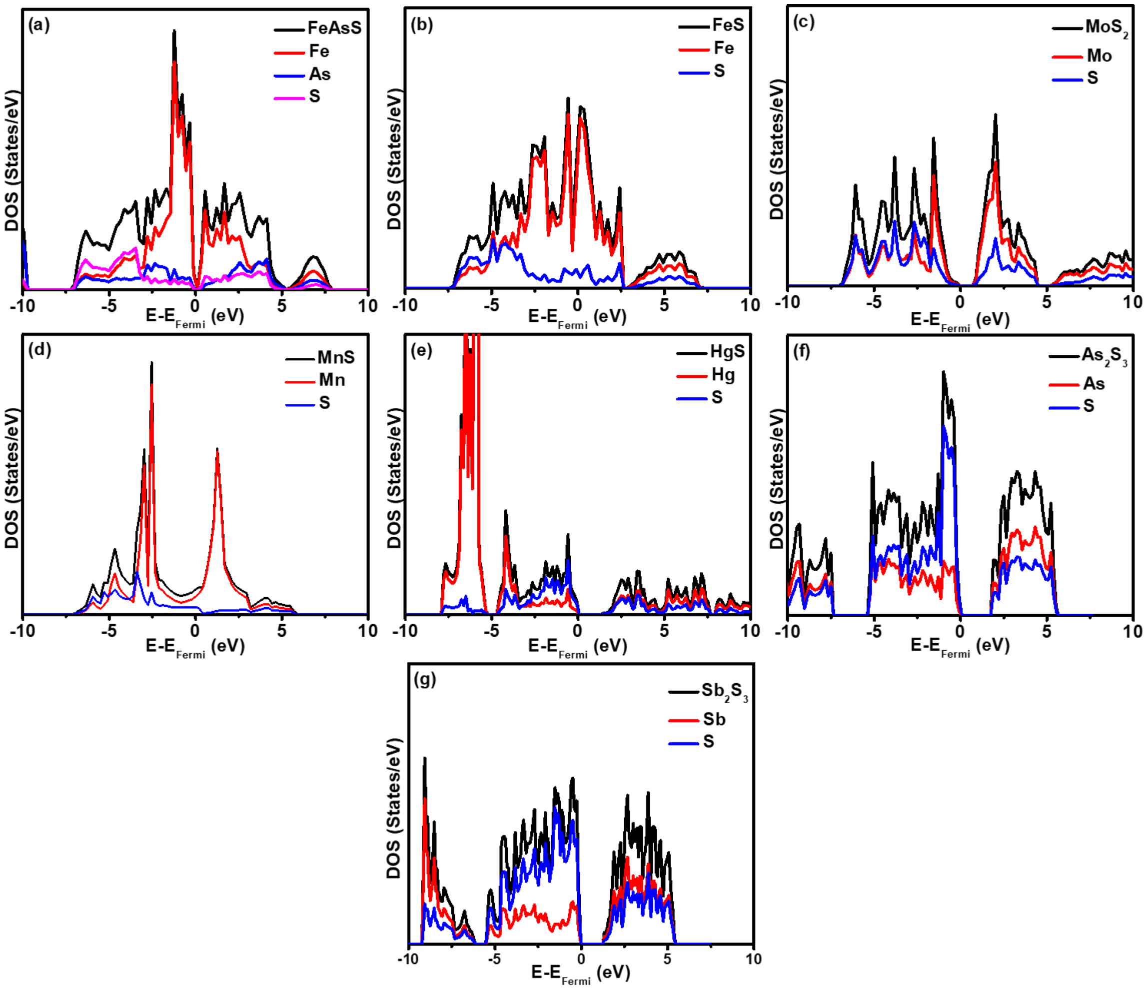

**Figure A.3** DFT calculated PDOS for bulk crystals: (a) FeAsS, (b) FeS, (c) $MoS_2$, (d) MnS, (e) HgS, (f) $As_2S_3$ and (g) $Sb_2S_3$.

## A.4 References

(1) Kresse, G.; Hafner, J. Ab Initio Molecular Dynamics for Liquid Metals. *Phys. Rev. B* **1993**, *47* (1), 558–561.

(2) Kresse, G.; Hafner, J. Ab Initio Molecular-Dynamics Simulation of the Liquid-Metal-Amorphous-Semiconductor Transition in Germanium. *Phys. Rev. B* **1994**, *49* (20), 14251–14269.

(3) Kresse, G.; Furthmüller, J. Efficiency of Ab-Initio Total Energy Calculations for Metals and Semiconductors Using a Plane-Wave Basis Set. *Comput. Mater. Sci.* **1996**, *6* (1), 15–50.

(4) Kresse, G.; Furthmüller, J. Efficient Iterative Schemes for Ab Initio Total-Energy Calculations Using a Plane-Wave Basis Set. *Phys. Rev. B* **1996**, *54* (16), 11169–11186.

(5) Blöchl, P. E. Projector Augmented-Wave Method. *Phys. Rev. B* **1994**, *50* (24), 17953–17979.

(6) Kresse, G. From Ultrasoft Pseudopotentials to the Projector Augmented-Wave Method. *Phys. Rev. B* **1999**, *59* (3), 1758–1775.

(7) Hammer, B.; Hansen, L. B.; Nørskov, J. K. Improved Adsorption Energetics within Density-Functional Theory Using Revised Perdew-Burke-Ernzerhof Functionals. *Phys. Rev. B* **1999**, *59* (11), 7413–7421.

(8) McCrum, I. T.; Hickner, M. A.; Janik, M. J. First-Principles Calculation of Pt Surface Energies in an Electrochemical Environment: Thermodynamic Driving Forces for Surface Faceting and Nanoparticle Reconstruction. *Langmuir* **2017**, *33* (28), 7043–7052.

(9) Nørskov, J. K.; Rossmeisl, J.; Logadottir, A.; Lindqvist, L.; Kitchin, J. R.; Bligaard, T.; Jónsson, H. Origin of the Overpotential for Oxygen Reduction at a Fuel-Cell Cathode. *J. Phys. Chem. B* **2004**, *108* (46), 17886–17892.

(10) Andersson, K. J.; Ogasawara, H.; Nordlund, D.; Brown, G. E.; Nilsson, A. Preparation, Structure, and Orientation of Pyrite $FeS_2$\{100\} Surfaces: Anisotropy, Sulfur Monomers, Dimer Vacancies, and a Possible Fes Surface Phase. *J. Phys. Chem. C* **2014**, *118* (38), 21896–21903.

(11) Chen, V. H. Y.; Mallia, G.; Martínez-Casado, R.; Harrison, N. M. Surface Morphology of $CuFeS_2$: The Stability of the Polar (112)/(112¯) Surface Pair. *Phys. Rev. B* **2015**, *92* (15), 1–9.

(12) Zherebetskyy, D.; Scheele, M.; Zhang, Y.; Bronstein, N.; Thompson, C.; Britt, D.; Salmeron, M.; Alivisatos, P.; Wang, L.-W. Hydroxylation of the Surface of PbS Nanocrystals Passivated with Oleic Acid. *Science* **2014**, *344* (6190), 1380–1384.

(13) Hamad, S.; Cristol, S.; Catlow, C. R. A. Surface Structures and Crystal Morphology of ZnS: Computational Study. *J. Phys. Chem. B* **2002**, *106* (42), 11002–11008.

(14) Monkhorst, H. J.; Pack, J. D. Special Points for Brillouin-Zone Integrations. *Phys. Rev. B* **1976**, *13* (12), 5188–5192.

(15) Lee, Y.-L.; Kleis, J.; Rossmeisl, J.; Shao-Horn, Y.; Morgan, D. Prediction of Solid Oxide Fuel Cell Cathode Activity with First-Principles Descriptors. *Energy Environ. Sci.* **2011**, *4* (10), 3966–3970.

(16) Grimaud, A.; May, K. J.; Carlton, C. E.; Lee, Y.-L.; Risch, M.; Hong, W. T.; Zhou, J.;

Shao-Horn, Y. Double Perovskites as a Family of Highly Active Catalysts for Oxygen Evolution in Alkaline Solution. *Nat. Commun.* **2013**, *4*, 1–7.

(17) Hong, W.; Stoerzinger, K. A.; Lee, Y.-L.; Giordano, L.; Grimaud, A. J. L.; Johnson, A. M.; Hwang, J.; Crumlin, E.; Yang, W.; Shao-Horn, Y. Charge-Transfer-Energy-Dependent Oxygen Evolution Reaction Mechanisms for Perovskite Oxides. *Energy Environ. Sci.* **2017**, *10*, 2190–2200.

(18) Zhao, B.; Zhang, L.; Zhen, D.; Yoo, S.; Ding, Y.; Chen, D.; Chen, Y.; Zhang, Q.; Doyle, B.; Xiong, X.; et al. A Tailored Double Perovskite Nanofiber Catalyst Enables Ultrafast Oxygen Evolution. *Nat. Commun.* **2017**, *8*, 1–9.

(19) Jacobs, R.; Booske, J.; Morgan, D. Understanding and Controlling the Work Function of Perovskite Oxides Using Density Functional Theory. *Adv. Funct. Mater.* **2016**, *26* (30), 5471–5482.

(20) Shao, M.; Chang, Q.; Dodelet, J.-P.; Chenitz, R. Recent Advances in Electrocatalysts for Oxygen Reduction Reaction. *Chem. Rev.* **2016**, *116* (6), 3594–3657.

(21) Chen, Z.; Higgins, D.; Yu, A.; Zhang, L.; Zhang, J. A Review on Non-Precious Metal Electrocatalysts for PEM Fuel Cells. *Energy Environ. Sci.* **2011**, *4* (9), 3167–3192.

(22) Malakhov, I. V; Nikitenko, S. G.; Savinova, E. R.; Kochubey, D. I.; Alonso-Vante, N. In Situ EXAFS Study To Probe Active Centers of Ru Chalcogenide Electrocatalysts During Oxygen Reduction Reaction. *J. Phys. Chem. B* **2002**, *106* (7), 1670–1676.

(23) Alonso-Vante, N.; Malakho, I. V; Nikitenko, S. G.; Sa, E. R. The Structure Analysis of the Active Centers of Ru-Containing Electrocatalysts for the Oxygen Reduction. An in

Situ EXAFS Study. *Electrochim. Acta* **2002**, *47* (22–23), 3807–3814.

(24) Lee, K.; Zhang, L.; Zhang, J. Ternary Non-Noble Metal Chalcogenide (W-Co-Se) as Electrocatalyst for Oxygen Reduction Reaction. *Electrochem. commun.* **2007**, *9* (7), 1704–1708.

(25) Tritsaris, G. A.; Nørskov, J. K.; Rossmeisl, J. Trends in Oxygen Reduction and Methanol Activation on Transition Metal Chalcogenides. *Electrochim. Acta* **2011**, *56* (27), 9783–9788.

(26) Suntivich, J.; Gasteiger, H. A.; Yabuuchi, N.; Nakanishi, H.; Goodenough, J. B.; Shao-Horn, Y. Design Principles for Oxygen-Reduction Activity on Perovskite Oxide Catalysts for Fuel Cells and Metal-Air Batteries. *Nat. Chem.* **2011**, *3* (7), 546–550.

(27) Asadi, M.; Kim, K.; Liu, C.; Addepalli, A. V.; Abbasi, P.; Yasaei, P.; Phillips, P.; Behranginia, A.; Cerrato, J. M.; Haasch, R.; et al. Nanostructured Transition Metal Dichalcogenide Electrocatalysts for $CO_2$ Reduction in Ionic Liquid. *Science* **2016**, *353* (6298), 467–470.

(28) Durand, W. J.; Peterson, A. A.; Studt, F.; Abild-Pedersen, F.; Nørskov, J. K. Structure Effects on the Energetics of the Electrochemical Reduction of $CO_2$ by Copper Surfaces. *Surf. Sci.* **2011**, *605* (15–16), 1354–1359.

(29) Liu, S.; White, M. G.; Liu, P. Mechanism of Oxygen Reduction Reaction on Pt(111) in Alkaline Solution : Importance of Chemisorbed Water on Surface. *J. Phys. Chem. C* **2016**, *120* (28), 15288–15298.

(30) Tritsaris, G. A. Trends in Low-Temperature Fuel Cell Catalysis: A Computational Study,

Technical University of Denmark (DTU), 2011.

(31) Ogasawara, H.; Brena, B.; Nordlund, D.; Nyberg, M.; Pelmenschikov, A.; Pettersson, L. G. M.; Nilsson, A. Structure and Bonding of Water on Pt(111). *Phys. Rev. Lett.* **2002**, *89* (111), 2761021–2761024.

(32) Maier, S.; Lechner, B. A. J.; Somorjai, G. A.; Salmeron, M. Growth and Structure of the First Layers of Ice on Ru(0001) and Pt(111). *J. Am. Chem. Soc.* **2016**, *138* (9), 3145–3151.

(33) Cramer, C. J. *Essentials of Computational Chemistry Theories and Models*, Second Edi.; John Willey & Sons Ltd: Chichester, 2004.

(34) Rosen, J.; Hutchings, G. S.; Lu, Q.; Rivera, S.; Zhou, Y.; Vlachos, D. G.; Jiao, F. Mechanistic Insights into the Electrochemical Reduction of $CO_2$ to CO on Nanostructured Ag Surfaces. *ACS Catal.* **2015**, *5* (7), 4293–4299.

(35) Rand, D. A. J. Oxygen Reduction on Sulphide Minerals: Part III. Comparison of Activities of Various Copper, Iron, Lead and Nickel Mineral Electrodes. *J. Electroanal. Chem. Interfacial Electrochem.* **1977**, *83* (1), 19–32.

(36) Downs, R. T.; Hall-Wallace, M. The American Mineralogist Crystal Structure Database. *Am. Mineral.* **2003**, *88* (1), 247–250.

# Appendix B Supporting Information for Chapter 5

## B.1 The relationship between the hydrophobicity and bond ionicity in the context of minerals flotation

It is well known that hydrophobic functionalization of metal sulfides plays a critical role in the realization of efficient mineral separation using the froth flotation technology.[1] The high-performance mineral flotation requires the addition of surfactant molecule (collector), normally composed of a chemically reactive head group and a hydrophobic tail. The collector adsorbs on the mineral surface through the head group, while the tail exposes toward the surrounding aqueous flotation pulp. The induced or enhanced surface hydrophobicity facilitates the attachment of mineral particles to air bubbles and consequently, leads to the separation from hydrophilic minerals.[2–4] As such, various theories have been proposed to consummate the design and screening of more effective collectors for higher flotation performance.

The pioneering Taggart's solubility product theory asserts that the collecting ability of a surfactant is mainly determined by the solubility product of the corresponding metal−ligand compound in solution from the sense of chemical reaction.[5] The basic idea is analogous to the implicit theory of like dissolves like. This theory has been verified to be capable of rationalizing many well-known experimental phenomena in mineral flotation. Despite the widespread acceptance of the solubility product ($pK_{sp}$) in assessing the collecting capacity, its poor predictive power makes it unsuitable to guide the design of new collectors.

In response, a more advanced model on the basis of the electronegativity theory was advocated by D.Z. Wang et al.[6] They linked the collecting ability of the ligand toward minerals with the relative electronegativity difference $[(\Delta\lambda)^2]$ between the ligand head group (e.g., $-OCS_2$, $-NCS_2$

or $-O_2PS_2$) and the active metal atom on mineral surface (e.g., Cu, Pb or Fe). Specifically, a smaller value of $(\Delta\lambda)^2$ indicates a stronger covalent bonding interaction which contributes to a more hydrophobic surface. Conversely, a larger value of $(\Delta\lambda)^2$ represents a weaker covalent bond and a less hydrophobic surface. The relative values of $(\Delta\lambda)^2$ were found to correlate well with the corresponding solubility products. Therefore, the bond ionicity can be taken as a guidance for minerals flotation.

## B.2 Calculation of the ligand electronegativity

In this study, it was found that the ligand–ZnS(110) bond is highly ionic, and the relative ionicities correlate well with the corresponding experimental solubility product constant of the compounds. This naturally motivates us to use a parameter that can reflect the electronegativity of the ligands to serve as the computational descriptor.

We calculated the electronegativity ($\chi 1$) of the ligands using Gaussian [ub3lyp/6-311++g(3df,3pd)].[7–9] The structures of the ligands optimized in VASP[10–13] were used without further optimizations for the corresponding anion and cation states. The electronegativity was calculated as,[14,15]

$$\chi = \frac{(IE+EA)}{2} \qquad \text{B-1}$$

$$IE = IE_v = E_{tot}(X^+) - E_{tot}(X) \qquad \text{B-2}$$

$$EA = EA_v = E_{tot}(X) - E_{tot}(X^-) \qquad \text{B-3}$$

where $\chi$ is the electronegativity, IE is the vertical ionization energy and EA is the vertical electron affinity. For comparison, we also calculated the electronegativity ($\chi 2$) of the ligands which were further optimized in VASP in 30 × 30 × 30 cell and with more strict convergence conditions (EDIFF = 1e−6 and EDIFFG = −0.01). Alternatively, we calculated a parameter in VASP and assumed it as SOMO (i.e., singly occupied molecular orbital). Since for radical with an odd number of electrons, the spin orbitals are separated with different energy levels and each of the occupied ones can only contain one electron. Besides, the orbital energies obtained in VASP cannot be directly used, since the vacuum energy level is not zero due to the periodic boundary conditions. As such, the SOMO defined above was calculated by subtracting the vacuum energy level from the Fermi level of the radical system in a way similar to that of work function. All these results were compared with the electronegativity values calculated by D. Z. Wang et al. using empirical parameters which is denoted as the empirical electronegativity (λ) here, as shown in Figure B.1 below.[6]

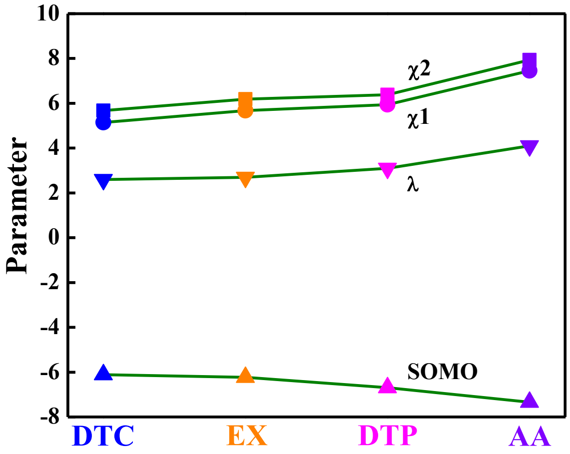

**Figure B.1** Computational parameters (χ1, χ2 and SOMO) and empirical electronegativity (λ) of the ligands.

Although the different data sources correlate well, we eventually decide to use the electronegativity (χ2) calculated in Gaussian to better reflect the intrinsic attribute of free ligands and to avoid confusions. More suitable parameters may be selected based on specific system and database size.

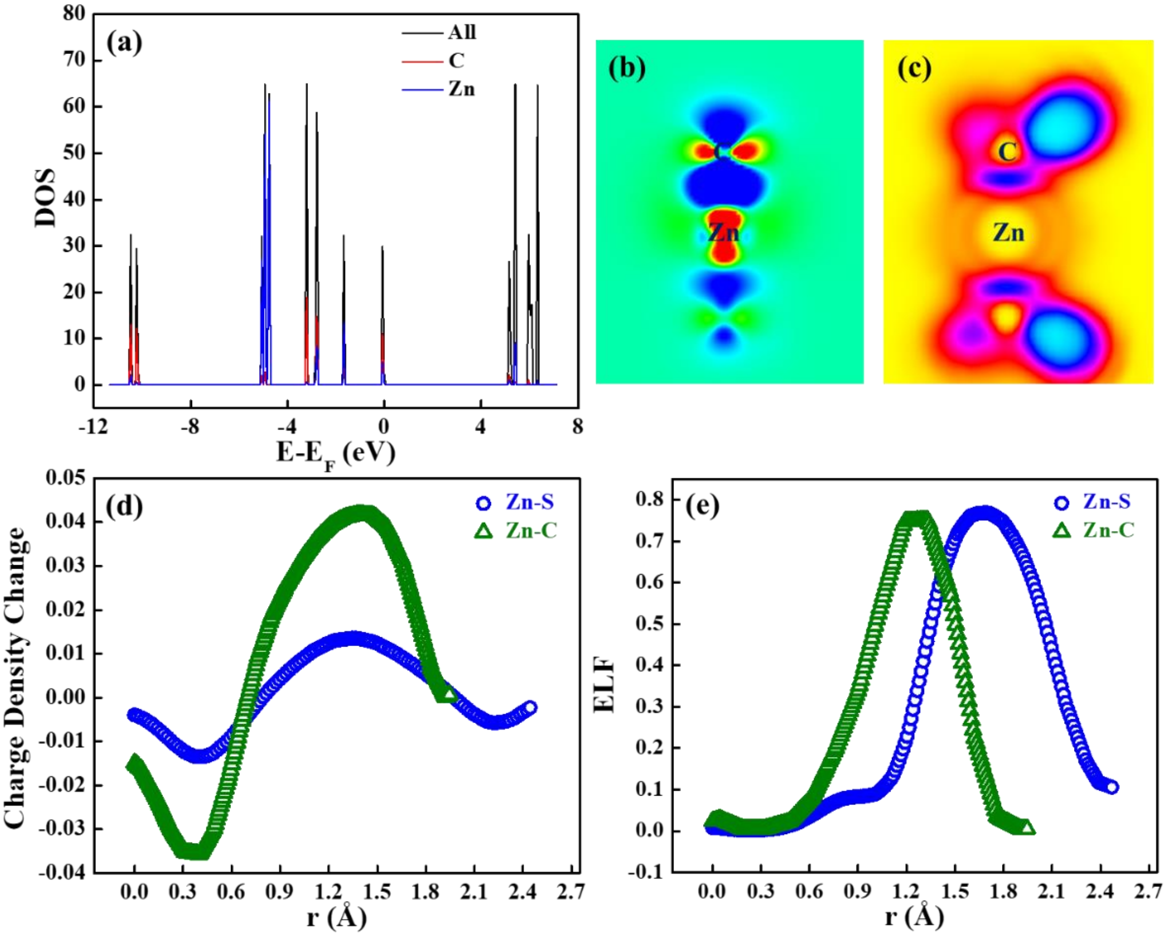

**Figure B.2** (a) PDOS, (b) charge density difference map (CDDM), (c) electron location function (ELF) of dimethylzinc; (d) the line profiles of CDDM along Zn−C for dimethylzinc (green) and Zn−S for DTC−ZnS(110) (blue), (e) the line profiles of ELF along Zn−C for dimethylzinc (green) and Zn−S for DTC−ZnS(110) (blue).

### B.3 DFT Calculations for dimethylzinc

Since the Zn−C bond has a significant amount of covalence, we constructed the dimethylzinc model and applied the same analytical techniques to verify our conclusions. DFT calculations were conducted with the dimethylzinc $[Zn(CH_3)_2]$ in a 30 × 30 × 30 cell using the same methods. The results are presented in Figure B.2 (a)-(f) below. The line profiles along Zn−C bond for the charge density difference map (CDDM) and the electron localization function (ELF) are compared with those of the DTC−ZnS(110) system in Figure B2(c) and (d), respectively, since DTC forms the strongest covalent bond among the four ligands studied. The color scales for CDDM and ELF are identical as those in the manuscript.

PDOS in Figure B.2(a) shows that the valence electrons of the connected Zn and C are strongly correlated. Moreover, upon binding of the $CH_3$ radical to $CH_3Zn$, substantial electron accumulations can be observed in the Zn−C bonding region in Figure B.2(b), and the contour indicates slight polarization toward C. In terms of the ELF in Figure B.2(c), there is clear localization domain along the Zn−C bond and locates closely to the bond center. Overall, these results suggest that the Zn−C bond in dimethylzinc is strongly covalent with slight polarization.

Apparently, the results for dimethylzinc are very different from the ligand−ZnS(110) systems. By examining Figure B.2(d), we can see that the electron accumulation within the bonding area is much stronger than that of the DTC−ZnS(110). Moreover, for the ELF in Figure B.2(e), the localization domain locates more closely to the Zn in dimethylzinc along the bond, while this domain is much more stretched toward S in DTC−ZnS(110). Therefore, the Zn−C bond possess considerably larger fractions of covalency than Zn−S in the ligand−ZnS(110) systems which further verified our analytical techniques and confirmed the applicability of our methodology.

## B.4 References

(1) Rosso, K. M. Reactivity of Sulfide Mineral Surfaces. *Rev. Mineral. Geochemistry* **2006**, *61* (1), 557–607.

(2) Ma, X.; Xia, L.; Wang, S.; Zhong, H.; Jia, H. Structural Modification of Xanthate Collectors to Enhance the Flotation Selectivity of Chalcopyrite. *Ind. Eng. Chem. Res.* **2017**, *56* (21), 6307–6316.

(3) Moreels, I.; Fritzinger, B.; Martins, J. C.; Hens, Z. Surface Chemistry of Colloidal PbSe Nanocrystals. *J. Am. Chem. Soc.* **2008**, *130* (45), 15081–15086.

(4) Woods, R. Oxidation of Ethyl Xanthate on Platinum, Gold, Copper, and Galena Electrodes. Relation to the Mechanism of Mineral Flotation. *J. Phys. Chem.* **1971**, *75* (3), 354–362.

(5) Taggart, A. F. *Handbook of Mineral Dressing, Ores and Industrial Minerals*; Taggart, A. F., Ed.; J. Wiley & sons, Incorporated: New York, 1945.

(6) Wang, D. *Flotation Reagents: Applied Surface Chemistry on Minerals Flotation and Energy Resources Beneficiation*; Springer Singapore, 2016.

(7) Gaussian 16, Revision B.01, Frisch, M. J.; Trucks, G. W.; Schlegel, H. B.; Scuseria, G. E.; Robb, M. A.; Cheeseman, J. R.; Scalmani, G.; Barone, V.; Petersson, G. A.; Nakatsuji, H.; Li, X.; Caricato, M.; Marenich, A. V.; Bloino, J.; Janesko, B. G.; Gomperts, R.; Mennucci, B.; Hratchian, H. P.; Ortiz, J. V.; Izmaylov, A. F.; Sonnenberg, J. L.; Williams-Young, D.; Ding, F.; Lipparini, F.; Egidi, F.; Goings, J.; Peng, B.; Petrone, A.; Henderson, T.; Ranasinghe, D.; Zakrzewski, V. G.; Gao, J.; Rega, N.; Zheng, G.; Liang, W.; Hada,

M.; Ehara, M.; Toyota, K.; Fukuda, R.; Hasegawa, J.; Ishida, M.; Nakajima, T.; Honda, Y.; Kitao, O.; Nakai, H.; Vreven, T.; Throssell, K.; Montgomery, J. A., Jr.; Peralta, J. E.; Ogliaro, F.; Bearpark, M. J.; Heyd, J. J.; Brothers, E. N.; Kudin, K. N.; Staroverov, V. N.; Keith, T. A.; Kobayashi, R.; Normand, J.; Raghavachari, K.; Rendell, A. P.; Burant, J. C.; Iyengar, S. S.; Tomasi, J.; Cossi, M.; Millam, J. M.; Klene, M.; Adamo, C.; Cammi, R.; Ochterski, J. W.; Martin, R. L.; Morokuma, K.; Farkas, O.; Foresman, J. B.; Fox, D. J. Gaussian, Inc., Wallingford CT, 2016.

(8) Chowdhry, M. Theoretical Study on Reactivity of Different Sulfide Collectors and Their Binding Affinity toward Cu(II), Zn(II) and Pb(II) Ions. Ph.D Dissertation, University of Alberta, Edmonton, AB, 2015.

(9) Lee, Chengteh, Weitao Yang, and R. G. P. Development of the Colle-Salvetti Correlation-Energy Formula into a Functional of the Electron Density. *Phys. Rev. B* **1988**, *37* (2), 785–789.

(10) Kresse, G.; Hafner, J. Ab Initio Molecular Dynamics for Liquid Metals. *Phys. Rev. B* **1993**, *47* (1), 558–561.

(11) Kresse, G.; Hafner, J. Ab Initio Molecular-Dynamics Simulation of the Liquid-Metal–amorphous-Semiconductor Transition in Germanium. *Phys. Rev. B* **1994**, *49* (20), 14251–14269.

(12) Kresse, G.; Furthmüller, J. Efficiency of Ab-Initio Total Energy Calculations for Metals and Semiconductors Using a Plane-Wave Basis Set. *Comput. Mater. Sci.* **1996**, *6* (1), 15–50.

(13) Kresse, G.; Furthmüller, J. Efficient Iterative Schemes for Ab Initio Total-Energy Calculations Using a Plane-Wave Basis Set. *Phys. Rev. B* **1996**, *54* (16), 11169–11186.

(14) Rienstra-Kiracofe, J. C.; Tschumper, G. S.; Schaefer, H. F.; Nandi, S.; Ellison, G. B. Atomic and Molecular Electron Affinities: Photoelectron Experiments and Theoretical Computations. *Chem. Rev.* **2002**, *102* (1), 231–282.

(15) Thomas Heine, Jan-Ole Joswig, A. G. Computational Chemistry Workbook. *ChemPhysChem* **2011**, *12* (11), 2184.

# Appendix C Implicit solvation model VASP$_{sol}$

The implicit solvation calculations are computationally much cheaper than the explicit solvation model.[1] The basic idea of implicit solvation model is to put the solute in a cavity which is surrounded by a continuum dielectric description of the solvent. The solute is treated quantum-mechanically, and the response of solvent to the solute charge density is described by the local relative permittivity of the solvent. Normally, for polar or ionic solute system in contact with polar fluids, the most significant solvation effects arise from the electrostatic interaction between the solute and the solvent; for nonpolar solutes and solvents, the van der Waals interaction may dominate over electrostatics; for large molecules, the energy required to form a cavity in the solvent, i.e., the cavitation energy, accounts primarily for the solvation energy. Thus, the solvation theories which can be generally applicable to nanoparticles, molecules, and surfaces must consider all these effects.[2] Besides, the cavitation and repulsion energies are positive, while the dispersion contribution is always negative. Overall, these terms tend to cancel each other and their effect on molecular properties and chemical reactions has been generally regarded as less important than the electrostatic term.[3] Within the scheme of VASP$_{sol}$, the solute system is surrounded by a dielectric medium which is quantified by the relative permittivity of the solvent system, $\epsilon(\vec{r})$.[2] The electrostatic term is calculated as,

$$E_{el} = -\int d^3r\epsilon(\vec{r})\frac{|\nabla\phi|^2}{8\pi} \qquad \text{C-1}$$

where $\phi(r)$ is the combined electrostatic potential due to the electronic and nuclear charges of the solute system in a polarizable medium. Since the non-electrostatic effects are mainly concentrated in the first solvation shell, these corrections are described as an interface term that is proportional to the solvation-accessible area,

$$E_{non-el} = \tau \int d^3 r \nabla S \tag{C-2}$$

where $\tau$ is the effective surface tension parameter which describes the cavitation, dispersion and the repulsion interaction between the solute and the solvent that are not captured by the electrostatic terms alone, and $S(\text{r})$ is the cavity shape function.

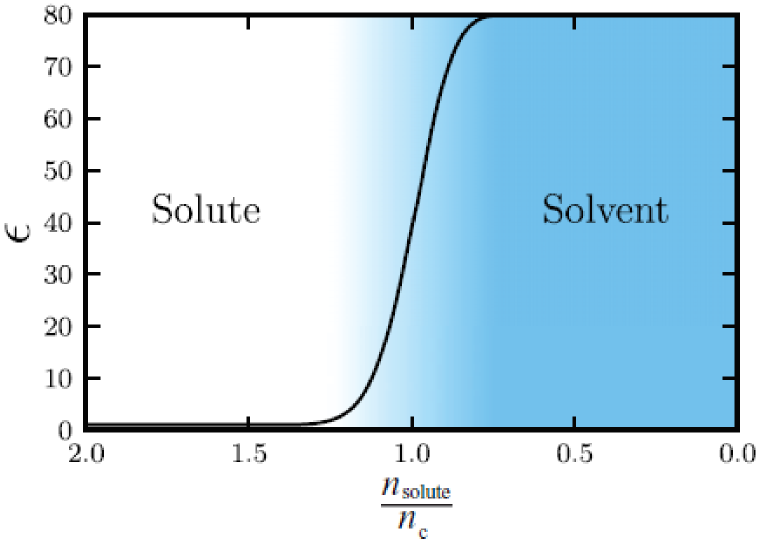

**Figure C.1** Smooth variation the relative permittivity, $\epsilon$, from the vacuum value of 1 to the value of the solvent, e.g., 80 for water.[2]

The existing implicit solvation models often differ in their approximations for the form of the dielectric cavity formed in the solvent by the solute. A common way to construct the cavity is to place spheres around the solute atoms and then take the union of these overlapping spheres.[3,4] This choice allows to have a regular discretization of the cavity surface that benefits the numerical convergence. Inside the cavity, the relative permittivity is assumed to be that of vacuum, outside it takes the value of the solvent, the induced charges are placed on the surface of this cavity. However, the numerical discretization of the cavity surface also leads to atomic forces that are not continuous with respect to atomic positions and suffers from numerical singularities. For this reason, in VASPsol, a diffuse dielectric cavity which is a local functional of the electronic charge density of the solute is assumed,

$$S\big(n_{solute}(\vec{r})\big) = \frac{1}{2} erfc\left[\frac{\log(n_{solute}/n_c)}{\sigma\sqrt{2}}\right] \quad \text{C-3}$$

$$\epsilon\big(n_{solute}(\vec{r})\big) = 1 + (\epsilon_b - 1)S(n_{solute}(\vec{r})) \quad \text{C-4}$$

where $S\big(n_{solute}(\vec{r})\big)$ is the cavity shape function, $n_c$ determines the critical value of the electron density of the dielectric where the cavity forms, and $\sigma$ is the parameter that determines the width of the diffuse cavity, $\epsilon\big(n_{solute}(\vec{r})\big)$ is the relative permittivity of the solvent and $\epsilon_b$ is the relative permittivity of the bulk solvent. This generates a diffuse cavity, as implicitly determined by the electronic structure of the solute, and ensures that the value of the relative permittivity varies smoothly from 1 in the bulk of the solute to $\epsilon_b$ in the bulk of the solvent which closely emulates the first solvation shell effects. Also, the smoothly changed relative permittivity ensures that the derivatives of the energy functional are continuous and thereby simplifying the subsequent implementation of the geometric optimization of the solute system. The values of the parameters are given as $n_c = 0.0025\,\text{Å}^{-3}$ , $\sigma = 0.6$ and $\tau = 0.525\, meV/\text{Å}^2$ by fitting the model to experimental solvation energies for a series of molecules in water.[5] VASPsol is further validated by comparing the solvation energies of several molecules with both the values obtained for the same solvation model from the JDFTx code and the relevant experimental values.

## C1. References

(1) Gauthier, J. A.; Dickens, C. F.; Chen, L. D.; Doyle, A. D.; Nørskov, J. K. Solvation Effects for Oxygen Evolution Reaction Catalysis on $IrO_2$(110). *J. Phys. Chem. C* **2017**, *121* (21), 11455–11463.

(2) Mathew, K.; Sundararaman, R.; Letchworth-Weaver, K.; Arias, T. A.; Hennig, R. G. Implicit Solvation Model for Density-Functional Study of Nanocrystal Surfaces and Reaction Pathways. *J. Chem. Phys.* **2014**, *140* (8), 084106.

(3) Andreussi, O.; Dabo, I.; Marzari, N. Revised Self-Consistent Continuum Solvation in Electronic-Structure Calculations. *J. Chem. Phys.* **2012**, *136* (6), 064102.

(4) Tomasi, J., Mennucci, B. and Cammi, R. Quantum Mechanical Continuum Solvation Models. *Chem. Rev.* **2005**, *105* (8), 2999–3093.

(5) Gunceler, D.; Letchworth-Weaver, K.; Sundararaman, R.; Schwarz, K. A.; Arias, T. A. The Importance of Nonlinear Fluid Response in Joint Density-Functional Theory Studies of Battery Systems. *Model. Simul. Mater. Sci. Eng.* **2013**, *21* (7), 074005.